THE UNIVERSITY OF CHICAGO

ALLOYED III-V NANOCRYSTALS AS VIABLE EMITTERS FOR DISPLAY APPLICATIONS

A DISSERTATION SUBMITTED TO

THE FACULTY OF THE DIVISION OF THE PHYSICAL SCIENCES

IN CANDIDACY FOR THE DEGREE OF

DOCTOR OF PHILOSOPHY

DEPARTMENT OF CHEMISTRY

BY

ARITRAJIT GUPTA

CHICAGO, ILLINOIS

DECEMBER 2023

Table of Contents

List of Figures

List of Tables

Acknowledgments

Information inundates us daily. Under the able guidance of my dissertation advisor, Prof. Dmitri Talapin, I learned how to process it to extract cumulative knowledge systematically. I am grateful for his unwavering support and guidance throughout my academic and personal journey, particularly during the uncertainties posed by a global pandemic. His mentorship and expertise have been instrumental in shaping the trajectory of my doctorate research. I also want to acknowledge the contributions of my dissertation committee members, Prof. Philippe Guyot-Sionnest and Prof. John Anderson, whose valuable feedback and dedication to academic excellence have improved the quality of this work. During my tenure, I had the privilege of collaborating with several esteemed research groups, including those led by Prof. Richard Schaller at Argonne National Laboratory and Northwestern University, Prof. Aaron Rossini at Ames National Laboratory and Iowa State University, Prof. Eran Rabani at the University of California, Berkeley, Prof. Allison Squires, and Prof. Greg Engel at the University of Chicago. Their insights and contributions exemplify the power of collaboration in today's scientific landscape.

As Dmitri would point out, the teachers we learn the most from are often our peers. I am fortunate to have had Dr. Margaret Hudson as an exceptional mentor during the formative stages of my academic journey. I must also thank all the current and former members of the Talapin group I overlapped with, Dr. Justin Ondry, Dr. Jun-Hyuk Chang, Dr. James Cassidy, Haoqi Wu, Di Wang, Zirui Zhou, Ahhyun Jeong, Ruiming Lin, Zehan Mi, Young-Hwan Kim, Youssef Tazoui, Luca Giordano, Prof. Chenkun Zhou, Dr. Wooje Cho, Dr. Josh Portner, Jingxing Geng, Dr. Iryna Golovina, Alex Hinkle, Dr. Jia-Ahn Pan, Dr. Igor Coropceanu, Prof. Himchan Cho, Dr. Min Chen, Dr. Huicheng Hu, Dr. Vlad Kamysbayev, Nivedina Sarma, Thomas Habte, Prof. Yuanyuan Wang,

Ayat Tasanov, Eleanor Dunietz, Dr. Eric Janke and Dr. Xinzheng Lan for their camaraderie and support. I am grateful to have found amazing colleagues as well as lifelong friends among you.

Every graduate school journey encounters its share of treacherous stretches, and within UChicago Chemistry, Dr. Vera Dragisich and Melinda Moore have been one of the few constant pillars of support. I must thank Dr. Meishan Zhao and the amazing undergraduate students in my discussion section for making my Teaching Assistantship a seamless and truly rewarding experience. This work made use of the shared resources at the University of Chicago Materials Research Science and Engineering Center, Advanced Electron Microscopy, and X-ray Research facilities on various occasions. I extend my heartfelt appreciation to the dedicated facility directors, Dr. Alex Filatov, Dr. Justin Jureller, Dr. Qiti Guo, and Yimei Chen. Their expertise and commitment to providing access to essential research tools have significantly contributed to the success of my work. Our group administrators, Dr. Andrew Nelson and Tanya Shpigel have played a vital role in supporting the daily operations of our research group. I'm grateful for their efforts in perusing and editing various scientific communications I have been involved in. I am thankful for the financial support provided by the Samsung Advanced Institute of Technology and the National Science Foundation. A special note of gratitude goes to Nanosys, Inc. (Milpitas, CA) for contributing samples to this study.

My parents, Dr. Ashis Gupta and Mala Mazumdar have been my constant source of motivation and encouragement, and I am thankful for their sacrifices throughout my academic pursuits. Their support has granted me the privilege of shielding myself from the external world's demands as I pursued my graduate studies, a gift I have come to value more as I grow older.

As international students moving abroad, we must establish new social circles and support systems. In Chicago, my friends have provided a sense of belonging akin to the familial bonds I

cherished back home. Exploring the picturesque UChicago campus with Mykyta, Abhirup, Kavya, Geoffrey, and Joseph during the frequent coffee breaks has become an integral part of my daily routine. I have fond memories of the numerous meals I have shared with friends such as Sneha, Mandira, Titli, Ram, Ananth, Kwanghoon, Poojya, Kruthika, Gregory, Alexandra, and Melissa. My long-time college friends, Punarbasu, Ameya, Shayani, Prathitha, Souvik, Angana, Subhendu, and Aravind, have been a constant source of companionship during my time in the States. I look forward to our continued success and growth in our professional journeys.

I would like to express my heartfelt gratitude to the many mentors, friends, and family whose unwavering support and encouragement have played a pivotal role in the completion of this doctoral dissertation. Thank you, from the bottom of my heart.

Preface

"By the means of Telescopes, there is nothing so far distant but may be represented to our view; and by the help of Microscopes, there is nothing so small, as to escape our inquiry; hence there is a new visible World discovered to the understanding. By this means the Heavens are open'd, and a vast number of new Stars, and new Motions, and new Productions appear in them, to which all the ancient Astronomers were utterly Strangers. By this the Earth it self, which lyes so neer us, under our feet, shews quite a new thing to us, and in every little particle of its matter; we now behold almost as great a variety of Creatures, as we were able before to reckon up in the whole Universe it self." - *Micrographia* (excerpt), Robert Hooke, January 1665

On a day of profound significance to mankind, Robert Hooke turned his array of magnifying lenses to a section of cork, and the microscopic world laid its secrets bare to an inquisitive human eye. Enamored with the allure of what the naked eye cannot visualize, scientists have developed more and more powerful microscopes over the course of the next few centuries. Our understanding of the physical world advanced by strides with the advent of quantum mechanics, and we were finally able to supplement the newly developed theories with observations of quantum mechanical phenomena on the nanometer scale. At present, numerous technological breakthroughs and innovative fabrication techniques allow us to engineer material structures with unparalleled precision, and we are now able to perform keen observations and rationalize physical phenomena transpiring in the atomistic dimensions. These developments on various fronts, coupled with the imperative to execute large-scale logical operations at an unprecedented pace, ushered us into the era of semiconductors. To this day, we continue to add to the complexity of semiconductor devices, seeking greater efficiency and longevity in our pursuit of technological excellence.

Abstract

III-V colloidal nanocrystals, such as InP, have emerged as a viable alternative to their heavily optimized II-VI counterparts, owing to their lower toxicity and enhanced structural stability. However, the III-V bonds are predominantly covalent, making it difficult to achieve microscopic reversibility for defect-free crystal growth, except at elevated temperatures inaccessible to traditional organic solvents. Additionally, the confinement sizing curve dictates that blue emission would only be achievable from minuscule InP nanocrystals that are inherently unstable. We address these challenges by introducing molten halide salts as reaction media for performing In-to-Ga cation exchange to synthesize alloyed $In_{1-x}Ga_xP$ nanocrystals with a bandgap greater than their InP counterparts. Subsequent sections in this dissertation present a comprehensive study of emissive $In_{1-x}Ga_xP$ nanocrystals, including the kinetic factors governing In-to-Ga cation exchange, variations in excitonic oscillator strength in relation to gallium composition, and synthetic strategies to achieve stable blue emission.

In Chapter 2, we estimate the kinetic factors that govern isovalent In-to-Ga cation exchange in InP nanocrystals. The gallium halide molten salt reaction medium causes surface recrystallization of spherical InP nanocrystals to yield tetrahedral $In_{1-x}Ga_xP$ nanocrystals during high-temperature annealing. We estimate the activation energy of Ga exchange in nanocrystalline InP at ~0.9 eV, considerably lower than the activation energy measured for self-diffusion in the corresponding bulk systems. It has long been debated if crystal momentum **k** is a useful quantum number to describe band structure in quantum-confined nanocrystalline systems, which blur the distinction between direct and indirect gap semiconductors. Bulk crystals of $In_{1-x}Ga_xP$ constitute a prototypical platform for analyzing band structure in ternary III-V alloys of direct- and relatively narrow-gap InP with indirect- and relatively wide-gap GaP. The direct-to-indirect band gap

transition in nanocrystalline $In_{1-x}Ga_xP$ is investigated in Chapter 3 by producing an optimized synthetic protocol for In-to-Ga cation exchange in inorganic molten salts, and subsequently growing ZnS shells on $In_{1-x}Ga_xP$ to form bright core-shell $In_{1-x}Ga_xP$/ZnS QDs. Time-resolved PL studies indicate that the oscillator strength of excitonic transitions decreases with gallium incorporation, represented by a monotonic increase in radiative decay lifetime. The direct-to-indirect gap transition occurs with roughly the same composition dependence as in bulk $In_{1-x}Ga_xP$, demonstrated by the loss of an excitonic bleach feature in transient absorption.

Therefore, we must strike a balance between the nanocrystal size and gallium composition to achieve blue emission from alloyed $In_{1-x}Ga_xP$ nanocrystals while preserving the oscillator strength of direct-like interband transitions. In Chapter 4 we outline a protocol to prepare $In_{1-x}Ga_xP$ quantum dots by performing In-to-Ga cation exchange on small InP nanocrystals to achieve one of the first instances of bright and color pure blue emission from III-V nanocrystals. Compared to InP, $In_{1-x}Ga_xP$ has a better lattice constant match with ZnS, allowing us to overgrow a relatively thick ZnS shell. We demonstrate that the resulting commensurability of the core and shell leads to increased thermal stability of their PLQY. Our co-optimization of size and composition in the $In_{1-x}Ga_xP$ system establishes cation exchange in molten salts as a viable route to high-quality, nontoxic III-V QD emitters for display applications.

1. Introduction

1.1. Quantum-confined semiconductor nanocrystals.

Inorganic semiconductors are ubiquitously employed as the active material in modern-day electronic devices. They offer unparalleled optoelectronic performance, including superior carrier mobilities, efficient photoluminescence, and remarkable thermal stability. However, the growth of inorganic semiconductors as defect-free single crystals is performed at high temperatures while tailored structures often require high-vacuum processes, examples being molecular beam epitaxy (MBE) and chemical vapor deposition (CVD). Their fabrication through cost-effective means remains a formidable challenge, hence it becomes imperative to introduce more economical alternatives to conventional technologies reliant on single crystals. Solution-based techniques such as spin coating, dip coating, spray coating, doctor blading, or inkjet printing significantly reduce production costs for electronic and optoelectronic devices.[1-2] In this regard, semiconductor nanocrystals emerge as viable candidates for solution-processed optoelectronic devices, forming thermodynamically stable colloidal solutions that are easily processable. They are typically synthesized from reactive precursors under carefully tuned reaction conditions, allowing for controlled nucleation and growth of the crystalline domains. The long-chain coordinating surfactants usually present during the reaction play an essential role in determining the morphology and size distribution of these crystallites while also imparting colloidal stability in nonpolar solvents via steric repulsion. As a representative schematic, Figure 1.1 shows a calculated atomic structure of a 5 nm diameter lead sulfide (PbS) nanocrystal with its metal-rich facets passivated with oleic acid and hydroxyl ligands.[3]

The optoelectronic properties of semiconductor nanocrystals are easily tunable, making them versatile materials for applications ranging from advanced solar cells to efficient LEDs. As

the nanocrystal's dimensions become smaller than its Bohr exciton radius, band-like energy levels undergo discretization. In the strong quantum confinement regime, energies of the discrete electron

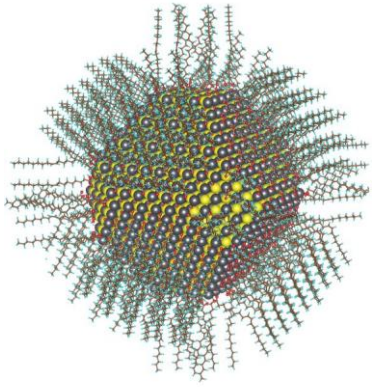

Figure 1.1. Calculated atomic structure of a Lead Sulfide (PbS) nanocrystal with ligands. Representative schematic showing a calculated atomic structure of a 5 nm diameter lead sulfide (PbS) nanocrystal with oleic acid and hydroxyl ligands coordinating to its metal-rich facets. Reproduced with permission from Zherebetskyy, D. *et al. Science* **2014,** *344* (6190), 1380-1384.[3] Copyright 2014, American Association for the Advancement of Science.

and hole states are determined by the dimensions, morphology, and composition of the crystalline domain. Within the confines of a spherical nanocrystal (NC), the electron and hole states mirror the energy levels observed in a hydrogen atom, possessing S, P, D, and F symmetries, as demonstrated schematically in Figure 1.2.[4] Additionally, the spherical symmetry of the atomic lattice determines the quantum-confined states' degeneracy. Nanocrystals of a majority of II−VI and III−V semiconductors, commonly characterized by wurtzite and zinc blende lattices, possess $1S_e$, $1P_e$, and $1D_e$ states with 2-, 6-, and 10-fold degeneracy respectively.[5] In a charge-neutral NC, the highest occupied ($1S_h$) and lowest unoccupied ($1S_e$) states are separated by an energy gap, and the excited state is usually not thermally accessible at room temperature. This energy gap, akin to the bandgap in extended crystalline solids, is dictated by the nanocrystal size R, and can be

estimated from its bulk bandgap (E_g) and the effective masses of both electrons (m_e) and holes (m_h) following the Brus equation:[5]

$$E = E_g + \frac{\hbar^2 \pi^2}{2R^2}\left(\frac{1}{m_e} + \frac{1}{m_h}\right) - \frac{1.8e^2}{\epsilon R}$$

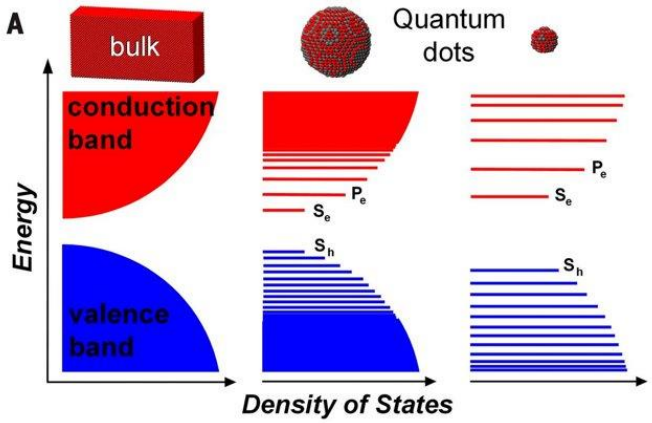

Figure 1.2. Schematic illustration of the Quantum Confinement effect.
Electron and hole energy states undergo discretization as the carrier wavefunctions are confined within the physical dimensions of a nanocrystal. Reproduced with permission from Kagan, C. R. *et al. Science* **2016**, *353* (6302), aac5523. Copyright 2016, American Association for the Advancement of Science.[4]

Size-dependent absorption and emission spectra of a few canonical examples of colloidal II-VI,[6-13] III-V,[14-17] and IV-VI[18-20] semiconductor nanocrystals, also known as quantum dots, have been extensively documented in the literature. A tunable electronic structure in tandem with a high luminescence efficiency in the visible spectrum renders colloidal quantum dots (CQDs) particularly appealing as solution-processable next-generation emitters for display applications.

1.2. InP nanocrystals as emitters.

Emitters for displays require a few specific attributes: high photoluminescence (PL) quantum yield to maximize device external quantum efficiency and a narrow emission linewidth for an expansive color gamut with accurate color representation. Additionally, luminescence stability under harsh

cycling conditions is essential for extending the lifespan of display devices. Among colloidal semiconductor nanocrystals emitting in the visible spectral range, cadmium selenide (CdSe)-based systems belonging to the II-VI class of binary semiconductors, are the most well-studied and have been thoroughly optimized.[21-24]

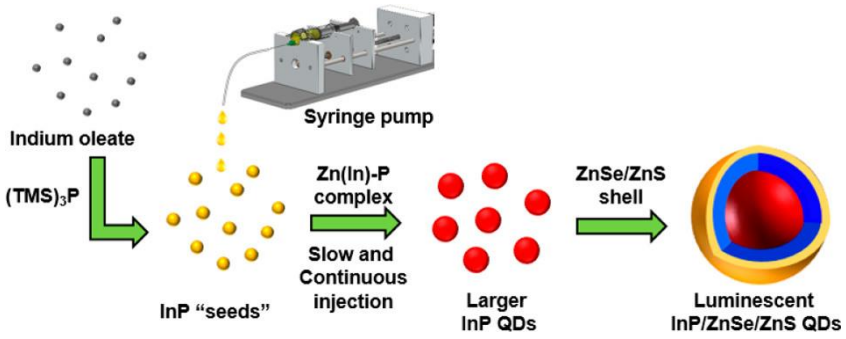

Figure 1.3. Schematic for continuous injection of InP clusters.
Continuous injection of pre-formed InP clusters to yield larger InP nanocrystals with minimal size polydispersity. Reprinted (adapted) with permission from Ramasamy, P. *et al. Chem. Mater.* **2018,** *30* (11), 3643-3647. Copyright 2018, American Chemical Society.[25]

Only recently has there been a significant push toward developing Cd-free non-toxic alternatives in this space for unrestricted incorporation in consumer electronics, and InP-based III-V CQDs have emerged as a viable candidate. Instead of an initial burst of nucleation at the early stages of the reaction, nucleation takes place continuously during InP nanocrystal synthesis; whereas growth is limited by the attachment of monomers and slows down with an increase in nanocrystal size.[26-27] This distinct kinetic behavior still results in narrow size distributions, despite its departure from the traditional LaMer model.[28] Established InP nanocrystal synthesis techniques utilize this to tune the size of quantum dots (QDs) via continuous injection of pre-formed InP clusters, resulting in minimal size polydispersity (Figure 1.3).[25] Overgrowing wide band gap semiconductors as a shell around the QD core has proven to be one of the most successful surface passivation techniques to improve the PL quantum yield (PLQY) of colloidal nanocrystals.[29-30] This type-I heterostructure

confines electrons and holes within the core, effectively isolating charge carriers from surface trap states. Most synthetic methods for highly luminescent CQD heterostructures typically entail sequential growth of multiple shells to finely adjust the band alignment and reduce lattice mismatch at the core-shell interface.[31-32] These usual strategies have been successfully implemented to yield red[33] and green-emitting[34] InP/ZnSe/ZnS CQDs with >95% PLQY, narrow emission linewidths and a near-optimal device external quantum efficiency (EQE). However, a functional electroluminescent device necessitates the development of emitters covering all three primary colors: red, green, and blue. To achieve blue emission, the sizing curve of InP based on confinement effects dictates that the nanocrystals be as small as 1.8 nm.[35-36] Such minuscule sizes are inherently unstable with detrimental non-radiative processes like rapid Auger recombination becoming increasingly dominant.

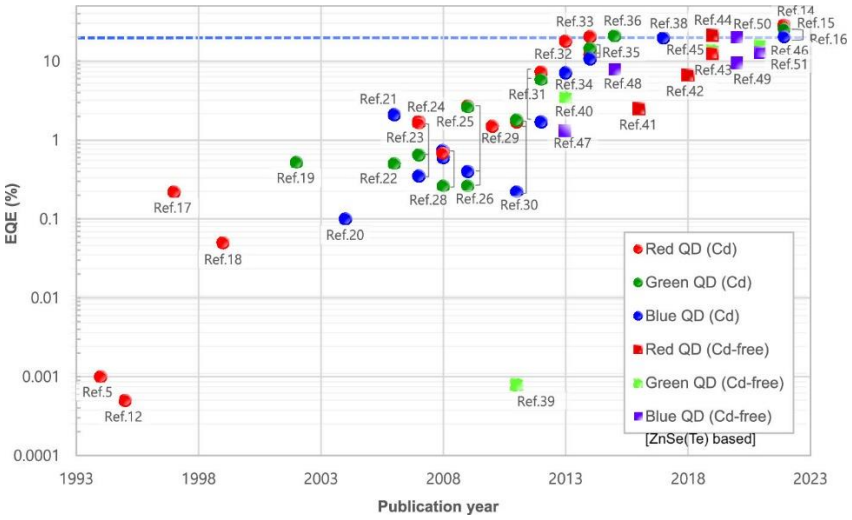

Figure 1.4. Progress in attainable external quantum efficiencies (EQEs) in QD-LEDs.
Representative device EQEs for emitters across the three primary colors. The reference numbers are as they appear on the original article, and are not related to the bibliography presented here. Reprinted (adapted) with permission from Jang, E.; Jang, H., *Chem. Rev.* **2023**, *123* (8), 4663-4692. Copyright 2023 American Chemical Society.[37]

Consequently, blue emission from Cd-free CQDs is primarily limited to ZnSe(Te)-based II-VI semiconductors,[38] as summarized in terms of progress in attainable device external quantum

efficiencies (EQE) in Figure 1.4.[37] The scientific community has yet to achieve stable blue emission from III-V CQDs.

1.3. Molten halide salts as reaction medium to process III-V nanocrystals.

InP and other III–V compound semiconductors stand as the material of choice for a myriad of electronic and optoelectronic applications due to several remarkable attributes, including high carrier mobilities and direct band gaps. These applications span a wide spectrum, encompassing high-performance transistors,[39-41] efficient photovoltaic cells,[42-44] and light-emitting diodes (LEDs).[45] The evolution of epitaxial growth techniques, such as molecular beam epitaxy,[46] metal-organic chemical vapor deposition (MOCVD),[47] and pulsed laser deposition[48] have facilitated the growth of single-crystalline III–V thin films tailored for various device applications. Unfortunately, the achievements in this realm have not yet extended to the domain of solution-processable III-V nanocrystals. The III-V bonds are predominantly covalent and rigid, making it difficult to achieve microscopic reversibility for defect-free crystal growth, except at elevated temperatures inaccessible to traditional organic solvents. Additionally, the precursors are severely prone to oxidation and often too reactive, leading to the accumulation of crystalline defects.

Our group introduced molten salt processing as a novel approach to address persistent challenges encountered in the synthesis of III-V QD materials.[49-50] Molten inorganic salts serve as robust, high-temperature solvents with a wide electrochemical window, rendering them inert matrices for a range of synthetic processes.[51] Recent research has demonstrated that it's possible to disperse NCs in various molten salts, where the specific chemical interactions between the NC surface and the salt matrix induce a restructuring of the molten salt ion template around the NCs, effectively creating a barrier that prevents direct contact between the NC surfaces.[52] As a result,

the NCs are safeguarded against undesired sintering, even at elevated temperatures. Furthermore, alkali halide salt melts are rigorously oxygen-free, and have been successfully employed for the synthesis of oxidation-prone ceramic materials directly in air.[53] This unique environment proves to be exceptionally well-suited for conducting synthetic transformations involving III-V QDs.

Molten salts fall into different categories based on the Lewis acidity of the salt melt. Lewis basic salts consist of ions that act as electron donors and alkali halide eutectics are common examples. In contrast, Lewis acidic salts contain an excess of electron-accepting moieties, as seen in eutectic mixtures like GaI_3/KI [65:35 mol%]. When equimolar quantities of Lewis acidic and Lewis basic species react following the general equation $AX + MX_3 \rightarrow AMX_4$, they form Lewis neutral molten salts. These neutral salts possess a unique molecular structure distinct from that of their parent compounds. A fourth different type of molten salt containing the reduced $Ga^{(I)}$ species can be produced by reacting an equimolar mixture of Ga metal and GaI_3, that is nominally Ga_2I_4 /$Ga^{(I)}Ga^{(III)}I_4$. The decomposition pathway for the pnictide phases present in III-V nanocrystals, is oxidative and affected by the electrochemical window offered by the molten halide salt phase. In the three subsequent chapters of this dissertation, we have utilized three different iodide-based halide salt melts to perform In-to-Ga cation exchange on InP nanocrystals; the Lewis acidic GaI_3/KI [65:35 mol%] eutectic mixture, Lewis neutral $KGaI_4$ and the reduced Ga_2I_4 salt. A comparison of the reduction potentials shows that an arsenide phase such as InAs is more easily oxidized than its phosphide counterpart InP,[54] making an alloyed arsenide-phosphide phase the ideal model system to ascertain chemical stability of the phosphide phase in these different molten salts.

$$P(white) + 3H^+ + 3e^- \rightleftharpoons PH_3\,(g)\ ,\ E^o = -0.063V$$

$$As + 3H^+ + 3e^- \rightleftharpoons AsH_3\,(g)\ ,\ E^o = -0.608V$$

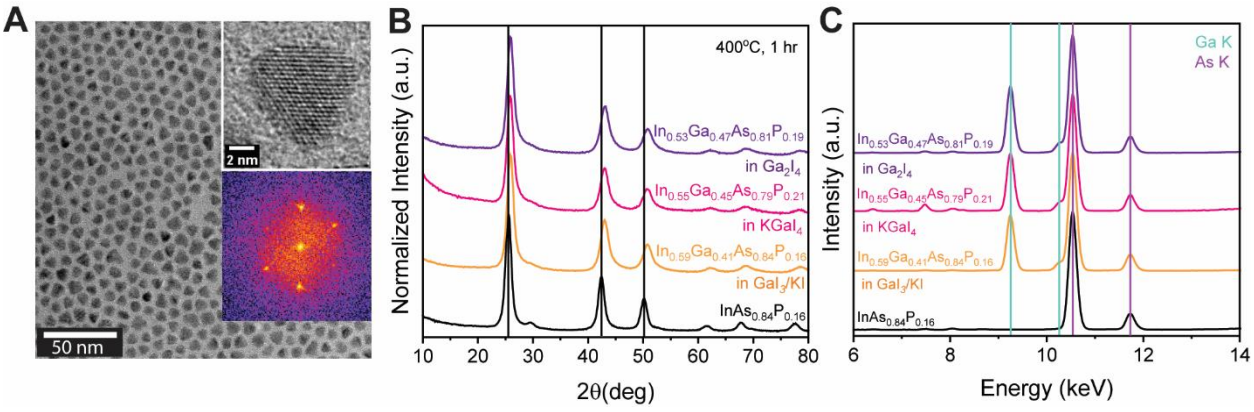

Figure 1.5. Chemical stability of an alloyed InAsP phase in different molten halide salts.
(A) TEM image of the as-synthesized highly crystalline $InAs_{0.84}P_{0.16}$ phase, High-Resolution TEM image inset. (B) PXRD patterns of the cation-exchange products from the three distinct iodide salt melts. (C) XRF elemental analysis in the mid-Z region indicates similar gallium uptake.

We synthesized colloidal $InAs_{0.84}P_{0.16}$ nanocrystals according to an established procedure. The as-synthesized tetrahedral indium arsenide-phosphide nanocrystals are highly crystalline, with an average edge length of ~9.5 nm as observed in the associated Transmission Electron Microscopy (TEM) image (Figure 1.5A). The native organic ligands were exchanged with Z-type GaI_3 ligands, and the ligand-exchanged particles were dispersed in these three different iodide-based salt melts in separate sealed quartz ampoules. We could achieve general colloidal stability of the particles in all three salts. They were annealed at 400°C for an hour, and then the cation-exchanged particles were recovered with oleylamine ligands as a colloidal solution in toluene. The detailed methodology is described in the subsequent chapters. X-Ray diffraction studies indicate that we are able to recover nanocrystalline zinc blende phase-pure products in all three cases (Figure 1.5B), whereas X-Ray Fluorescence based elemental analysis indicates that the extent of gallium incorporation remains mostly unchanged (Figure 1.5C). These observations indicate that although the chemical environments are distinct, the three molten-salt mediated In-to-Ga cation exchange reaction conditions would generally be applicable to the oxidatively more stable phosphide phase.

1.4. Thesis motivation.

Achieving blue emission from InP nanocrystals is challenging, as it requires the nanocrystals to be as small as 1.5 nm according to the sizing curve based on confinement effects.[35-36] Such minuscule sizes are inherently unstable and prone to detrimental non-radiative processes, such as rapid Auger recombination. The associated synthetic difficulties have forced the research community to resort to sub-optimal synthetic strategies, such as surface etching[55-56] or aliovalent doping of larger pre-formed InP nanocrystals with Zn^{2+} or Cu^{2+} cations to achieve blue emission.[31, 57-58]

In their bulk form, GaP, an indirect-band-gap semiconductor (E_g = 2.26 eV),[59] possesses a larger bandgap than InP, a direct-band-gap semiconductor (E_g = 1.34 eV).[60] Consequently, alloying InP nanocrystals with GaP produces ternary III-P phases with a larger bandgap and bluer emission while maintaining a larger size. In recent works, our group prepared ternary III–V phases from InP nanocrystals capped with sulfide ligands by annealing them at high temperatures in a molten salt mixture of LiBr/KBr/CsBr + GaI_3 forming $In_{1-x}Ga_xP$.[49] We further explored the role of nanocrystal surface chemistry on the reactivity of InP nanocrystals in LiBr/KBr/CsBr and LiI/KI eutectic mixtures.[61] These observations indicate that in the absence of added GaI_3, chalcogenide surface ligands were key to suppressing undesirable ripening at elevated temperatures.

Here, we build upon our success in using Z-type inorganic gallium halide ligands for molten salt-mediated cation exchange. This procedural modification avoids concerns regarding the presence of chalcogenide atoms, which may deleteriously affect their optical performance. Next, we use this chalcogenide-free molten salt system to systematically study and understand the effect of cation exchange on particle morphology and the kinetics of In-to-Ga cation exchange.[62]

In their bulk form, InP and GaP are miscible at all proportions. At ~75% gallium content the Γ and X valleys of the conduction band cross in energy, and bulk $In_{1-x}Ga_xP$ exhibits indirect behavior at higher gallium contents.[63] The effect of quantum confinement on the exciton oscillator strength in $In_{1-x}Ga_xP$ nanocrystals as a function of size and composition has not been systematically studied. Here, we develop a ZnS shelling protocol to passivate the surface of the molten-salt-derived $In_{1-x}Ga_xP$ nanocrystals while rigorously avoiding oxygen-containing precursors. This yields high-quality samples, which enables us to spectroscopically probe the changes in optoelectronic properties as Ga content is varied.[64] Since high gallium contents result in low oscillator strength of emissive states, these results inform us that incorporating more gallium in $In_{1-x}Ga_xP$/ZnS CQDs can only be a part of the strategy to prepare blue III-P emitters.

We next extend these design principles to a population of small InP nanocrystals and produce $In_{1-x}Ga_xP$ QDs with a moderate Ga content. The small size of the nanocrystals allows us to strike a balance between the nanocrystal size and gallium composition in order to achieve blue emission from $In_{1-x}Ga_xP$ while maintaining the oscillator strength of direct-like Γ-to-Γ valley interband excitonic transitions. Alloying provides a better lattice constant match with ZnS, allowing us to overgrow a relatively thick shell on the $In_{1-x}Ga_xP$ cores. This carefully tuned synthetic strategy yields bright and color pure blue emission at 470 nm. A thick ZnS shell may also impose a large potential barrier to the excitons and efficiently localize them in the core, thereby preventing fast Förster resonance energy transfer (FRET) pathways in electroluminescent devices.

1.5. Chapter 1 bibliography.

1. Talapin, D. V.; Lee, J.-S.; Kovalenko, M. V.; Shevchenko, E. V., Prospects of Colloidal Nanocrystals for Electronic and Optoelectronic Applications. *Chem. Rev.* **2010,** *110* (1), 389-458. DOI: 10.1021/cr900137k.

2. García de Arquer, F. P.; Armin, A.; Meredith, P.; Sargent, E. H., Solution-processed semiconductors for next-generation photodetectors. *Nat. Rev. Mater.* **2017,** *2* (3), 16100. DOI: 10.1038/natrevmats.2016.100.

3. Zherebetskyy, D.; Scheele, M.; Zhang, Y.; Bronstein, N.; Thompson, C.; Britt, D.; Salmeron, M.; Alivisatos, P.; Wang, L.-W., Hydroxylation of the surface of PbS nanocrystals passivated with oleic acid. *Science* **2014,** *344* (6190), 1380-1384. DOI: doi:10.1126/science.1252727.

4. Kagan, C. R.; Lifshitz, E.; Sargent, E. H.; Talapin, D. V., Building devices from colloidal quantum dots. *Science* **2016,** *353* (6302), aac5523. DOI: 10.1126/science.aac5523.

5. Brus, L., Electronic wave functions in semiconductor clusters: experiment and theory. *J. Phys. Chem.* **1986,** *90* (12), 2555-2560. DOI: 10.1021/j100403a003.

6. Rajh, T.; Micic, O. I.; Nozik, A. J., Synthesis and characterization of surface-modified colloidal cadmium telluride quantum dots. *J. Phys. Chem.* **1993,** *97* (46), 11999-12003.

7. Murray, C. B.; Norris, D. J.; Bawendi, M. G., Synthesis and characterization of nearly monodisperse CdE (E = sulfur, selenium, tellurium) semiconductor nanocrystallites. *J. Am. Chem. Soc.* **1993,** *115* (19), 8706-8715. DOI: 10.1021/ja00072a025.

8. Norris, D. J.; Bawendi, M. G., Measurement and assignment of the size-dependent optical spectrum in CdSe quantum dots. *Phys. Rev. B* **1996,** *53* (24), 16338-16346. DOI: 10.1103/PhysRevB.53.16338.

9. Hines, M. A.; Guyot-Sionnest, P., Bright UV-Blue Luminescent Colloidal ZnSe Nanocrystals. *J. Phys. Chem. B* **1998,** *102* (19), 3655-3657. DOI: 10.1021/jp9810217.

10. Weller, H.; Koch, U.; Gutiérrez, M.; Henglein, A., Photochemistry of Colloidal Metal Sulfides 7. Absorption and Fluorescence of Extremely Small ZnS Particles (The World of the Neglected Dimensions). *Berichte der Bunsengesellschaft für physikalische Chemie* **1984,** *88* (7), 649-656. DOI: https://doi.org/10.1002/bbpc.19840880715.

11. Rogach, A.; Kershaw, S. V.; Burt, M.; Harrison, M. T.; Kornowski, A.; Eychmüller, A.; Weller, H., Colloidally Prepared HgTe Nanocrystals with Strong Room-Temperature Infrared Luminescence. *Adv. Mater.* **1999,** *11* (7), 552-555.

12. Jeong, K. S.; Deng, Z.; Keuleyan, S.; Liu, H.; Guyot-Sionnest, P., Air-Stable n-Doped Colloidal HgS Quantum Dots. *J. Phys. Chem. Lett.* **2014,** *5* (7), 1139-1143. DOI: 10.1021/jz500436x.

13. Deng, Z.; Jeong, K. S.; Guyot-Sionnest, P., Colloidal Quantum Dots Intraband Photodetectors. *ACS Nano* **2014,** *8* (11), 11707-11714. DOI: 10.1021/nn505092a.

14. Mićić, O. I.; Cheong, H. M.; Fu, H.; Zunger, A.; Sprague, J. R.; Mascarenhas, A.; Nozik, A. J., Size-Dependent Spectroscopy of InP Quantum Dots. *J. Phys. Chem. B* **1997,** *101* (25), 4904-4912. DOI: 10.1021/jp9704731.

15. Micic, O. I.; Sprague, J. R.; Curtis, C. J.; Jones, K. M.; Machol, J. L.; Nozik, A. J.; Giessen, H.; Fluegel, B.; Mohs, G.; Peyghambarian, N., Synthesis and Characterization of InP, GaP, and $GaInP_2$ Quantum Dots. *J. Phys. Chem.* **1995,** *99* (19), 7754-7759. DOI: 10.1021/j100019a063.

16. Guzelian, A. A.; Banin, U.; Kadavanich, A. V.; Peng, X.; Alivisatos, A. P., Colloidal chemical synthesis and characterization of InAs nanocrystal quantum dots. *Appl. Phys. Lett.* **1996,** *69* (10), 1432-1434. DOI: 10.1063/1.117605.

17. Liu, W.; Chang, A. Y.; Schaller, R. D.; Talapin, D. V., Colloidal InSb Nanocrystals. *J. Am. Chem. Soc.* **2012,** *134* (50), 20258-20261. DOI: 10.1021/ja309821j.

18. Murray, C. B.; Sun, S.; Gaschler, W.; Doyle, H.; Betley, T. A.; Kagan, C. R., Colloidal synthesis of nanocrystals and nanocrystal superlattices. *IBM J. Res. Dev.* **2001,** *45* (1), 47-56. DOI: 10.1147/rd.451.0047.

19. Wehrenberg, B. L.; Wang, C.; Guyot-Sionnest, P., Interband and Intraband Optical Studies of PbSe Colloidal Quantum Dots. *J. Phys. Chem. B* **2002,** *106* (41), 10634-10640. DOI: 10.1021/jp021187e.

20. Hines, M. A.; Scholes, G. D., Colloidal PbS Nanocrystals with Size-Tunable Near-Infrared Emission: Observation of Post-Synthesis Self-Narrowing of the Particle Size Distribution. *Adv. Mater.* **2003,** *15* (21), 1844-1849. DOI: https://doi.org/10.1002/adma.200305395.

21. Chen, O.; Zhao, J.; Chauhan, V. P.; Cui, J.; Wong, C.; Harris, D. K.; Wei, H.; Han, H.-S.; Fukumura, D.; Jain, R. K.; Bawendi, M. G., Compact high-quality CdSe–CdS core–shell nanocrystals with narrow emission linewidths and suppressed blinking. *Nat. Mater.* **2013,** *12* (5), 445-451. DOI: 10.1038/nmat3539.

22. Zhou, J.; Pu, C.; Jiao, T.; Hou, X.; Peng, X., A Two-Step Synthetic Strategy toward Monodisperse Colloidal CdSe and CdSe/CdS Core/Shell Nanocrystals. *J. Am. Chem. Soc.* **2016,** *138* (20), 6475-6483. DOI: 10.1021/jacs.6b00674.

23. Bae, W. K.; Padilha, L. A.; Park, Y.-S.; McDaniel, H.; Robel, I.; Pietryga, J. M.; Klimov, V. I., Controlled Alloying of the Core–Shell Interface in CdSe/CdS Quantum Dots for Suppression of Auger Recombination. *ACS Nano* **2013,** *7* (4), 3411-3419. DOI: 10.1021/nn4002825.

24. Park, Y.-S.; Lim, J.; Klimov, V. I., Asymmetrically strained quantum dots with non-fluctuating single-dot emission spectra and subthermal room-temperature linewidths. *Nat. Mater.* **2019,** *18* (3), 249-255. DOI: 10.1038/s41563-018-0254-7.

25. Ramasamy, P.; Ko, K.-J.; Kang, J.-W.; Lee, J.-S., Two-Step "Seed-Mediated" Synthetic Approach to Colloidal Indium Phosphide Quantum Dots with High-Purity Photo- and Electroluminescence. *Chem. Mater.* **2018,** *30* (11), 3643-3647. DOI: 10.1021/acs.chemmater.8b02049.

26. McMurtry, B. M.; Qian, K.; Teglasi, J. K.; Swarnakar, A. K.; De Roo, J.; Owen, J. S., Continuous Nucleation and Size Dependent Growth Kinetics of Indium Phosphide Nanocrystals. *Chem. Mater.* **2020,** *32* (10), 4358-4368. DOI: 10.1021/acs.chemmater.0c01561.

27. Gary, D. C.; Terban, M. W.; Billinge, S. J. L.; Cossairt, B. M., Two-Step Nucleation and Growth of InP Quantum Dots via Magic-Sized Cluster Intermediates. *Chem. Mater.* **2015,** *27* (4), 1432-1441. DOI: 10.1021/acs.chemmater.5b00286.

28. LaMer, V. K.; Dinegar, R. H., Theory, Production and Mechanism of Formation of Monodispersed Hydrosols. *J. Am. Chem. Soc.* **1950,** *72* (11), 4847-4854. DOI: 10.1021/ja01167a001.

29. Dabbousi, B. O.; Rodriguez-Viejo, J.; Mikulec, F. V.; Heine, J. R.; Mattoussi, H.; Ober, R.; Jensen, K. F.; Bawendi, M. G., (CdSe)ZnS Core−Shell Quantum Dots: Synthesis and Characterization of a Size Series of Highly Luminescent Nanocrystallites. *J. Phys. Chem. B* **1997,** *101* (46), 9463-9475. DOI: 10.1021/jp971091y.

30. Hines, M. A.; Guyot-Sionnest, P., Synthesis and Characterization of Strongly Luminescing ZnS-Capped CdSe Nanocrystals. *J. Phys. Chem.* **1996,** *100* (2), 468-471. DOI: 10.1021/jp9530562.

31. Van Avermaet, H.; Schiettecatte, P.; Hinz, S.; Giordano, L.; Ferrari, F.; Nayral, C.; Delpech, F.; Maultzsch, J.; Lange, H.; Hens, Z., Full-Spectrum InP-Based Quantum Dots with Near-Unity Photoluminescence Quantum Efficiency. *ACS Nano* **2022,** *16* (6), 9701-9712. DOI: 10.1021/acsnano.2c03138.

32. Ramasamy, P.; Kim, N.; Kang, Y.-S.; Ramirez, O.; Lee, J.-S., Tunable, Bright, and Narrow-Band Luminescence from Colloidal Indium Phosphide Quantum Dots. *Chem. Mater.* **2017,** *29* (16), 6893-6899. DOI: 10.1021/acs.chemmater.7b02204.

33. Won, Y.-H.; Cho, O.; Kim, T.; Chung, D.-Y.; Kim, T.; Chung, H.; Jang, H.; Lee, J.; Kim, D.; Jang, E., Highly efficient and stable InP/ZnSe/ZnS quantum dot light-emitting diodes. *Nature* **2019,** *575* (7784), 634-638. DOI: 10.1038/s41586-019-1771-5.

34. Kim, Y.; Ham, S.; Jang, H.; Min, J. H.; Chung, H.; Lee, J.; Kim, D.; Jang, E., Bright and Uniform Green Light Emitting InP/ZnSe/ZnS Quantum Dots for Wide Color Gamut Displays. *ACS Appl. Nano Mater.* **2019,** *2* (3), 1496-1504. DOI: 10.1021/acsanm.8b02063.

35. Mićić, O. I.; Ahrenkiel, S. P.; Nozik, A. J., Synthesis of extremely small InP quantum dots and electronic coupling in their disordered solid films. *Appl. Phys. Lett.* **2001,** *78* (25), 4022-4024. DOI: 10.1063/1.1379990.

36. Micic, O. I.; Curtis, C. J.; Jones, K. M.; Sprague, J. R.; Nozik, A. J., Synthesis and Characterization of InP Quantum Dots. *J. Phys. Chem.* **1994,** *98* (19), 4966-4969. DOI: 10.1021/j100070a004.

37. Jang, E.; Jang, H., Review: Quantum Dot Light-Emitting Diodes. *Chem. Rev.* **2023,** *123* (8), 4663-4692. DOI: 10.1021/acs.chemrev.2c00695.

38. Kim, T.; Kim, K.-H.; Kim, S.; Choi, S.-M.; Jang, H.; Seo, H.-K.; Lee, H.; Chung, D.-Y.; Jang, E., Efficient and stable blue quantum dot light-emitting diode. *Nature* **2020,** *586* (7829), 385-389. DOI: 10.1038/s41586-020-2791-x.

39. del Alamo, J. A., Nanometre-scale electronics with III–V compound semiconductors. *Nature* **2011,** *479* (7373), 317-323. DOI: 10.1038/nature10677.

40. Ko, H.; Takei, K.; Kapadia, R.; Chuang, S.; Fang, H.; Leu, P. W.; Ganapathi, K.; Plis, E.; Kim, H. S.; Chen, S.-Y.; Madsen, M.; Ford, A. C.; Chueh, Y.-L.; Krishna, S.; Salahuddin, S.; Javey, A., Ultrathin compound semiconductor on insulator layers for high-performance nanoscale transistors. *Nature* **2010,** *468* (7321), 286-289. DOI: 10.1038/nature09541.

41. Kroemer, H., Heterostructure bipolar transistors and integrated circuits. *Proc. IEEE* **1982,** *70* (1), 13-25. DOI: 10.1109/PROC.1982.12226.

42. Geisz, J. F.; France, R. M.; Schulte, K. L.; Steiner, M. A.; Norman, A. G.; Guthrey, H. L.; Young, M. R.; Song, T.; Moriarty, T., Six-junction III–V solar cells with 47.1% conversion efficiency under 143 Suns concentration. *Nature Energy* **2020,** *5* (4), 326-335. DOI: 10.1038/s41560-020-0598-5.

43. Wallentin, J.; Anttu, N.; Asoli, D.; Huffman, M.; Åberg, I.; Magnusson, M. H.; Siefer, G.; Fuss-Kailuweit, P.; Dimroth, F.; Witzigmann, B.; Xu, H. Q.; Samuelson, L.; Deppert, K.; Borgström, M. T., InP Nanowire Array Solar Cells Achieving 13.8% Efficiency by Exceeding the Ray Optics Limit. *Science* **2013,** *339* (6123), 1057-1060. DOI: 10.1126/science.1230969.

44. Yoon, J.; Jo, S.; Chun, I. S.; Jung, I.; Kim, H.-S.; Meitl, M.; Menard, E.; Li, X.; Coleman, J. J.; Paik, U.; Rogers, J. A., GaAs photovoltaics and optoelectronics using releasable multilayer epitaxial assemblies. *Nature* **2010,** *465* (7296), 329-333. DOI: 10.1038/nature09054.

45. Nakamura, S.; Mukai, T.; Senoh, M., Candela-class high-brightness InGaN/AlGaN double-heterostructure blue-light-emitting diodes. *Appl. Phys. Lett.* **1994,** *64* (13), 1687-1689. DOI: 10.1063/1.111832.

46. Cho, A. Y.; Arthur, J. R., Molecular beam epitaxy. *Prog. Solid State Chem.* **1975,** *10*, 157-191. DOI: https://doi.org/10.1016/0079-6786(75)90005-9.

47. Dapkus, P. D.; Manasevit, H. M.; Hess, K. L.; Low, T. S.; Stillman, G. E., High purity GaAs prepared from trimethylgallium and arsine. *J. Cryst. Growth* **1981,** *55* (1), 10-23. DOI: https://doi.org/10.1016/0022-0248(81)90265-7.

48. Dijkkamp, D.; Venkatesan, T.; Wu, X. D.; Shaheen, S. A.; Jisrawi, N.; Min-Lee, Y. H.; McLean, W. L.; Croft, M., Preparation of Y-Ba-Cu oxide superconductor thin films using pulsed laser evaporation from high Tc bulk material. *Appl. Phys. Lett.* **1987,** *51* (8), 619-621. DOI: 10.1063/1.98366.

49. Srivastava, V.; Kamysbayev, V.; Hong, L.; Dunietz, E.; Klie, R. F.; Talapin, D. V., Colloidal Chemistry in Molten Salts: Synthesis of Luminescent $In_{1-x}Ga_xP$ and $In_{1-x}Ga_xAs$ Quantum Dots. *J. Am. Chem. Soc.* **2018,** *140* (38), 12144-12151. DOI: 10.1021/jacs.8b06971.

50. Cho, W.; Zhou, Z.; Lin, R.; Ondry, J. C.; Talapin, D. V., Synthesis of Colloidal GaN and AlN Nanocrystals in Biphasic Molten Salt/Organic Solvent Mixtures under High-Pressure Ammonia. *ACS Nano* **2023,** *17* (2), 1315-1326. DOI: 10.1021/acsnano.2c09552.

51. Zhang, H.; Dasbiswas, K.; Ludwig, N. B.; Han, G.; Lee, B.; Vaikuntanathan, S.; Talapin, D. V., Stable colloids in molten inorganic salts. *Nature* **2017,** *542* (7641), 328-331. DOI: 10.1038/nature21041.

52. Kamysbayev, V.; Srivastava, V.; Ludwig, N. B.; Borkiewicz, O. J.; Zhang, H.; Ilavsky, J.; Lee, B.; Chapman, K. W.; Vaikuntanathan, S.; Talapin, D. V., Nanocrystals in Molten Salts and Ionic Liquids: Experimental Observation of Ionic Correlations Extending beyond the Debye Length. *ACS Nano* **2019,** *13* (5), 5760-5770. DOI: 10.1021/acsnano.9b01292.

53. Dash, A.; Vaßen, R.; Guillon, O.; Gonzalez-Julian, J., Molten salt shielded synthesis of oxidation prone materials in air. *Nat. Mater.* **2019,** *18* (5), 465-470. DOI: 10.1038/s41563-019-0328-1.

54. *CRC Handbook of Chemistry and Physics*. 93rd ed.; CRC Press: Boca Raton, FL, 2012.

55. Siramdas, R.; McLaurin, E. J., InP Nanocrystals with Color-Tunable Luminescence by Microwave-Assisted Ionic-Liquid Etching. *Chem. Mater.* **2017,** *29* (5), 2101-2109. DOI: 10.1021/acs.chemmater.6b04457.

56. Lovingood, D. D.; Strouse, G. F., Microwave Induced In-Situ Active Ion Etching of Growing InP Nanocrystals. *Nano Lett.* **2008,** *8* (10), 3394-3397. DOI: 10.1021/nl802075j.

57. Yang, X.; Zhao, D.; Leck, K. S.; Tan, S. T.; Tang, Y. X.; Zhao, J.; Demir, H. V.; Sun, X. W., Full Visible Range Covering InP/ZnS Nanocrystals with High Photometric Performance and Their Application to White Quantum Dot Light-Emitting Diodes. *Adv. Mater.* **2012,** *24* (30), 4180-4185. DOI: https://doi.org/10.1002/adma.201104990.

58. Huang, F.; Bi, C.; Guo, R.; Zheng, C.; Ning, J.; Tian, J., Synthesis of Colloidal Blue-Emitting InP/ZnS Core/Shell Quantum Dots with the Assistance of Copper Cations. *J. Phys. Chem. Lett.* **2019,** *10* (21), 6720-6726. DOI: 10.1021/acs.jpclett.9b02386.

59. Onton, A.; Lorenz, M. R.; Reuter, W., Electronic Structure and Luminescence Processes in $In_{1-x}Ga_xP$ Alloys. *J. Appl. Phys.* **1971,** *42* (9), 3420-3432. DOI: 10.1063/1.1660748.

60. Williams, G. P.; Cerrina, F.; Lapeyre, G. J.; Anderson, J. R.; Smith, R. J.; Hermanson, J., Experimental study of the band structure of GaP, GaAs, GaSb, InP, InAs, and InSb. *Phys. Rev. B* **1986,** *34* (8), 5548-5557. DOI: 10.1103/PhysRevB.34.5548.

61. Hudson, M. H.; Gupta, A.; Srivastava, V.; Janke, E. M.; Talapin, D. V., Synthesis of $In_{1-x}Ga_xP$ Quantum Dots in Lewis Basic Molten Salts: The Effects of Surface Chemistry, Reaction Conditions, and Molten Salt Composition. *J. Phys. Chem. C* **2022,** *126* (3), 1564-1580. DOI: 10.1021/acs.jpcc.1c10394.

62. Gupta, A.; Ondry, J. C.; Chen, M.; Hudson, M. H.; Coropceanu, I.; Sarma, N. A.; Talapin, D. V., Diffusion-Limited Kinetics of Isovalent Cation Exchange in III–V Nanocrystals Dispersed in Molten Salt Reaction Media. *Nano Lett.* **2022,** *22* (16), 6545-6552. DOI: 10.1021/acs.nanolett.2c01699.

63. Onton, A.; Lorenz, M. R.; Reuter, W., Electronic Structure and Luminescence Processes in $In_{1-x}Ga_xP$ Alloys. *J. Appl. Phys.* **2003,** *42* (9), 3420-3432. DOI: 10.1063/1.1660748.

64. Gupta, A.; Ondry, J. C.; Lin, K.; Chen, Y.; Hudson, M. H.; Chen, M.; Schaller, R. D.; Rossini, A. J.; Rabani, E.; Talapin, D. V., Composition-Defined Optical Properties and the Direct-to-Indirect Transition in Core–Shell $In_{1-x}Ga_xP$/ZnS Colloidal Quantum Dots. *J. Am. Chem. Soc.* **2023,** *145* (30), 16429-16448. DOI: 10.1021/jacs.3c02709.

2. Diffusion-Limited Kinetics of Isovalent Cation Exchange in InP Nanocrystals Dispersed in Molten Salt Reaction Media

2.1. Introduction to In-to-Ga cation exchange in InP nanocrystals.

Colloidal quantum dots (QDs) constitute an important class of optoelectronic materials widely explored for display applications[2-4] To date, colloidal quantum dots made of II-VI materials have shown the best optical performance in terms of near unity photoluminescence quantum yield and narrow emission linewidth.[5-7] The same level of performance has not been universally achieved for the class of III-V colloidal nanocrystals. There are several reasons, however, to develop colloidal routes to III-V nanocrystals including lower toxicity,[8] and impressive optoelectronic performance achieved when grown by CVD and MBE methods.[9-12] Synthetic efforts to improve solution-synthesized III-V materials face several challenges. For example, typical precursors are very reactive,[13-14] making it difficult to control nucleation and growth.[14-17] III-V chemical bonds are predominantly covalent,[13, 18-19] making high temperature processing necessary. Further, Ga and Al are extremely oxophilic,[20-21] making colloidal preparation of their pnictide phases difficult. Thus far only the In-V (V=P, As, Sb) phases have been synthesized via traditional colloidal routes with reasonable material quality.[22-28]

In recent work, our group has started addressing key challenges related to III-V semiconductors by introducing high temperature molten salt annealing (>400^{o}C) and molten salt mediated cation exchange to prepare ternary III-V phases. Initially, we used InP nanocrystals capped with sulfide ligands and processed them in a mixture of LiBr/KBr/CsBr+GaI_3 forming $In_{1-x}Ga_xP$.[29] We recently explored the role of nanocrystal surface chemistry and gallium halide

additives on the reactivity of InP nanocrystals in LiBr/KBr/CsBr and LiI/KI eutectic mixtures and found that chalcogenide surface ligands ($(NH_4)_2S$, Li_2Se, $(DDA)_2S$, *etc.*) were key to protecting the particles from undesirable ripening at elevated temperatures without added GaI_3.[1] Further, we found that nanocrystals capped with Lewis acid ligands[30] ($GaCl_3$, $InCl_3$ *etc.*) were stable against undesirable ripening or decomposition only in the presence of excess GaI_3. This procedural modification avoids concerns regarding the presence of chalcogenide atoms, which may deleteriously affect their optical performance.[31]

In this work, we build upon our success using Z-type inorganic gallium halide ligands for molten salt mediated cation exchange.[1] We replace the Lewis basic alkali halide salts with Lewis acidic salts consisting of GaI_3 and KI mixtures resulting in qualitatively better colloidal stability of the nanocrystals. Next, we use this chalcogenide-free molten salt system to systematically study the effect of cation exchange on particle morphology and the kinetics of the In-to-Ga replacement.[32] We find that the activation energy of the rate determining step in the cation exchange process is considerably lower (~1eV) compared to the activation energy measured for self-diffusion in the corresponding bulk systems.[33-35]

2.2. Impact of nanocrystal morphology on indium-to-gallium cation exchange.

We synthesized InP QDs using two distinct synthetic methods to prepare sphere- and tetrahedron-shaped InP respectively. Sphere-shaped InP QDs were synthesized from $InCl_3$ and $(TMS)_3P$ in trioctylphosphine (TOP) and trioctylphosphine oxide (TOPO) by an adaptation of the method developed by Micic *et al.*[36-37] Tetrahedron-shaped InP QDs were synthesized from $InCl_3$ and $(NMe_2)_3P$ in oleylamine following the methods developed by Hens *et al.*[38-39] After size selective precipitation, we obtained sphere-shaped particles (Figure 2.1A, B) and tetrahedron-shaped particles with relatively narrow size distributions (Figure 2.1C, D).

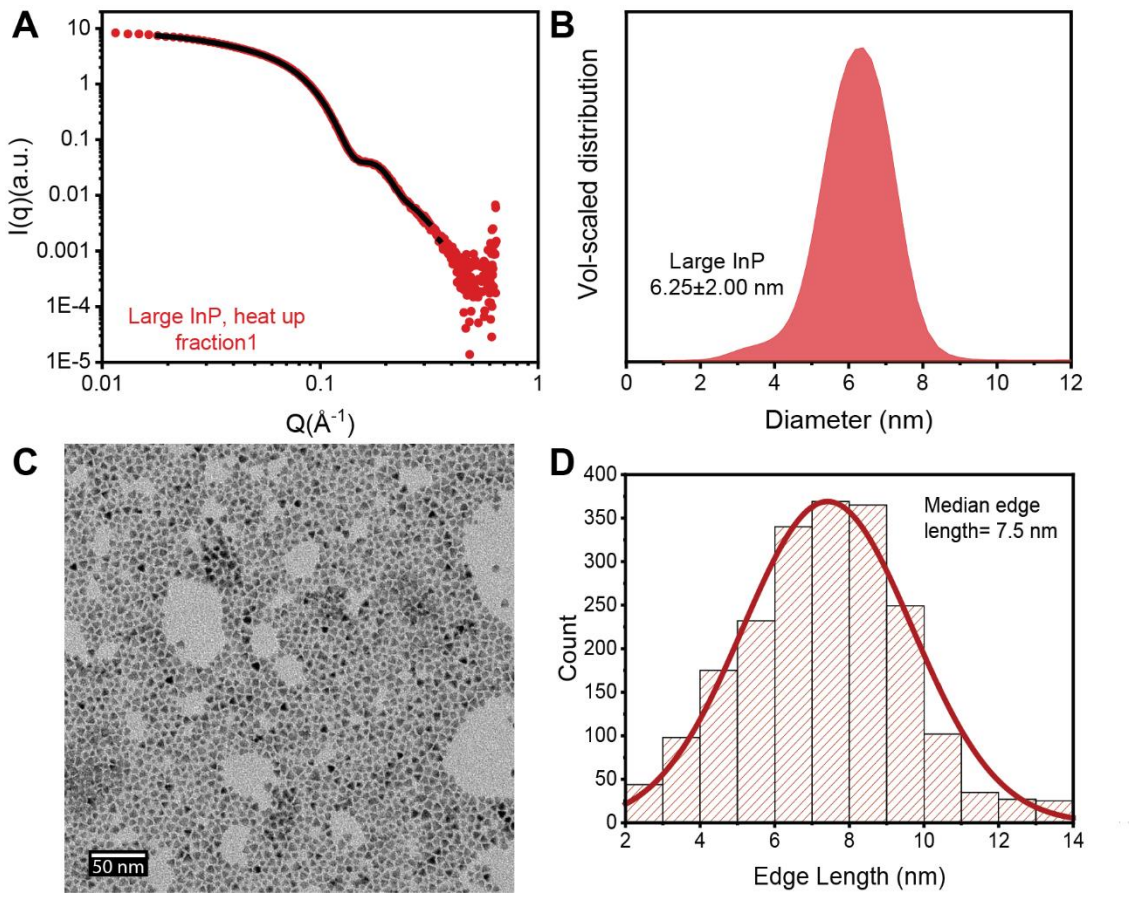

Figure 2.1. Size analysis of starting InP nanocrystal populations.
(A) Small-angle x-ray scattering (SAXS) data (red dots) and maximum-entropy fit (black line) for a solution of size-selected large spherical InP QDs. (B) Volume-scaled size distribution of the same obtained from a maximum-entropy fit to the SAXS data. (C) TEM of size-selected large tetrahedral InP QDs, and (D) the corresponding size analysis. The triangular projections on TEM were used to estimate an average edge length.

The photographs in Figure 2.2B show well-dispersed particles in the solidified molten salt, consistent with our previously determined principles for colloidal stability.[40-41] The distinct morphologies of the sphere- and tetrahedron-shaped nanocrystals provide an opportunity to explore the effect the molten salt annealing has on the shape and surface termination of the particles. TEM images of the sphere-shaped InP QDs show little evidence of particle faceting (Figure 2.2C) whereas amine/chloride passivated InP QDs show faceted particles with triangular projections consistent with a tetrahedron shape (Figure 2.2F). Following cation exchange, the

$In_{1-x}Ga_xP$ QDs produced from either sphere- or tetrahedron-shaped nanocrystals both show faceted, triangular shapes in TEM images (Figure 2.2D, G respectively). This suggests that under the molten salt cation exchange conditions at ~400 °C the QD surface can recrystallize.

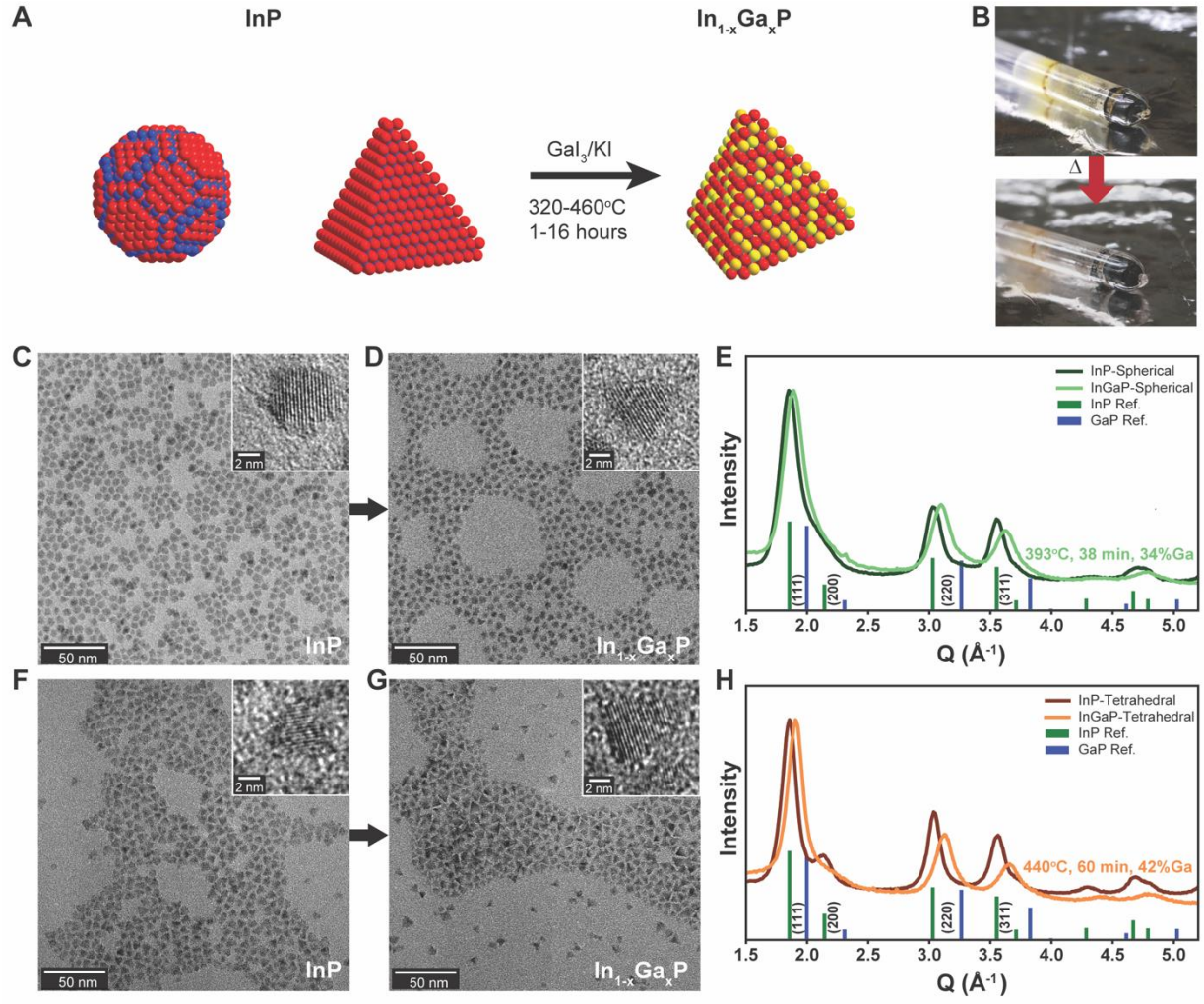

Figure 2.2. Impact of nanocrystal morphology on indium-to-gallium cation exchange.
(A) Reaction scheme outlining the transformation of sphere and tetrahedron-shaped InP nanocrystals into tetrahedron-shaped $In_{1-x}Ga_xP$ nanocrystals. (B) Representative photographs of InP nanocrystals dispersed in GaI_3/KI [65:35 mol%] eutectic molten salt (top) and the resulting $In_{1-x}Ga_xP$ after annealing (bottom). (C-E) TEM images of sphere-shaped InP nanocrystals before (C) and after (D) annealing in the molten salt reaction medium with corresponding powder X-ray diffraction patterns (E). (F-H) TEM images of tetrahedron-shaped InP nanocrystals before (F) and after (G) annealing in the molten salt reaction medium with corresponding powder X-ray diffraction patterns (H).

The preference for tetrahedral morphology in the molten iodide matrix is supported by calculations which indicate favorable interactions between halide ions and the InP (111) surface facets, suggesting tetrahedral particles are the thermodynamically favored shapes of III-V nanocrystals in molten halide salts.[42] The change in morphology for initially spherical particles also suggests the phosphide sublattice is mobile, which may have important consequences related to the kinetics of the In-to-Ga cation exchange discussed below.[43-45] Cation exchange in both sphere- and tetrahedron-shaped InP QD samples yields $In_{1-x}Ga_xP$ QDs, as evidenced by a shift of the XRD peaks to higher angles indicating a decreased lattice constant (Figure 2.2E, H) and a corresponding blue shift in the absorbance onset (Figure 2.3). Based on the lattice constants measured with XRD, we estimate the QD composition to be $In_{0.66}Ga_{0.34}P$ for the initially spherical particles and $In_{0.58}Ga_{0.42}P$ for the initially tetrahedron-shaped particles.

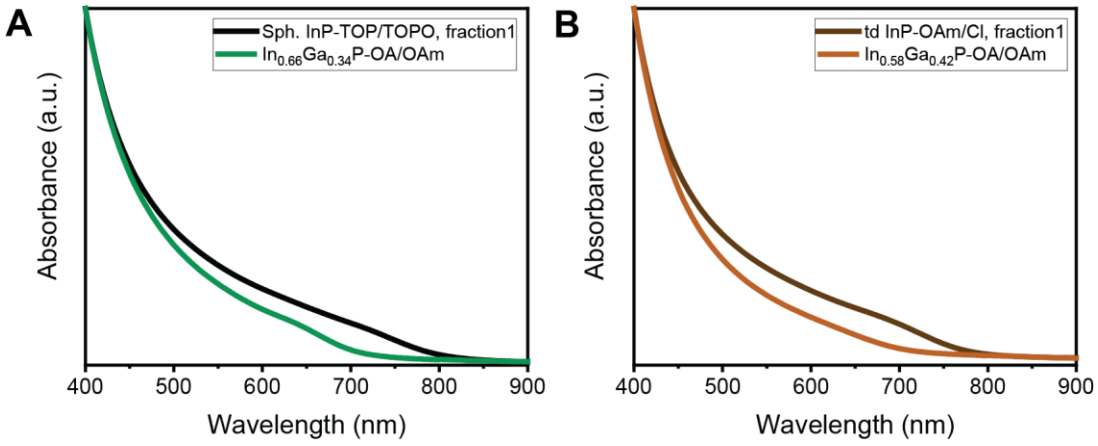

Figure 2.3. Optical characterization of the cation exchange.
A blue shift of the absorption onset observed after In^{3+} to Ga^{3+} cation exchange was performed on (A) large spherical InP QDs over an annealing duration of 28 min at 393ºC and (B) large tetrahedral InP QDs over an annealing duration of 60 min at 440ºC in a eutectic iodide molten salt medium.

2.3. Kinetics of In-to-Ga cation exchange in spherical InP nanocrystals.

The chemical bonding in III-V semiconductors is predominantly covalent.[13, 18-19] As a result, cation diffusion in bulk InP or GaP crystals is slow, characterized by a large activation energy and small diffusion coefficients. Studies on the diffusion of Ga^{3+} into bulk InP at the temperature ranges considered here are unavailable, so instead we extrapolate the reported self-diffusion coefficients to our working temperatures.[33-34] Based on this, the self-diffusion coefficient would be on the order of 10^{-24} cm^2/s for InP at our working temperature,[1] requiring ~32 years to incorporate 50% Ga into a 6.25 nm particle at 400°C. This would indicate that Fickian diffusion for In-to-Ga cation exchange would be extremely slow at present reaction conditions. Yet we observe substantial alloying even at low temperatures, indicating that the pertinent mode of mass transport during molten salt mediated cation exchange in III-V nanocrystals has much lower barriers to Ga incorporation than in bulk systems. Previously, we hypothesized that three distinct steps exist in isovalent cation exchange processes in InP nanocrystals.[1] The final step is the introduction of Ga^{3+}

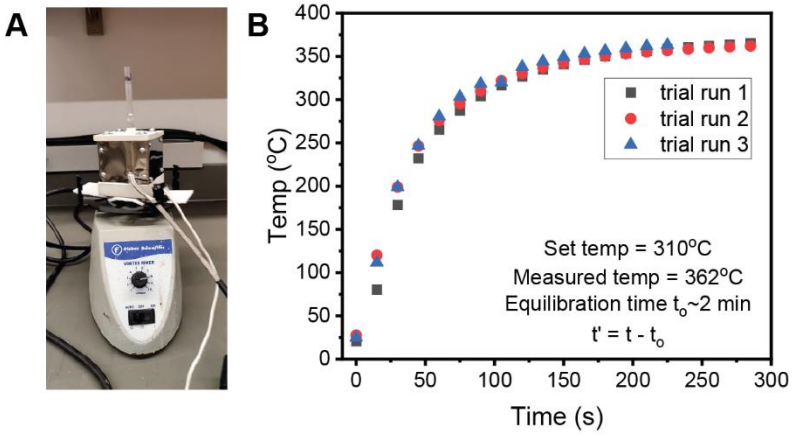

Figure 2.4. High temperature annealing setup and temperature calibration.
(A) A custom-built shaking furnace setup used for high temperature annealing of InP nanocrystals. (B) The temperature response curve of this custom-built furnace was constructed using an independent temperature probe. Based on this behavior, a temperature equilibration period of 2 min was subtracted from the recorded annealing durations.

cations into the crystal lattice and simultaneous expulsion of In^{3+} cations. This step is likely the slowest and rate determining step. Modeling this final phase within the analytical framework of the solution to Fick's second law of diffusion for spherical particles allows us to gain crucial insight into the mechanistic pathways of In-to-Ga cation exchange under diffusion limited control.

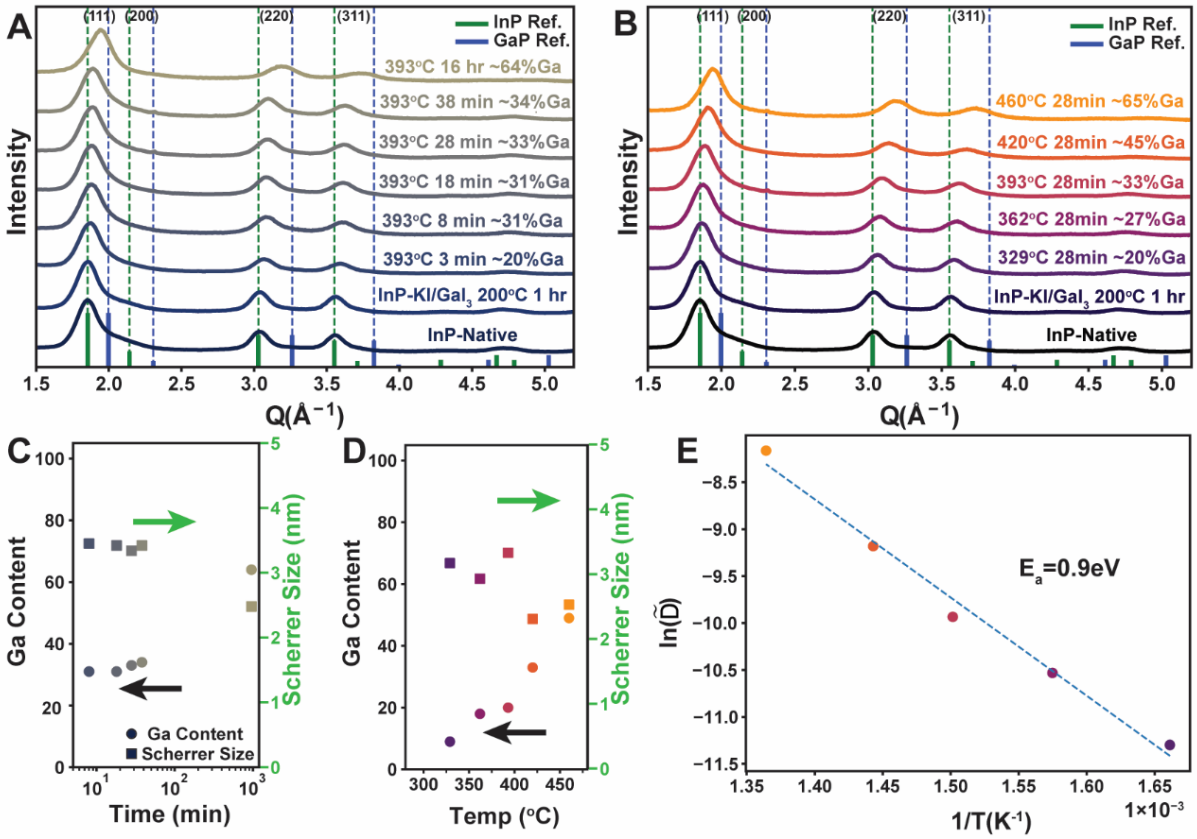

Figure 2.5. Time and temperature series data to yield kinetic factors.
Powder XRD patterns for ~6.25 nm InP nanocrystals annealed in GaI_3/KI [65:35 mol%] for different times (A) and temperatures (B). Extracted gallium content (circles) and Scherrer size (squares) for the time (C) and temperature (D) series. Arrhenius plot of the apparent diffusion coefficient measured as a function of temperature with the extracted activation energy (E).

We start with spherical InP nanocrystals with ~6.25 nm average diameter. After GaI_3 ligand exchange, the particles were dispersed in a eutectic GaI_3/KI molten salt matrix at 240°C for 1 hour, sealed inside a quartz ampoule under vacuum and annealed at different combinations of time and temperature using a custom-built shaking furnace (Figure 2.4). After cation exchange, alloyed

$In_{1-x}Ga_xP$ nanocrystals were recovered by first dissolving the salt matrix with acetonitrile. Next, the nanocrystals were treated with oleic acid and oleylamine (OA/OAm) in toluene, resulting in colloidal solutions of nanocrystals in non-polar solvents which were characterized using PXRD (Figure 2.5A-B). As expected, we observe the shift of diffraction peaks to higher momentum transfers ($Q = 4\pi\sin(\theta)/\lambda$, where 2θ is the Bragg angle and λ is X-ray wavelength, for conventional 2θ axis see Figure 2.6) for longer reaction times and higher reaction temperatures, consistent with the decrease in lattice parameter expected for higher gallium incorporation.

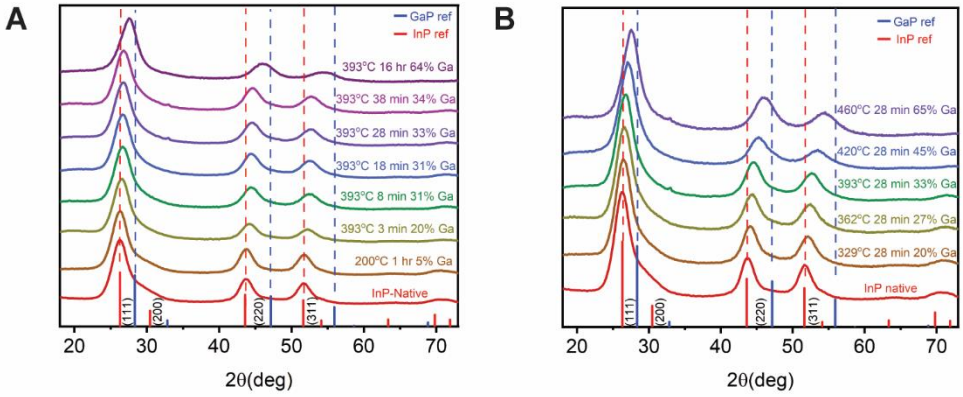

Figure 2.6. Powder XRD patterns (in the conventional 2θ axis for reference).
For ~6.25 nm InP nanocrystals annealed in GaI_3/KI [65:35 mol%] for different times (A) and temperatures (B).

To estimate lattice constants, we performed Le Bail refinement on each diffraction pattern[46] and calculated the gallium composition by linear interpolation of the composition/lattice constant from the pure bulk phases. An additional sample was prepared without the high temperature annealing step, likely restricting the In-to-Ga cation exchange only to the particle surface.

This allows us to estimate the contribution of the intermediate surface exchange step towards alloying at about ~5% of complete conversion. We found that annealing spherical InP nanocrystals at 393°C resulted in nanocrystals with gallium content ranging from 25% to 60%, with increasing

time resulting in the increased gallium incorporation (Figure 2.5A-B). This trend occurs simultaneously with a continuous blue shift of the excitonic absorption feature with increasing gallium content (Figure 2.7).

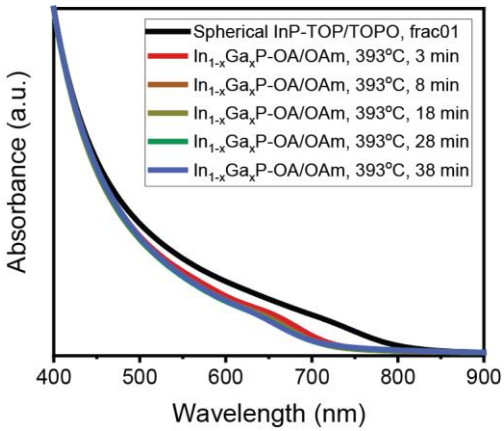

Figure 2.7. Trends in Absorption spectra.
Absorption spectra of the ~6.25 nm InP particles, along with the $In_{1-x}Ga_xP$ populations yieled by annealing at 393°C for different durations.

TEM images of these samples showed increasingly distinct faceting with longer annealing durations (Figure 2.8). Further, the faceting develops even with the shortest (3 min) annealing time, indicating that the disruption and subsequent recrystallization of the phosphide sublattice happens rather rapidly at 393°C. Notably, the average Scherrer sizes of these nanocrystals are smaller than the corresponding SAXS and TEM estimates (Figure 2.1A, B). The tetrahedron-shaped $In_{1-x}Ga_xP$ nanocrystals prepared with 1 hour of annealing time have an average edge length of ~8.5 nm via TEM (Figure 2.8), whereas the Scherrer estimate of the effective radius is 3.4 to 3.6 nm. We attribute this discrepancy to the presence of stacking faults and crystal twinning (Figure 2.9). An annealing temperature of 362°C yields similar trends (Figure 2.10) where an initially quick increase in gallium content is followed by a slower incorporation at long times.

Next, we explored the temperature dependence of gallium incorporation by annealing the samples for a fixed duration at different temperatures (Figure 2.5B). From this we extract an

effective interdiffusion coefficient $\widetilde{D}$ at each of these annealing temperatures for a reaction duration of *t* and extent of conversion *x* by utilizing the solution to Fick's second law of diffusion for a spherical particle of radius *R*.[47]

$$x = 1 - \frac{6}{\pi^2}\sum_{n=1}^{\infty}\frac{1}{n^2}exp\left(-\frac{\widetilde{D}n^2\pi^2 t}{R^2}\right)$$

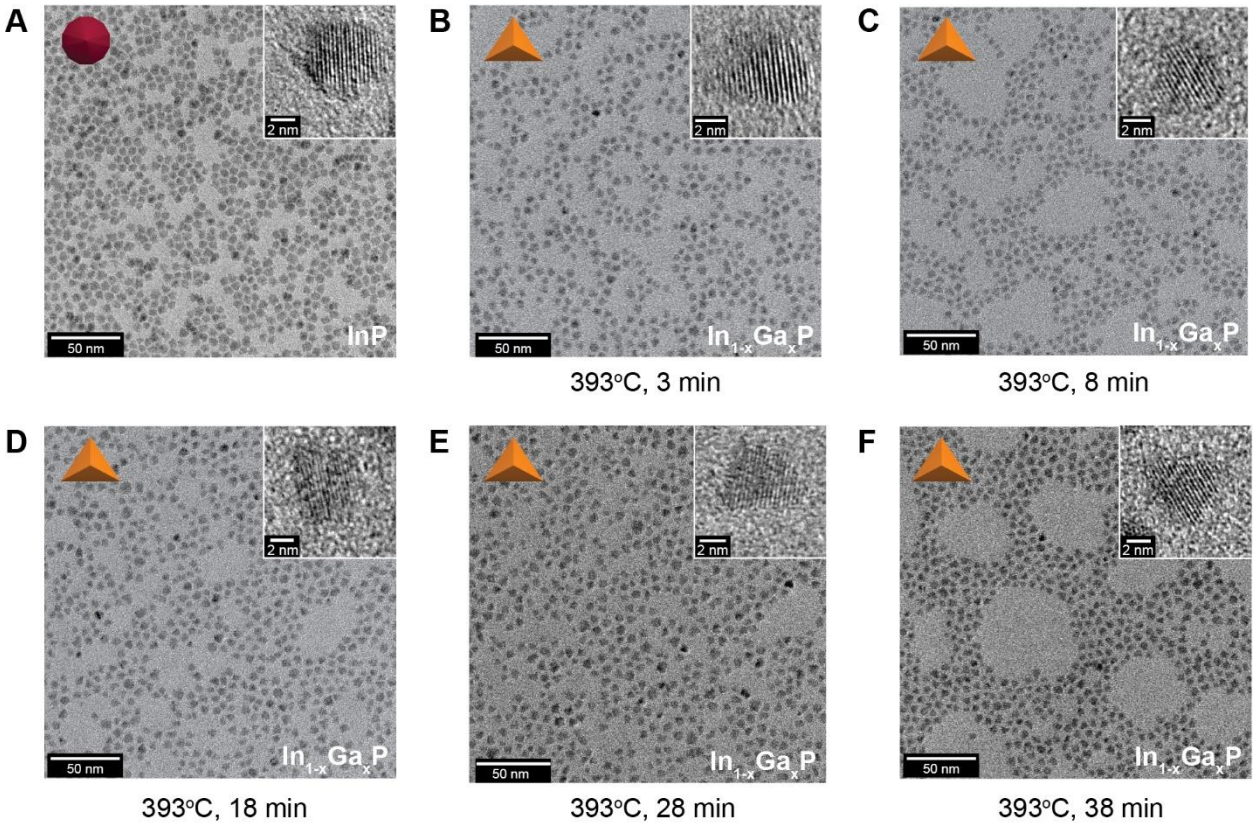

Figure 2.8. Evolution of nanocrystal morphology with time.
TEM images of the spherical ~6.25 nm InP nanocrystals (A) before and (B-F) after annealing in the GaI_3/KI eutectic molten salt reaction medium over different durations. The cation exchanged particles appear increasingly more faceted, characterized by triangular projections on TEM indicating tetrahedral morphology.

The gallium content increases monotonically with longer durations of annealing and increased temperatures according to figures 2.5C and D. As hypothesized previously, all the apparent interdiffusion coefficients extracted from the temperature series data are many orders of magnitude

larger than their self-diffusion counterpart extrapolated from the available bulk data. Assuming an Arrhenius dependence of the apparent diffusion coefficients on temperature, we were able to estimate the activation barrier towards cation exchange, E_a ~ 0.9 eV (~87 kJ/mol) as noted in Figure 2.5E. These numbers are significantly lower than the activation barrier for self-diffusion previously reported in bulk III-V semiconductors, *e.g.* 3.85 eV for In in bulk InP,[33-34] but similar in magnitude to prior reports across different II-VI and IV-VI nanocrystalline systems.[45, 48-49]

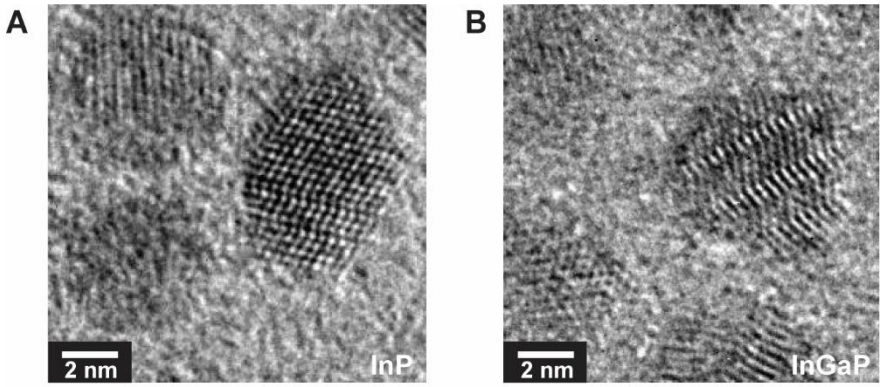

Figure 2.9. Observation of planar defects.
High-resolution TEM images confirm the frequent presence of planar defects such as twin planes and stacking faults in the (A) as synthesized large spherical InP nanocrystals and (B) alloyed $In_{1-x}Ga_xP$ nanocrystals synthesized by annealing InP in a GaI_3/KI eutectic molten salt at 393ºC for 38 min.

Several high-diffusivity pathways could be invoked to explain this deviation. As noted previously, reorganization of the phosphide sublattice into a thermodynamically more favorable morphology is expected to generate defects and thus, accelerate gallium diffusion. Additionally, these nanocrystals have stacking faults and twin defects which are known to be important low temperature diffusion pathways.[50]

To test the generality of our findings, we repeated annealing experiments on smaller InP nanocrystals with an average diameter of 4 nm (Figure 2.11). The particles were processed similarly, and the time and temperature series data under different annealing conditions are given

in Figure 2.12A-C. We observe qualitatively similar trends, in that longer reaction times and higher temperatures result in higher gallium concentration.

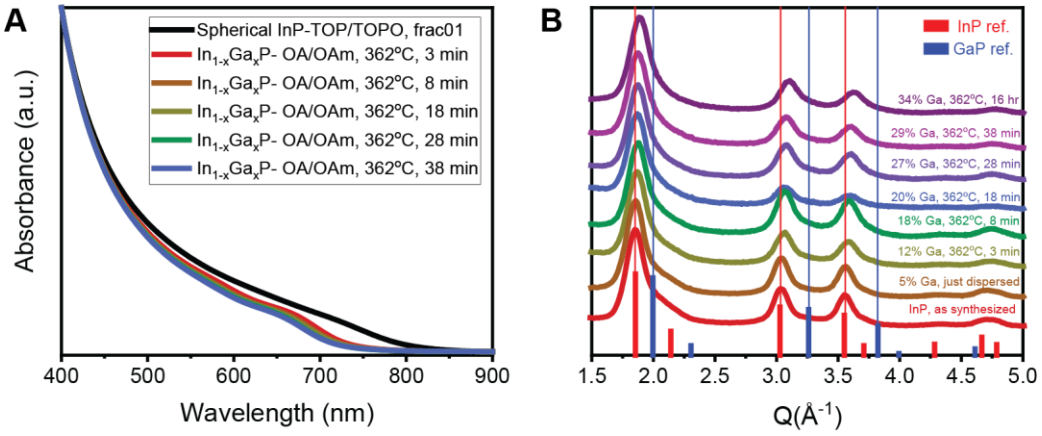

Figure 2.10. Time series data obtained at a different annealing temperature.
(A) Absorption spectra of the size-selected large spherical InP particles, along with the $In_{1-x}Ga_xP$ populations synthesized by annealing them in the molten salt reaction medium at 362°C for different durations. (B) The corresponding diffraction patterns indicate the presence of a pure zinc blende phase. The lattice constants were estimated with Le Bail refinement, and subsequently the Ga compositions were calculated using Vegard's law.

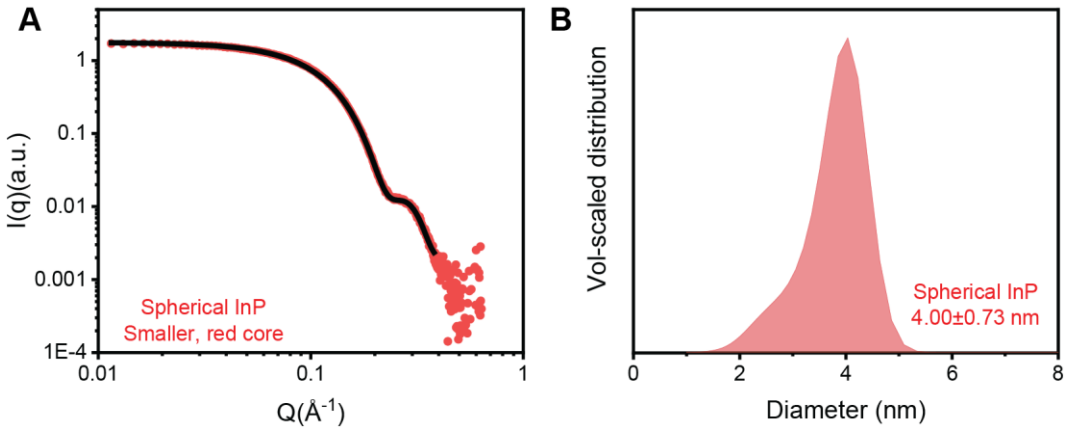

Figure 2.11. Size analysis of a different small InP population.
(A) Small-angle x-ray scattering (SAXS) data (red dots) and maximum-entropy fit (black line) for a solution of small spherical InP QDs obtained from Nanosys. (B) Volume-scaled size distribution of the same obtained from a maximum-entropy fit to the SAXS data.

The resulting Arrhenius plot deviates significantly from linearity, suggesting competing pathways at different temperatures (Figure 2.12D). These smaller InP particles have a ~60% higher surface to volume ratio relative to the ~6.25 nm particles described before. Consequently, the surface exchange or surface recrystallization processes are expected to contribute more to the kinetics in these systems.[48]

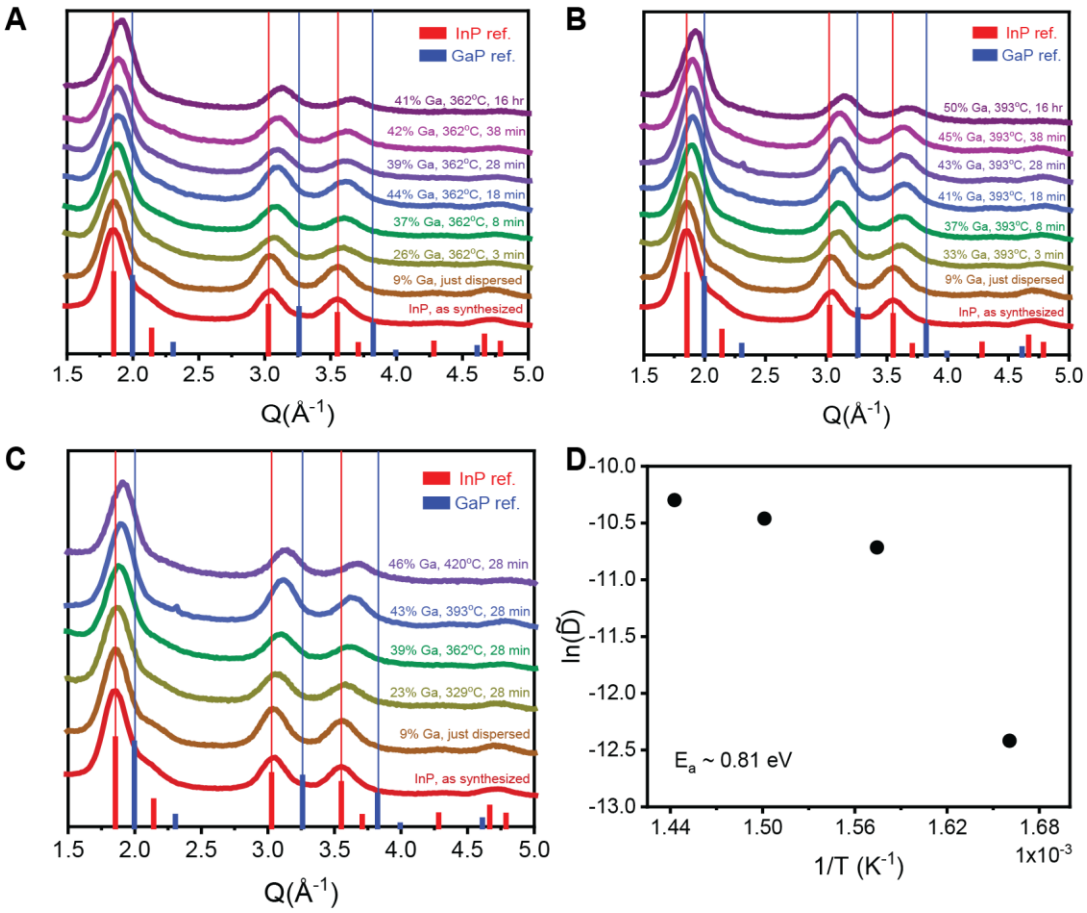

Figure 2.12. Time and temperature series data on In-to-Ga cation exchange on a different population of small InP nanocrystals.
Powder XRD patterns for ~4 nm InP nanocrystals annealed in GaI_3/KI [65:35 mol%] for different times at (A) 362°C and (B) 393°C. (C) Diffraction patterns were also recorded for particles annealed at different temperatures. The gallium content extracted from the temperature series data, was used to estimate an apparent diffusion coefficient at each temperature. (D) Arrhenius plot of the apparent diffusion coefficient measured as a function of temperature. The fit deviates from linearity significantly, rendering the extracted activation energy questionable.

2.4. Conclusions.

In this work we have carefully studied several aspects of the InP→ $In_{1-x}Ga_xP$ cation exchange reaction on nanocrystals in KI/GaI_3-based molten salts. We find that initially spherical InP nanocrystals are converted to faceted tetrahedral nanocrystals upon high temperature annealing in molten salts. Furthermore, we measured the activation energy for gallium incorporation into InP nanocrystals and found it was much lower compared to related activation energies for bulk self-diffusion. We evaluated the structure of our $In_{1-x}Ga_xP$ nanocrystals using powder XRD simulations and determined that these materials contain considerable stacking disorder present in the original InP nanocrystals which persist after the molten salt annealing. Together, our results highlight the substantial difference that exists between kinetic parameters pertaining to cation exchange in bulk and nanocrystalline III-V phases, as well as the implications of cation exchange on the morphology of III-V nanocrystals.

2.5. Materials and methods.

Chemicals. Trioctylphosphine (TOP, 97%), trioctylphosphine oxide (TOPO, 99%), and anhydrous solvents (hexane, toluene, ethanol (EtOH), isopropanol (IPA), acetonitrile (ACN)) were purchased from Sigma Aldrich and used as received. Oleylamine (OAm, technical grade, 70%) was purchased from Sigma Aldrich and purified by freezing, thawing, and then centrifuging to remove any insoluble solids. The resulting purified oleylamine was dried under dynamic vacuum at 100^{o}C overnight and stored in a nitrogen glovebox. Oleic acid (OA, 90%) was purchased from Sigma Aldrich and dried under dynamic vacuum at 100^{o}C overnight before storage in a nitrogen glove box. Potassium iodide (ultra-dry, 99.998%), gallium(iii) iodide (ultra-dry, 99.999%), hexamethylphosphorus triamide ($(NMe_2)_3P$, 97%), and N,N-dimethylformamide (DMF, anhydrous 99.9%) were purchased from Alfa Aesar and used as received. *Tris*(trimethylsilyl)

phosphine ($(TMS)_3P$, 98%, stored frozen) and indium(iii) chloride (anhydrous, 99.999%) were purchased from Strem Chemicals and used as received.

InP nanocrystal synthesis.

Small InP QDs. Small InP QDs (4 nm diameter) were obtained from Nanosys, Inc. as a solution in 1-octadecene and were stored in a nitrogen glove box. The QDs were precipitated by addition of EtOH and centrifugation, then redispersed in toluene for further processing.

Large, spherical InP QDs. Large, spherical InP QDs were synthesized by repeated applications of the procedure developed by Micic et al.[36-37] A portion of $InCl_3$ (1 g, 4.52 mmol) was dissolved in a solution of TOP (15 mL) and TOPO (1.5 g) at room temperature. This solution was filtered with a 0.2 μm PTFE syringe filter to remove undissolved solids. Half of this precursor mixture was stored separately, while the rest was loaded into a 100 mL 3-neck round-bottom flask under nitrogen. A portion of $(TMS)_3P$ (375 mg, 2 mmol) was added to the $InCl_3$ solution, and the reaction was heated at 270 °C for 30 hours. The solution was cooled down to room temperature, another portion of $(TMS)_3P$ (375 mg, 2 mmol) was added to the precursor mixture stored previously and that was added to the reaction flask. It was heated at 280 °C for another 30 hours and finally cooled down. The QDs were washed in a nitrogen glove box three times by solvent/nonsolvent (toluene/EtOH) precipitation and centrifugation. As synthesized, these InP QDs are quite polydisperse, but the size distribution could be narrowed through size-selective precipitation. Fractions of successively smaller particles were isolated by slow addition of EtOH and centrifugation. The QDs were stored as a solution in toluene. The predominant fraction of the largest particles was used for this work.

Large, tetrahedral InP QDs. Large, tetrahedral InP QDs were synthesized based on an established procedure.[38-39] In a 100 mL 3-neck round bottom flask, 442 mg $InCl_3$ (2 mmol) was dissolved in

10 mL oleylamine and degassed under dynamic vacuum at 120 °C for an hour. The solution was heated to 260 °C under nitrogen, and 1.3 mL $(NMe_2)_3P$ (7.1 mmol) was quickly injected. The reaction proceeded at 260 °C for 30 minutes and was then cooled to room temperature naturally. The particles were washed three times by solvent/nonsolvent (toluene/IPA) precipitation and centrifugation. A narrower size distribution was achieved by size-selective precipitation, where EtOH nonsolvent was slowly added to a solution of QDs in toluene and successively smaller particles were isolated by centrifugation. The QDs were stored as a solution in toluene.

Ligand exchange. Native organic ligands on the InAs and InP nanocrystals were replaced with GaI_3 using methods adapted from Dirin *et.al*.[1, 30] Briefly in a N_2 glovebox, 5ml of 0.05M GaI_3 solution in DMF was prepared in a 20ml vial and 10ml of hexane was added to create a biphasic system. The nanocrystals dissolved in hexane were added to the top phase, and the biphasic mixture was stirred for several hours until phase transfer of the nanocrystals to the lower DMF phase was complete. The DMF phase was decanted and washed three times with excess hexane. Next, the nanocrystals were precipitated using ACN, collected by centrifugation, and dispersed again in DMF. The nanocrystals were then precipitated a second time using ACN and collected as a pellet *via* centrifugation. This pellet was then washed three times with excess ACN and dried overnight in a glovebox.

Molten salt dispersion. In a N_2 glovebox, GaI_3 and KI in either 1:1 or 65:35 molar ratio were loaded into an oven-dried mortar and pestle and ground into a fine powder. For InP nanocrystals, the previously prepared dry powder of ligand exchanged nanocrystals was added to the mortar and pestle with the eutectic mixture of GaI_3 and KI in 65:35 molar ratio and ground to disperse the powder in the salt mixture. Next the nanocrystal/salt mixtures were weighed out into oven dried

quartz ampoules (9mm outer diameter 7mm inner diameter, with an indentation ~50mm from the bottom), and a 6mm diameter quartz plug was inserted. The samples were heated at 240^{o}C for 1 hour to melt the salt mixture. After melting, the ampoule was sealed using a H_2/O_2 torch under vacuum using an air free vacuum transfer chuck to mount the ampoule on a vacuum manifold without air exposure.

High temperature annealing. For InP samples, nanocrystals were annealed in a custom-built shaking furnace. The furnace consisted of ceramic walls around a central ceramic tube to hold the ampoule. The furnace was heated by a swaged heater cartridge with the temperature measured using a thermocouple and controlled using a PID temperature controller. The furnace assembly was placed atop a small vortex shaker.

Nanocrystal recovery from salt matrix. The ampoules were broken open in an N_2 glovebox, and the salt pellets embedded in the bottom of the ampoule were placed in an oven dried glass vial with a stir bar. Next, 5ml of ACN was added and stirred until the salt matrix dissolved completely. The nanocrystals were separated by centrifugation and the supernatant discarded. The nanocrystal pellet was washed with additional acetonitrile twice and recollected by centrifugation. A solution of OAm and OA in toluene (50µl/ml each) was next added to the pellet and stirred until a clear colloidal solution was obtained. The nanocrystals were then precipitated using anhydrous ethanol, followed by final dispersion in toluene.

Characterization.

Optical absorption. UV-vis spectra were collected on colloidal solutions of QDs with a Shimadzu UV-3600i Plus UV-Vis-NIR spectrophotometer in transmission mode.

Powder x-ray diffraction. Powder x-ray diffraction patterns were collected on a Rigaku MiniFlex x-ray diffractometer. Samples were deposited on (511) Si low background substrates. For $In_{1-x}Ga_xP$ nanocrystals, the lattice parameter was extracted by employing the Le Bail refinement framework to fit the full XRD pattern using the TOPAS software package (version 5, Bruker AXS). A twelfth-order Chebyshev polynomial was used to fit the background, and the crystalline phase was assumed to contain a single zinc blende phase (*F-43m* space group) exclusively. The lattice constants of bulk InP (5.8687 Å) and GaP (5.4505 Å) were used to calculate the alloy composition *x*, assuming a linear relationship between the lattice constant and alloying composition (Vegard's law) as follows:

$$a(In_{1-x}Ga_xP) = (1-x)a_{In} + xa_{Ga}$$

Le Bail refinement and multipeak fitting result in nearly identical gallium content estimations.

Transmission electron microscopy. TEM images were obtained on an FEI Tecnai F30 microscope at 300 kV.

Small-angle x-ray scattering (SAXS). Colloidal solutions of QDs in toluene were prepared in sealed Kapton capillaries for small-angle x-ray scattering (SAXS) experiments. SAXS patterns were collected using a SAXSLab Ganesha instrument with Cu Kα radiation (λ = 1.54 Å). The SAXS curves were analyzed by fitting to a quantitative model in Igor Pro using the Irena package (available at http://usaxs.xray.aps.anl.gov/staff/ilavsky/irena.html).[51] The scattering curves were fit in the particle size distribution module using the model-free Maximum Entropy approach. Based on TEM data, the particles' form factor was assumed to be that of a sphere with an aspect ratio of 1. The extracted size distributions were further fit with symmetric Gaussians to estimate average particle diameters along with the associated standard deviations.

2.6. Chapter 2 bibliography.

1. Gupta, A.; Ondry, J. C.; Chen, M.; Hudson, M. H.; Coropceanu, I.; Sarma, N. A.; Talapin, D. V., Diffusion-Limited Kinetics of Isovalent Cation Exchange in III–V Nanocrystals Dispersed in Molten Salt Reaction Media. *Nano Lett.* **2022,** *22* (16), 6545-6552. DOI: 10.1021/acs.nanolett.2c01699.

2. Moon, H.; Lee, C.; Lee, W.; Kim, J.; Chae, H., Stability of Quantum Dots, Quantum Dot Films, and Quantum Dot Light-Emitting Diodes for Display Applications. *Adv. Mater.* **2019,** *31* (34), 1804294. DOI: 10.1002/adma.201804294.

3. Shirasaki, Y.; Supran, G. J.; Bawendi, M. G.; Bulović, V., Emergence of colloidal quantum-dot light-emitting technologies. *Nat. Photonics* **2013,** *7* (1), 13-23. DOI: 10.1038/nphoton.2012.328.

4. Dai, X.; Deng, Y.; Peng, X.; Jin, Y., Quantum-Dot Light-Emitting Diodes for Large-Area Displays: Towards the Dawn of Commercialization. *Adv. Mater.* **2017,** *29* (14), 1607022. DOI: 10.1002/adma.201607022.

5. Zhou, J.; Pu, C.; Jiao, T.; Hou, X.; Peng, X., A Two-Step Synthetic Strategy toward Monodisperse Colloidal CdSe and CdSe/CdS Core/Shell Nanocrystals. *J. Am. Chem. Soc.* **2016,** *138* (20), 6475-83. DOI: 10.1021/jacs.6b00674.

6. Park, Y. S.; Lim, J.; Klimov, V. I., Asymmetrically strained quantum dots with non-fluctuating single-dot emission spectra and subthermal room-temperature linewidths. *Nat. Mater.* **2019,** *18* (3), 249-255. DOI: 10.1038/s41563-018-0254-7.

7. Chen, O.; Zhao, J.; Chauhan, V. P.; Cui, J.; Wong, C.; Harris, D. K.; Wei, H.; Han, H.-S.; Fukumura, D.; Jain, R. K.; Bawendi, M. G., Compact high-quality CdSe–CdS core–shell nanocrystals with narrow emission linewidths and suppressed blinking. *Nat. Mater.* **2013,** *12* (5), 445-451. DOI: 10.1038/nmat3539.

8. Das, A.; Snee, P. T., Synthetic Developments of Nontoxic Quantum Dots. *ChemPhysChem* **2016,** *17* (5), 598-617. DOI: 10.1002/cphc.201500837.

9. del Alamo, J. A., Nanometre-scale electronics with III–V compound semiconductors. *Nature* **2011,** *479* (7373), 317-323. DOI: 10.1038/nature10677.

10. Khan, M. A.; Van Hove, J. M.; Kuznia, J. N.; Olson, D. T., High electron mobility $GaN/Al_xGa_{1-x}N$ heterostructures grown by low-pressure metalorganic chemical vapor deposition. *Appl. Phys. Lett.* **1991,** *58* (21), 2408-2410. DOI: 10.1063/1.104886.

11. Davis, R. F., III-V nitrides for electronic and optoelectronic applications. *Proc. IEEE* **1991,** *79* (5), 702-712.

12. Jones, A. C., Developments in metalorganic precursors for semiconductor growth from the vapour phase. *Chem. Soc. Rev.* **1997,** *26* (2), 101. DOI: 10.1039/cs9972600101.

13. Allen, P. M.; Walker, B. J.; Bawendi, M. G., Mechanistic insights into the formation of InP quantum dots. *Angew. Chem. Int. Ed.* **2010,** *49* (4), 760-2. DOI: 10.1002/anie.200905632.

14. Gary, D. C.; Glassy, B. A.; Cossairt, B. M., Investigation of Indium Phosphide Quantum Dot Nucleation and Growth Utilizing Triarylsilylphosphine Precursors. *Chem. Mater.* **2014,** *26* (4), 1734-1744. DOI: 10.1021/cm500102q.

15. Franke, D.; Harris, D. K.; Xie, L.; Jensen, K. F.; Bawendi, M. G., The Unexpected Influence of Precursor Conversion Rate in the Synthesis of III–V Quantum Dots. *Angew. Chem. Int. Ed.* **2015,** *54* (48), 14299-14303. DOI: 10.1002/anie.201505972.

16. Li, Y.; Pu, C.; Peng, X., Surface activation of colloidal indium phosphide nanocrystals. *Nano Res.* **2017,** *10* (3), 941-958. DOI: 10.1007/s12274-016-1353-x.

17. Xie, L.; Shen, Y.; Franke, D.; Sebastián, V.; Bawendi, M. G.; Jensen, K. F., Characterization of Indium Phosphide Quantum Dot Growth Intermediates Using MALDI-TOF Mass Spectrometry. *J. Am. Chem. Soc.* **2016,** *138* (41), 13469-13472. DOI: 10.1021/jacs.6b06468.

18. Srivastava, V.; Liu, W.; Janke, E. M.; Kamysbayev, V.; Filatov, A. S.; Sun, C.-J.; Lee, B.; Rajh, T.; Schaller, R. D.; Talapin, D. V., Understanding and Curing Structural Defects in Colloidal GaAs Nanocrystals. *Nano Lett.* **2017,** *17* (3), 2094-2101. DOI: 10.1021/acs.nanolett.7b00481.

19. Lauth, J.; Strupeit, T.; Kornowski, A.; Weller, H., A Transmetalation Route for Colloidal GaAs Nanocrystals and Additional III–V Semiconductor Materials. *Chem. Mater.* **2013,** *25* (8), 1377-1383. DOI: 10.1021/cm3019617.

20. Tessier, M. D.; Baquero, E. A.; Dupont, D.; Grigel, V.; Bladt, E.; Bals, S.; Coppel, Y.; Hens, Z.; Nayral, C.; Delpech, F., Interfacial Oxidation and Photoluminescence of InP-Based Core/Shell Quantum Dots. *Chem. Mater.* **2018,** *30* (19), 6877-6883. DOI: 10.1021/acs.chemmater.8b03117.

21. Stein, J. L.; Holden, W. M.; Venkatesh, A.; Mundy, M. E.; Rossini, A. J.; Seidler, G. T.; Cossairt, B. M., Probing Surface Defects of InP Quantum Dots Using Phosphorus Kα and Kβ X-ray Emission Spectroscopy. *Chem. Mater.* **2018,** *30* (18), 6377-6388. DOI: 10.1021/acs.chemmater.8b02590.

22. Won, Y. H.; Cho, O.; Kim, T.; Chung, D. Y.; Kim, T.; Chung, H.; Jang, H.; Lee, J.; Kim, D.; Jang, E., Highly efficient and stable InP/ZnSe/ZnS quantum dot light-emitting diodes. *Nature* **2019,** *575* (7784), 634-638. DOI: 10.1038/s41586-019-1771-5.

23. Ramasamy, P.; Ko, K.-J.; Kang, J.-W.; Lee, J.-S., Two-Step "Seed-Mediated" Synthetic Approach to Colloidal Indium Phosphide Quantum Dots with High-Purity Photo- and

Electroluminescence. *Chem. Mater.* **2018,** *30* (11), 3643-3647. DOI: 10.1021/acs.chemmater.8b02049.

24. Kim, Y.; Ham, S.; Jang, H.; Min, J. H.; Chung, H.; Lee, J.; Kim, D.; Jang, E., Bright and Uniform Green Light Emitting InP/ZnSe/ZnS Quantum Dots for Wide Color Gamut Displays. *ACS Appl. Nano Mater.* **2019,** *2* (3), 1496-1504. DOI: 10.1021/acsanm.8b02063.

25. Zhao, T.; Oh, N.; Jishkariani, D.; Zhang, M.; Wang, H.; Li, N.; Lee, J. D.; Zeng, C.; Muduli, M.; Choi, H. J.; Su, D.; Murray, C. B.; Kagan, C. R., General Synthetic Route to High-Quality Colloidal III-V Semiconductor Quantum Dots Based on Pnictogen Chlorides. *J. Am. Chem. Soc.* **2019,** *141* (38), 15145-15152. DOI: 10.1021/jacs.9b06652.

26. Srivastava, V.; Janke, E. M.; Diroll, B. T.; Schaller, R. D.; Talapin, D. V., Facile, Economic and Size-Tunable Synthesis of Metal Arsenide Nanocrystals. *Chem. Mater.* **2016,** *28* (18), 6797-6802. DOI: 10.1021/acs.chemmater.6b03501.

27. Ginterseder, M.; Franke, D.; Perkinson, C. F.; Wang, L.; Hansen, E. C.; Bawendi, M. G., Scalable Synthesis of InAs Quantum Dots Mediated through Indium Redox Chemistry. *J. Am. Chem. Soc.* **2020,** *142* (9), 4088-4092. DOI: 10.1021/jacs.9b12350.

28. Liu, W.; Chang, A. Y.; Schaller, R. D.; Talapin, D. V., Colloidal InSb nanocrystals. *J. Am. Chem. Soc.* **2012,** *134* (50), 20258-61. DOI: 10.1021/ja309821j.

29. Srivastava, V.; Kamysbayev, V.; Hong, L.; Dunietz, E.; Klie, R. F.; Talapin, D. V., Colloidal Chemistry in Molten Salts: Synthesis of Luminescent $In_{1-x}Ga_xP$ and $In_{1-x}Ga_xAs$ Quantum Dots. *J. Am. Chem. Soc.* **2018,** *140* (38), 12144-12151. DOI: 10.1021/jacs.8b06971.

30. Dirin, D. N.; Dreyfuss, S.; Bodnarchuk, M. I.; Nedelcu, G.; Papagiorgis, P.; Itskos, G.; Kovalenko, M. V., Lead halide perovskites and other metal halide complexes as inorganic capping ligands for colloidal nanocrystals. *J. Am. Chem. Soc.* **2014,** *136* (18), 6550-3. DOI: 10.1021/ja5006288.

31. Li, Y.; Hou, X.; Dai, X.; Yao, Z.; Lv, L.; Jin, Y.; Peng, X., Stoichiometry-Controlled InP-Based Quantum Dots: Synthesis, Photoluminescence, and Electroluminescence. *J. Am. Chem. Soc.* **2019,** *141* (16), 6448-6452. DOI: 10.1021/jacs.8b12908.

32. Rusishvili, M.; Wippermann, S.; Talapin, D. V.; Galli, G., Stoichiometry of the Core Determines the Electronic Structure of Core–Shell III–V/II–VI Nanoparticles. *Chem. Mater.* **2020,** *32* (22), 9798-9804. DOI: 10.1021/acs.chemmater.0c03939.

33. Goldstein, B., Diffusion in Compound Semiconductors. *Phys Rev* **1961,** *121* (5), 1305-1311. DOI: 10.1103/PhysRev.121.1305.

34. Fisher, D. J., *Diffusion in Semiconductors, Other Than Silicon: Compilation*. Trans Tech: 2010.

35. Wang, L.; Wolk, J. A.; Hsu, L.; Haller, E. E.; Erickson, J. W.; Cardona, M.; Ruf, T.; Silveira, J. P.; Briones, F., Gallium self-diffusion in gallium phosphide. *Appl. Phys. Lett.* **1997,** *70* (14), 1831-1833. DOI: 10.1063/1.118705.

36. Langof, L.; Ehrenfreund, E.; Lifshitz, E.; Micic, O. I.; Nozik, A. J., Continuous-Wave and Time-Resolved Optically Detected Magnetic Resonance Studies of Nonetched/Etched InP Nanocrystals. *J. Phys. Chem. B* **2002,** *106* (7), 1606-1612. DOI: 10.1021/jp013720g.

37. Mićić, O. I.; Nozik, A. J.; Lifshitz, E.; Rajh, T.; Poluektov, O. G.; Thurnauer, M. C., Electron and Hole Adducts Formed in Illuminated InP Colloidal Quantum Dots Studied by Electron Paramagnetic Resonance. *J. Phys. Chem. B* **2002,** *106* (17), 4390-4395. DOI: 10.1021/jp014180q.

38. Tessier, M. D.; Dupont, D.; De Nolf, K.; De Roo, J.; Hens, Z., Economic and Size-Tunable Synthesis of InP/ZnE (E = S, Se) Colloidal Quantum Dots. *Chem. Mater.* **2015,** *27* (13), 4893-4898. DOI: 10.1021/acs.chemmater.5b02138.

39. Tessier, M. D.; De Nolf, K.; Dupont, D.; Sinnaeve, D.; De Roo, J.; Hens, Z., Aminophosphines: A Double Role in the Synthesis of Colloidal Indium Phosphide Quantum Dots. *J. Am. Chem. Soc.* **2016,** *138* (18), 5923-9. DOI: 10.1021/jacs.6b01254.

40. Zhang, H.; Dasbiswas, K.; Ludwig, N. B.; Han, G.; Lee, B.; Vaikuntanathan, S.; Talapin, D. V., Stable colloids in molten inorganic salts. *Nature* **2017,** *542* (7641), 328-331. DOI: 10.1038/nature21041.

41. Kamysbayev, V.; Srivastava, V.; Ludwig, N. B.; Borkiewicz, O. J.; Zhang, H.; Ilavsky, J.; Lee, B.; Chapman, K. W.; Vaikuntanathan, S.; Talapin, D. V., Nanocrystals in Molten Salts and Ionic Liquids: Experimental Observation of Ionic Correlations Extending beyond the Debye Length. *ACS Nano* **2019,** *13* (5), 5760-5770. DOI: 10.1021/acsnano.9b01292.

42. Kim, K.; Yoo, D.; Choi, H.; Tamang, S.; Ko, J.-H.; Kim, S.; Kim, Y.-H.; Jeong, S., Halide–Amine Co-Passivated Indium Phosphide Colloidal Quantum Dots in Tetrahedral Shape. *Angew. Chem. Int. Ed.* **2016,** *55* (11), 3714-3718. DOI: 10.1002/anie.201600289.

43. Beberwyck, B. J.; Surendranath, Y.; Alivisatos, A. P., Cation Exchange: A Versatile Tool for Nanomaterials Synthesis. *J. Phys. Chem. C* **2013,** *117* (39), 19759-19770. DOI: 10.1021/jp405989z.

44. Son, D. H.; Hughes, S. M.; Yin, Y.; Paul Alivisatos, A., Cation exchange reactions in ionic nanocrystals. *Science* **2004,** *306* (5698), 1009-12. DOI: 10.1126/science.1103755.

45. Li, Z.; Saruyama, M.; Asaka, T.; Tatetsu, Y.; Teranishi, T., Determinants of crystal structure transformation of ionic nanocrystals in cation exchange reactions. *Science* **2021,** *373* (6552), 332-337. DOI: doi:10.1126/science.abh2741.

46. Le Bail, A.; Duroy, H.; Fourquet, J. L., Ab-initio structure determination of $LiSbWO_6$ by X-ray powder diffraction. *Mater. Res. Bull.* **1988,** *23* (3), 447-452. DOI: 10.1016/0025-5408(88)90019-0.

47. J., C., *The Mathematics of Diffusion*. 2nd ed.; Oxford University Press: London, 1975.

48. Nelson, A.; Honrao, S.; Hennig, R. G.; Robinson, R. D., Nanocrystal Symmetry Breaking and Accelerated Solid-State Diffusion in the Lead–Cadmium Sulfide Cation Exchange system. *Chem. Mater.* **2019,** *31* (3), 991-1005. DOI: 10.1021/acs.chemmater.8b04490.

49. Sung, Y.-M.; Lee, Y.-J.; Park, K.-S., Kinetic Analysis for Formation of $Cd_{1-x}Zn_xSe$ Solid-Solution Nanocrystals. *J. Am. Chem. Soc.* **2006,** *128* (28), 9002-9003. DOI: 10.1021/ja061858c.

50. Shewmon, P., High Diffusivity Paths. Springer International Publishing: 2016; pp 189-222.

51. Ilavsky, J.; Jemian, P. R., Irena: Tool Suite for Modeling and Analysis of Small-Angle Scattering. *J. Appl. Crystallogr.* **2009,** *42* (2), 347-353. DOI: doi:10.1107/S0021889809002222.

3. Composition-defined Optical Properties and the Direct to Indirect Transition in Core-Shell $In_{1-x}Ga_xP$/ZnS Colloidal Quantum Dots

3.1. Introduction to the optoelectronic behavior of $In_{1-x}Ga_xP$ as a function of Ga content.

Electronic and optoelectronic devices such as transistors, photodetectors and LEDs employ high-quality semiconducting layers as the active material. In bulk semiconductors, electronic transitions must conserve both energy and momentum. This requirement divides semiconductors into two distinct families: direct-gap semiconductors, where the top of the valence band and bottom of the conduction band occur at the same point in the Brillouin zone (Γ point for typical II-VI materials like CdSe, and L points for typical IV-VI materials like PbS); and indirect gap semiconductors, where this condition is not met.[2] In sub-10 nm semiconductor nanocrystals, as the carrier wavefunctions are confined in dimensions smaller than the exciton Bohr radius, the energy gap between the highest-energy occupied and lowest-energy unoccupied states becomes a function of the particle size. The canonical examples of colloidal semiconductor nanostructures, such as CdSe nanocrystals, also known as quantum dots (QDs), show size-dependent absorption and emission spectra that are well described by particle-in-a-box models.[3] Quantum confined absorption and photoluminescence (PL) have been well documented in colloidal nanocrystals of elemental and compound semiconductors, alloys and core-shell structures.[4-7] The examples cited here are for compositions that, in their bulk form, are direct band gap semiconductors. Direct gap semiconductors generally show strong dipole-allowed interband transitions and, correspondingly, quantum dots derived from direct-gap semiconductors are characterized by strong excitonic

transitions,[8] high luminescence efficiency with fast nanosecond radiative lifetimes,[9] and state filling induced transient optical bleaching upon photoexcitation.[10-11]

In materials like silicon and germanium, which have an indirect band gap in the bulk, the effect of quantum confinement on absorption and photoluminescence is more complicated due to the momentum mismatch between the valence band maximum and conduction band minimum. In bulk crystals of these materials, absorption or emission of photons at the band gap energy requires phonons to compensate for the momentum mismatch between the conduction band minimum and valence band maximum, leading to weak band edge absorption and very weak, often undetectable photoluminescence (PL). Despite this additional factor, Si and Ge nanocrystals show size-dependent absorption onsets[12] and in some cases size-dependent PL.[13] However, the absorption spectra do not exhibit distinct excitonic features, the PL has long μs lifetimes,[13] and nanocrystals derived from indirect-gap materials do not display excitonic bleach signatures near the band edge.[14] The finite size of the crystallite relaxes, at least partially, the requirement of conservation of momentum, and mixing of the Γ and X valleys may enable direct-like absorption and emission of photons without phonon mediated processes.[15] Indeed, low temperature PL measurements on silicon nanocrystals show zero phonon emission for small particles, indicating a direct (not phonon-mediated) emission pathway is possible.[16] However, the mixing of the states is very weak and silicon remains essentially an indirect band gap material in nanocrystalline form.[10]

The two cases thus far discussed represent distinct materials classes which cannot be continuously tuned between direct and indirect behaving systems. One rather unique system where the indirect/direct nature of the transition is continuously tunable is InP - GaP.[17] InP is a direct band gap semiconductor with a valence band maximum and a conduction band minimum at the Γ point (Figure 1C).[18-19] GaP is an indirect band gap semiconductor with a valence band maximum

at the Γ point and a conduction band minimum at the X point.[19] (Figure 1A) These two materials form solid solutions at all compositions: alloying increases the energy of the Γ point conduction band minimum and lowers the energy of the X point conduction band minimum. At a bulk composition of ~75% gallium, the Γ and X points of the conduction band cross in energy resulting in a change in slope of the band gap vs composition relationship (Figure 1B), and $In_{1-x}Ga_xP$ exhibits indirect behavior at higher gallium contents.[20]

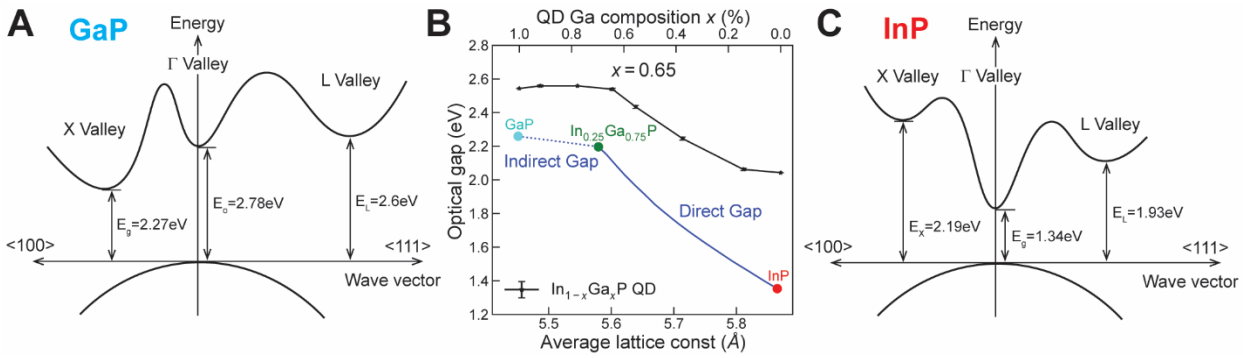

Figure 3.1. Band diagrams of bulk phase InP and GaP and the direct-to-indirect transition. Band structure of bulk (A) GaP and (C) InP. (B) Composition dependence of band gap and lattice constant in bulk alloyed $In_{1-x}Ga_xP$ crystals at 300 K (blue line) from previously reported data in ref 36, 37. Theoretical predictions for the composition dependence of the band gap for 4 nm diameter $In_{1-x}Ga_xP$ nanocrystals (black Squares) calculated using a semi-empirical pseudopotential model. Panel A was adapted with permission from reference 17 (Copyright 1971 American Physical Society). Panel C was adapted with permission from reference 19 (Copyright 1986 American Physical Society).

The effect of quantum confinement on the $In_{1-x}Ga_xP$ QDs as a function of size and x-value has not been systematically studied. In particular, it is not clear how quantum confinement affects the nature of the composition determined direct-to-indirect transition. For Stranski-Krastanov (SK) grown epitaxial QDs, since strain is the driving force for island formation, it is difficult to synthesize materials with independent control over size and composition.[21] Moreover, SK QDs are typically larger than the Bohr exciton radius and thus lie within the weak confinement regime, minimizing any potential Γ-X mixing which may occur due to strong quantum confinement.

Quantum confined nanowire or nanorod structures grown *via* epitaxial techniques or solution techniques have more flexibility in tuning size and composition independently, but achievable dimensions are still too large to achieve strong quantum confinement in this material system.[22-24]

Solution phase colloidal synthesis is an ideal method for preparing small semiconductor crystallites with strong quantum confinement due to precisely controllable nucleation and growth kinetics. These methods have been well developed for II-VI, IV-VI and In-Pn (Pn = P, As, Sb) materials. However, due to the high reactivity of gallium towards organic solvents at high temperatures,[25] synthesis of high-quality Ga-Pn and $In_{1-x}Ga_xPn$ materials is not well developed. Currently, there are many established routes to high-quality InP[26-29] with control over size and morphology, which result in bright emissive semiconductors, while only a few routes to colloidal GaP[30-31] have been reported. There are a select few examples of $In_{1-x}Ga_xP$ particles that have been prepared via colloidal growth methods. However, based on reported data, the uniform incorporation of gallium into the InP lattice has not been unambiguously verified.[32-33] The lack of general control over composition and size in these systems limits their utility for studying the fundamentals of the direct-to-indirect transition in quantum-confined $In_{1-x}Ga_xP$.

Recently, our group has developed methods to prepare stable colloids in molten salt solvents[34-35] and used these solvents as a high temperature reaction medium for preparing ternary $In_{1-x}Ga_xP$ and $In_{1-x}Ga_xAs$ colloidal nanocrystals.[36-38] In this synthetic approach we start with InP or InAs nanocrystals, where we can leverage their well-developed size control methods, and disperse the nanocrystals in a gallium-containing molten salt solvent. High temperature annealing of the InP/molten salt mixture causes solid state diffusion of gallium into the InP lattice with coupled out-diffusion of the In, leading to $In_{1-x}Ga_xP$ nanocrystals. The temperature and duration of annealing can be used to control the degree of gallium incorporation independent of particle size.

The high temperature stability and rigorously oxygen-free environment enabled by the molten salts further enable study of the $In_{1-x}Ga_xP$ without oxidation from decomposition of oxygen-containing ligands or atmospheric contamination.

In this work we synthesize a series of $In_{1-x}Ga_xP$ nanocrystals where we vary the diameter from 3.2 to 4.9 nm and x-value from 0 to 0.92. We use solid state NMR to validate that the molten salt derived nanocrystals have minimal surface oxidation and that In and Ga are alloyed uniformly within the nanocrystals rather than forming a distinct core-shell morphology. To fully exploit the oxygen-free nature of the molten salt derived $In_{1-x}Ga_xP$ nanocrystal surface, we develop a ZnS shelling protocol which rigorously avoids oxygen or oxygen containing precursors. We show that the resulting $In_{1-x}Ga_xP$/ZnS colloidal nanocrystals in the x=0.14-0.57 can display PL quantum yields (PLQY) as high as 89% with PL linewidths of 57 nm FWHM. Optoelectronic characterization *via* time-resolved PL (TRPL) and transient absorption spectroscopy on the resulting $In_{1-x}Ga_xP$/ZnS nanocrystals suggest that the oscillator strength of the emissive state decreases as gallium content is increased. Further, theoretical calculations via the atomistic semi-empirical pseudopotential methods were used to capture the electronic structure of the alloyed QD systems. Calculated optoelectronic properties, including optical gaps, absorption spectra and radiative lifetimes show good agreement with experimental measurements, capturing the trend as gallium content increases in alloyed $In_{1-x}Ga_xP$ QDs. Fluence-dependent transient absorption shows that the Auger recombination rate is not strongly modulated by composition; rather, well-established volume scaling dominates multiexciton physics in these quantum-confined nanocrystals. In $In_{1-x}Ga_xP$/ZnS samples with x=0.65-0.92, we show that the excitonic bleach feature disappears for samples which contain >65% gallium, consistent with conversion of the $In_{1-x}Ga_xP$/ZnS to an indirect band gap material. Calculated electronic structures of the conduction

band-edge states show the Γ- to X-valley transition as gallium composition increases and help decipher the direct-to-indirect band gap transition in the confined system. Finally, we show that $In_{1-x}Ga_xP$/ZnS nanocrystals display better thermal stability relative to InP/ZnS nanocrystals, likely due to a smaller mismatch of the lattice constants between the $In_{1-x}Ga_xP$ core and ZnS shell. Together, our results provide insight into the nature of the composition-driven direct-to-indirect transition of a model semiconductor system, providing crucial insight for designing next-generation colloidal QD materials.

3.2. Synthesis of $In_{1-x}Ga_xP$ cores and $In_{1-x}Ga_xP$/ZnS core-shell nanocrystals.

An In-to-Ga cation exchange reaction performed on indium pnictide nanocrystals dispersed in molten salts offers a viable route toward synthesizing the otherwise elusive gallium-containing ternary III-V phases.[36, 38] We exchange the native long-chain surfactants on the as-synthesized nanocrystals with compact charged inorganic ligands in order to disperse them in molten salt media. Z-type gallium halide ligands constitute a unique candidate for this role, as they avoid introducing additional heteroatom impurities such as chalcogenides.[37-38] Gallium is notoriously oxophilic at elevated temperatures, necessitating that oxygen-containing moieties are avoided at all subsequent steps. We, therefore, introduce an amine-based recovery in this report, allowing us to obtain a colloidal solution of alloyed ternary $In_{1-x}Ga_xP$ nanocrystals without using carboxylate ligands. This further prevents surface oxidation in the subsequent high-temperature ZnS shelling step.

To establish a general applicability of our protocol, we focus on three kinds of colloidal InP nanocrystals with different sizes and surface terminations. TOP/TOPO passivated InP nanocrystals were prepared by a dehalosilylation reaction between $InCl_3$ and tris(trimethylsilyl)phosphine

following an established synthesis pioneered by Micic *et al.*[31, 39] A population with an average diameter of ~4.9 nm was size-selectively separated from the reaction mixture.

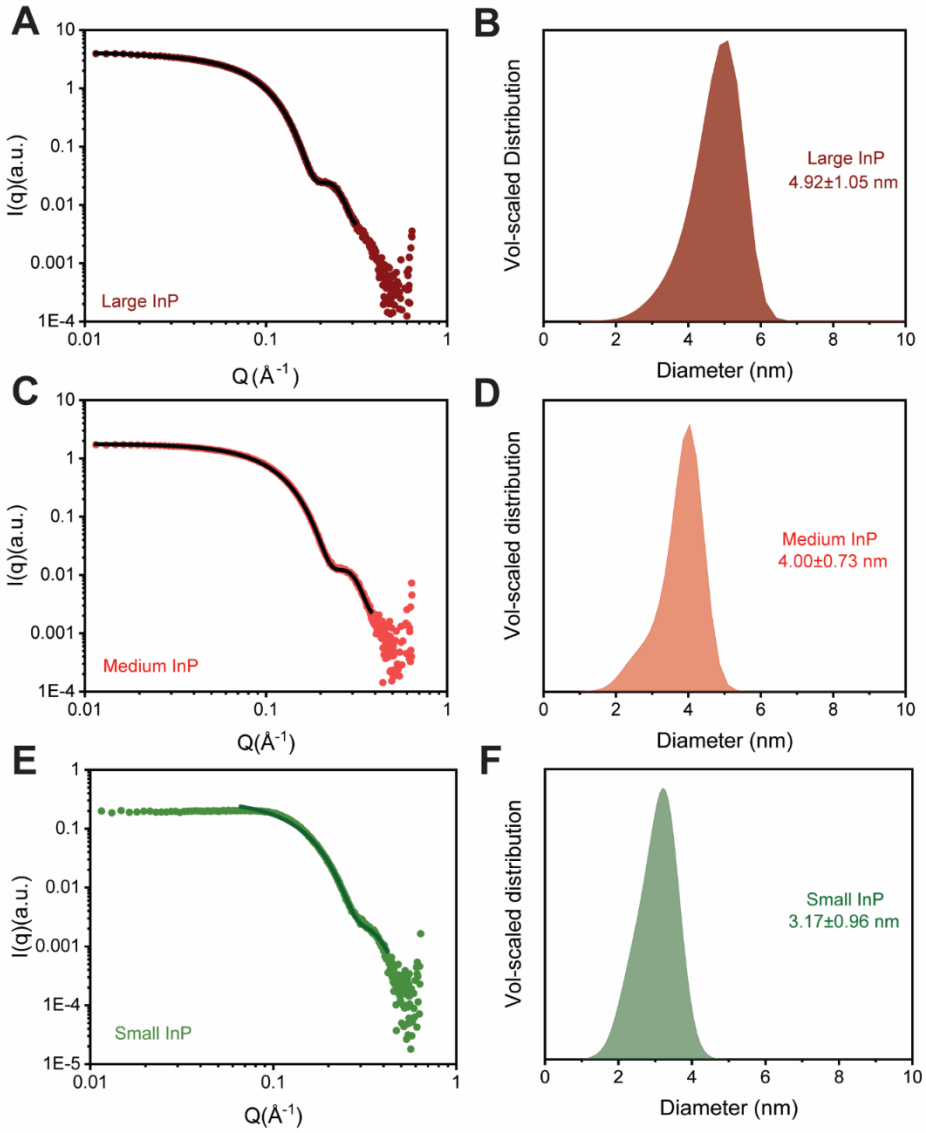

Figure 3.2. Size analysis: small-angle X-ray scattering (SAXS).
SAXS data and maximum-entropy fits for (A) size-selected large InP QDs, (C) medium-sized InP QDs and (E) small InP QDs. (B), (D) and (F) respectively are volume-scaled size distributions of the same obtained from a maximum-entropy fit to the SAXS data.

We also synthesized small InP nanocrystals of ~3.2 nm diameter via an adaptation of the indium myristate-based recipe pioneered by the Peng group.[26] A third intermediate-sized InP population

of 4.0 nm diameter, which is similar to QD cores used for display applications, were obtained from a proprietary source. The size distributions were calculated from maximum-entropy fits to the corresponding small angle X-ray scattering (SAXS) patterns, Figure 3.2A-F.[40] Following previous reports, the native organic ligands on each of these populations were exchanged for inorganic Z-type GaI_3 ligands.[37-38] We observe only small differences between the absorption spectra recorded using stable colloidal dispersions of these inorganically capped particles before and after ligand exchange (Figure 3.3), which we ascribe to subtle changes in energy levels of the band structure, influenced by changes in the QD surface chemistry.[41]

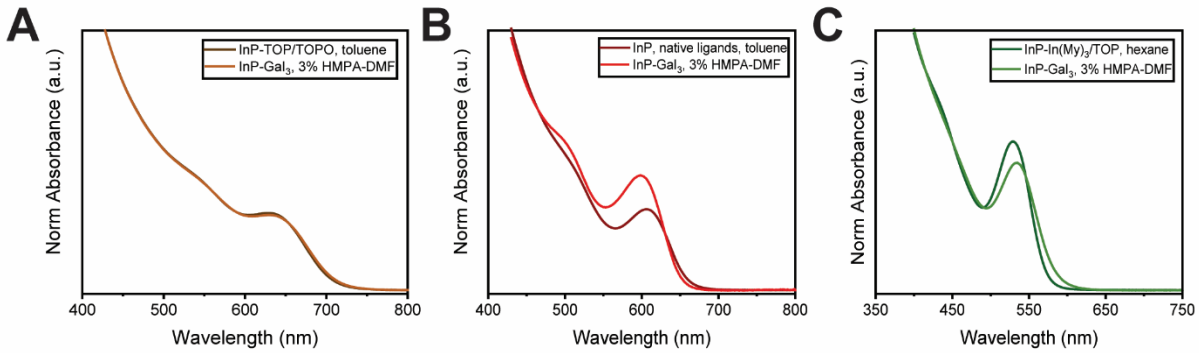

Figure 3.3. Optical characterization after gallium halide ligand exchange.
Comparison of optical absorption spectra of colloidal solutions of the relevant InP populations before and after GaI_3 ligand exchange: **(A)** 4.9 nm InP, **(B)** 4 nm InP and **(C)** 3.2 nm InP.

The InP particles capped with GaI_3 ligands were added to a $KGaI_4$ salt matrix (Figure 3.5A), flame-sealed inside quartz ampoules under vacuum, and subjected to different annealing conditions to yield similar gallium compositions, as noted in Table 3.1. Larger nanocrystals are more resistant to cation exchange than their smaller counterpart under similar reaction conditions, thereby requiring higher annealing temperatures for similar final gallium contents. Next, the salt matrix was dissolved using anhydrous acetonitrile, and the nanocrystals which are insoluble in acetonitrile

were recovered via centrifugation. We used a mixture of dodecylamine and octadecylamine as entropic ligands to confer colloidal stability to the $In_{1-x}Ga_xP$ nanocrystals in toluene.[42]

Table 3.1. Molten $KGaI_4$ salt cation exchange conditions with resultant gallium compositions and optical characterization plots of the corresponding core-shell samples.

Average diameter of the initial InP QDs	Annealing temperature (^oC)	Annealing duration (hr)	Estimated Ga content from PXRD x : $In_{1-x}Ga_xP$	Lattice Mismatch with ZnS	Corresponding panel in Fig. 3.7	
					Excitation -emission matrix	Time-resolved PL decay
4.92 nm	440	1	0.38	5.5%	A	B
4.00 nm	420	1	0.35	5.8%	C	D
3.17 nm	320/350	1+1	0.34	5.8%	E	F

Excess amine ligands were removed by precipitating the particles using methyl acetate and redispersing them in a desired non-polar solvent. We performed X-ray diffraction studies on the cation-exchanged products recovered with the aforementioned alkylamine ligands to ensure there was no decomposition of the zinc blende phase (Figure 3.4). We estimated lattice constants from the recorded diffraction patterns using Le Bail refinement, which allowed us to assign a resultant gallium composition to the alloyed $In_{1-x}Ga_xP$ phases. Additional peaks appearing before the (111) peak (*i.e.,* at lower 2θ) are more pronounced in the smaller populations and likely stem from the ordering of organic capping ligands.[43]

To study the photophysics of $In_{1-x}Ga_xP$ as a function of composition, we passivate the surface to remove surface trap states. Since gallium has a high affinity towards oxygen at elevated

temperatures, exposure of the alloyed $In_{1-x}Ga_xP$ nanocrystals to oxygen-containing shelling precursors (*e.g.*, carboxylates) can potentially trigger surface oxidation during ZnS shell growth.

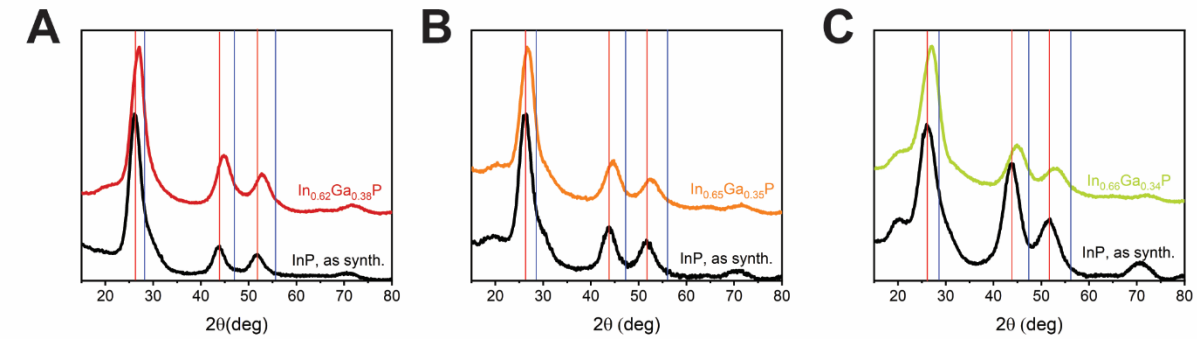

Figure 3.4. Diffraction patterns to estimate gallium composition in different InP populations. $In_{1-x}Ga_xP$ samples synthesized in a molten $KGaI_4$ salt matrix starting from (A) large 4.92 nm InP (B) medium 4.00 nm InP and (C) small 3.17 nm InP. Additional peaks appearing before (i.e., at lower 2θ) the (111) peak in (B) and (C), likely stem from the ordering of organic capping ligands.

Thus, we introduce a shelling protocol that allows us to grow a wide bandgap ZnS shell on the $In_{1-x}Ga_xP$ nanocrystals in a reducing environment (Figure 3.5A) without oxygen-containing precursors. $ZnCl_2$ in oleylamine and trioctylphosphine sulfide (TOP-S) were used as the zinc and sulfur precursors respectively. The In-to-Ga cation exchange decreases the lattice constant of the nanocrystals relative to the initial InP. This provides a better lattice match with wide-bandgap shelling materials such as ZnS, thus yielding highly emissive core-shell $In_{1-x}Ga_xP$/ZnS QDs. We obtain red, yellow, and green emission from the large-, medium-, and small-core populations respectively (Figure 3.5B), demonstrating the expected effects of quantum confinement to tune the bandgap of these alloyed nanocrystals as a function of size while retaining a similar composition at x~35% Ga content. Steady-state absorption and emission spectra of the individual core-shell samples are plotted in Figure 3.6, along with the absorption spectra of the relevant cores. $In_{0.65}Ga_{0.35}P$/ZnS nanocrystals synthesized from the 4 nm InP QDs have a 60 nm PL FWHM with a high PLQY of 75%, measured relative to the reference organic dye coumarin 153. Prior studies

indicated that emission in the ~530 nm region can be achieved with very small InP nanocrystals (~2 nm diameter) that are inherently less stable.[27]

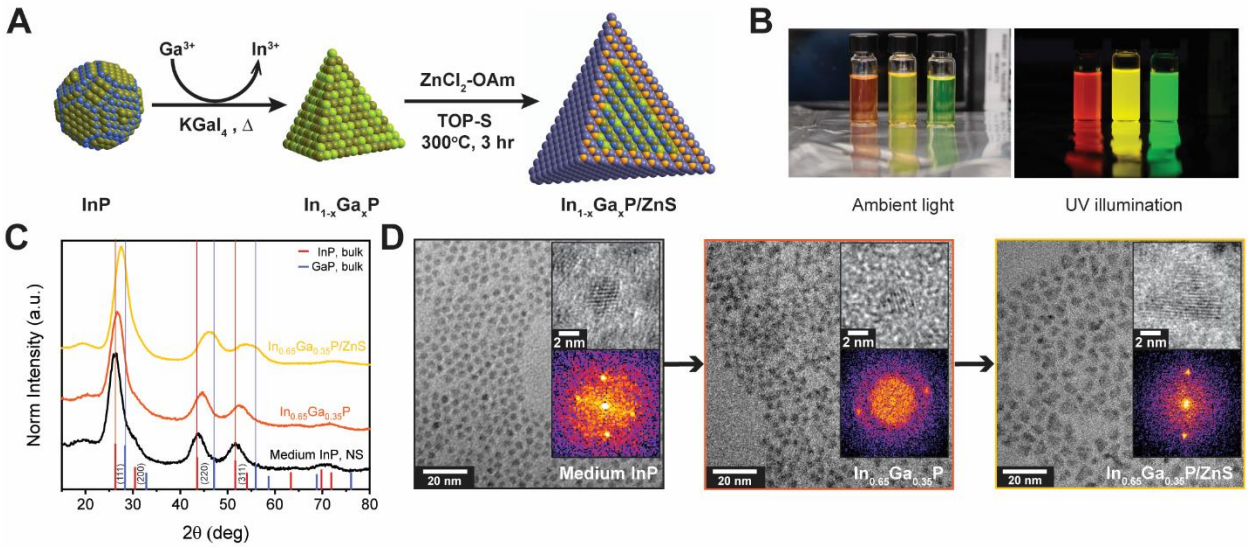

Figure 3.5. Core-shell synthetic scheme and structural characterization.
(A) Reaction scheme describing the conditions for the In-to-Ga cation exchange and the subsequent ZnS shelling steps. The photographs in (B) are of emissive core-shell $In_{1-x}Ga_xP/ZnS$ samples with similar gallium contents synthesized from 4.9 nm InP (red emitting post cation exchange), 4.0 nm InP (yellow) and 3.2 nm InP (green) populations. (C) Representative powder XRD patterns indicate a zinc blende crystal structure for the cores as well as for the core-shell samples derived from the 4.0 nm InP particles. (D) TEM images indicate the evolution of particle morphology over the cation exchange and shelling steps.

Notably, we could achieve green emission with a relatively high PLQY of ~48% using $In_{0.66}Ga_{0.34}P/ZnS$ QDs derived from the 3.2 nm InP population without any additional optimization. For larger 4.9 nm diameter $In_{0.62}Ga_{0.38}P/ZnS$ QDs, we achieved a PLQY of ~19%. We have previously shown that particles derived from this method have a higher density of internal defects,[38] indicating that starting with highly crystalline InP particles is likely key to achieving good quality $In_{1-x}Ga_xP$ emitters. Seeking to compare the contribution of population dispersity towards emission broadening in these samples, we constructed excitation-emission maps (Figure

3.7A, C, E) and found that a broad emission is inherent for the large particles, perhaps resulting from their higher defect concentration.

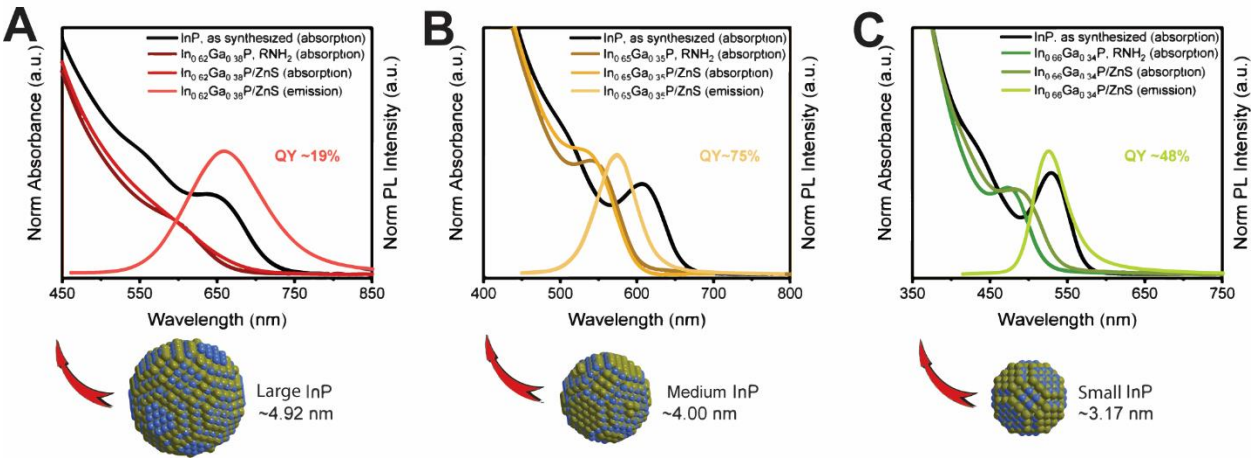

Figure 3.6. Steady-state optical spectra of $In_{1-x}Ga_xP/ZnS$ samples with similar gallium composition but different sizes.
Synthesized from (A) 4.9 nm large InP (red emitting post cation exchange), (B) 4.0 nm medium InP (yellow) and (C) 3.2 nm small InP (green) populations.

The impressive emission properties of the $In_{1-x}Ga_xP/ZnS$ samples reported in this study suggest that the ZnS shell we have grown provides efficient surface passivation, even though the lattice mismatch of $In_{0.65}Ga_{0.35}P$ with the ZnS shell is ~5.5%. In the 4 nm population, this is evidenced by the diffraction peaks getting narrower and further shifting to higher 2θ values after shelling (Figure 3.5C). Transmission Electron Microscopy (TEM) images indicate that the In-to-Ga cation exchange reaction in a molten gallium halide environment leads to increased faceting of the nanocrystals (Figure 3.5D), consistent with our previous observations.[38] We estimate that two monolayers of ZnS are grown under present shelling conditions, resulting in an average tetrahedral edge length of 9 nm for the representative faceted $In_{0.65}Ga_{0.35}P/ZnS$ nanocrystals derived from 4 nm InP (Figure 3.5D). The reduced lattice mismatch may still be too large, leading to a somewhat irregular growth of the ZnS shell at our reaction temperatures. While this proves sufficient to

provide reasonably high quantum yields, pursuing lattice-matched heterostructures or graded alloy shells may enable the growth of thicker shells and more efficient surface passivation.

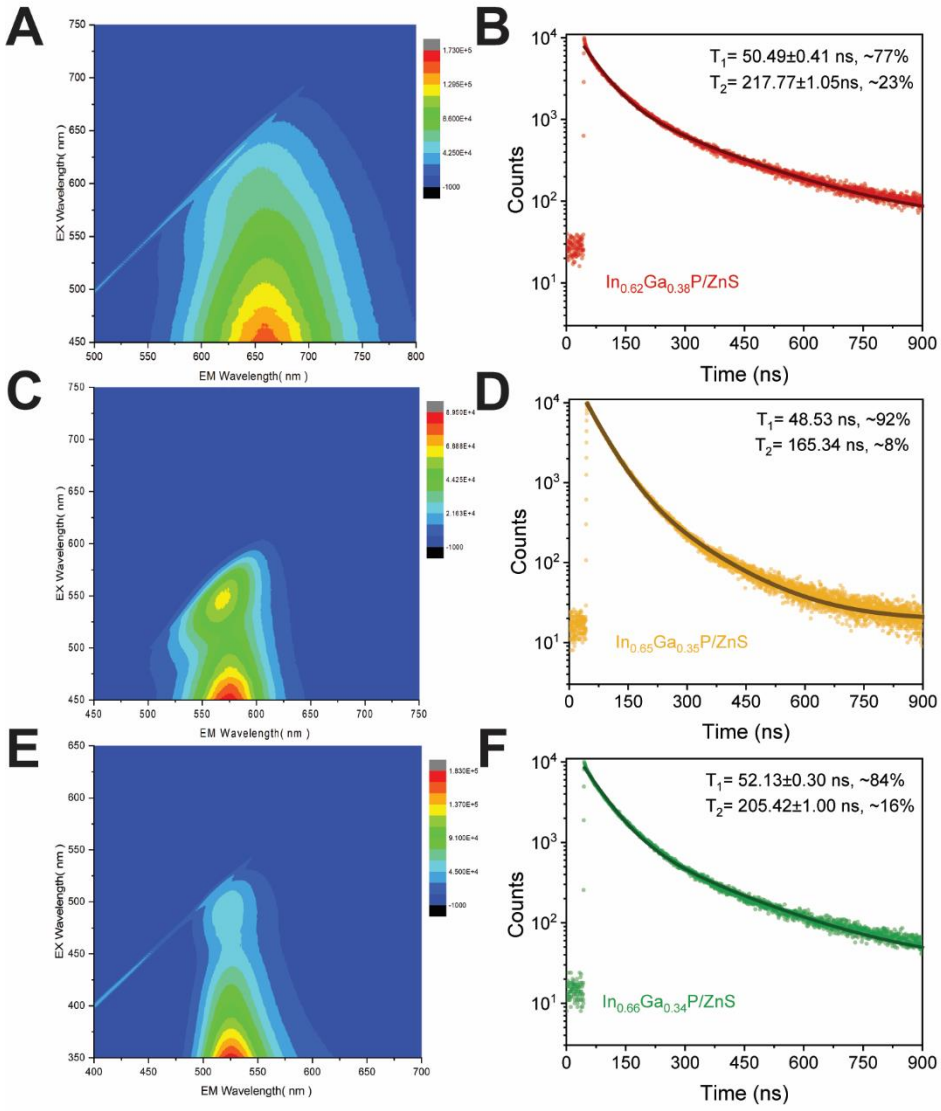

Figure 3.7. Excitation-emission matrices and time-resolved PL data of bright $In_{1-x}Ga_xP/ZnS$ core-shell samples synthesized from InP nanocrystals with different sizes.
(A) $In_{0.62}Ga_{0.38}P/ZnS$ from large 4.92 nm InP QDs, (C) $In_{0.65}Ga_{0.35}P/ZnS$ from medium 4.00 nm InP QDs and (E) $In_{0.66}Ga_{0.34}P/ZnS$ from small 3.17 nm InP QDs. Recording time-resolved PL and fitting the profile to a biexponential decay allow us to estimate the lifetime of excitonic decay in the same samples (B), (D) and (F), respectively. The molten salt annealing conditions and resultant gallium contents are matched with the optical characterization panels in table 3.1.

We collaborated with **Dr. Yunhua Chen and Prof. Aaron Rossini** at Iowa State University and performed solid-state nuclear magnetic resonance (ssNMR) experiments. The results show that the $In_{1-x}Ga_xP$ nanocrystals we prepared via molten salt processing are largely devoid of surface oxidation; the extent of oxidation of the phosphide phase is overall negligible. Further, the Ga distribution is likely homogeneous across the breadth of the nanocrystals. While ssNMR data cannot rule out some local inhomogeneities in Ga-to-In ratio, it can be concluded that $In_{0.50}Ga_{0.50}P$ QDs adopt an alloyed ternary III-V phase rather than a heterostructured morphology composed of InP and GaP domains.

3.3. Evolution of optoelectronic properties with Ga composition.

Equipped with an oxygen-free shelling protocol that yields good-quality emissive samples, we next seek to understand how the optoelectronic properties of these core-shell samples evolve as a function of gallium composition. Starting with the 4 nm InP nanocrystals, we synthesized a series of alloyed $In_{1-x}Ga_xP$ nanocrystals by performing In-to-Ga cation exchange in a $KGaI_4$ molten salt reaction medium under different combinations of annealing temperature and duration, as summarized in Table 3.2. The amine-capped $In_{1-x}Ga_xP$ nanocrystals were recovered as a colloidal solution in toluene, and characterized *via* X-ray diffraction; subsequently, the gallium compositions were estimated to be between 14% to 60% (Figure 3.8A). We performed elemental analysis using X-ray fluorescence (XRF) on the $In_{1-x}Ga_xP$/ZnS core-shell samples, the results are included in Table 3.2. For each sample, the elemental analysis method estimates the gallium content at ~25% higher than that estimated by employing XRD measurement of the lattice constant and subsequent Vegard's law interpolation of the gallium content. We have previously observed a similar discrepancy in gallium composition reported by elemental analysis techniques (XRF or ICP) and PXRD for small nanocrystals with a large surface-to-volume ratio.[37]

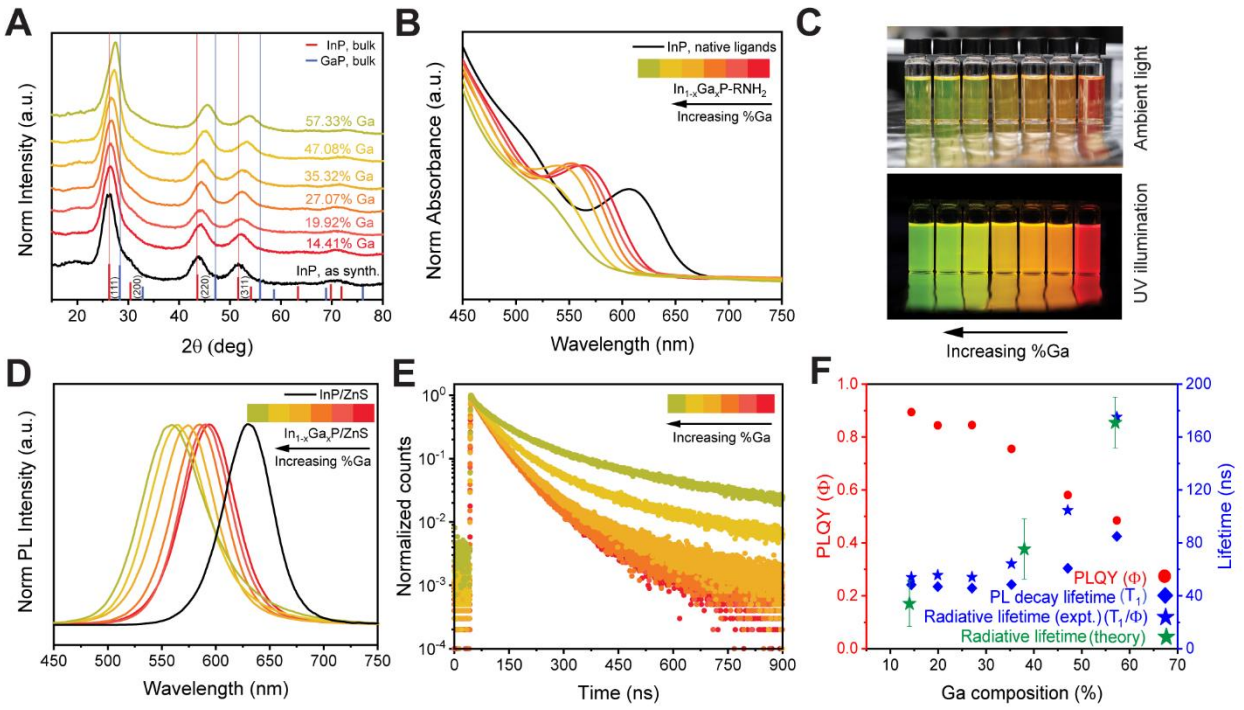

Figure 3.8. Optical and structural characterization of $In_{1-x}Ga_xP$ core and $In_{1-x}Ga_xP$/ZnS core-shells derived from 4 nm InP nanocrystals.
(A) Powder X-ray diffraction patterns and (B) Absorption spectra of the alloyed $In_{1-x}Ga_xP$ cores (normalized at 400nm). (C) Photographs show the large range of emission colors produced by core-shell $In_{1-x}Ga_xP$/ZnS samples with varying gallium content derived from the same 4.0 nm InP nanocrystals. (Red emission is from the InP/ZnS sample corresponding to x=0). (D) The corresponding emission spectra. (E) Time-resolved PL dynamics integrated over the emission spectra of the same samples indicate an increasing decay lifetime with gallium content. (F) The trends in PLQY decay time-constants pertaining to the predominant excitonic decay event and the corresponding radiative lifetime. The calculated radiative lifetimes for $In_{1-x}Ga_xP$ QDs of random gallium distributions are shown to agree well with the experimental results. The trace colors in panels B, D and E are the same as in panel A.

The 4 nm diameter QDs used in this study have approximately 25% of their atoms at the surface. Thus, one can imagine that changes in the composition of the outer surface layer can dramatically change the QD composition with only a minor impact on the QD interior. For example, if a surface monolayer of metal-rich InP exchanges to GaP, the elemental composition could be up to 25% gallium, while the XRD pattern would show only minor changes resulting primarily from the surface strain rather than bulk lattice reorganization. As expected, absorption peaks shift

monotonically to higher energies with increasing gallium content, indicative of a widening bandgap. Notably, we observe a continuous decline in the sharpness of the excitonic feature with increasing gallium content (Figure 3.8B). We can attribute this observation either to the broadening of nanocrystal size distribution over the course of high temperature annealing or to the mixing of excitonic states from direct and indirect valleys in the conduction band. Photographs of the particles under UV illumination (Figure 3.8C) show that we can achieve bright emission in a wide range of colors between red and green by varying gallium composition between 0 to 58% for 4 nm diameter cores. The recorded PL spectra corroborate our visual observations: a blue shift of the emission peak accompanies the increasing gallium content (Figure 3.8D).

Table 3.2. Molten $KGaI_4$ salt cation exchange conditions with resultant gallium compositions and optical characterization plots of the corresponding core-shell samples.

Annealing temperature (^oC)	Annealing duration (hr)	Estimated Ga content from PXRD x : $In_{1-x}Ga_xP$	Estimated Ga content from XRF / Elemental Analysis x : $In_{1-x}Ga_xP$	Corresponding panel in Fig. 3.9		
				Relevant absorption and emission spectra	Excitation -emission map	Time-resolved PL decay
362	1	0.14	0.39	A	B	C
380	1	0.20	0.45	D	E	F
400	1	0.27	0.51	G	H	I
420	1	0.35	0.60	J	K	L
460	1	0.47	0.69	M	N	O
440	24	0.57	0.78	P	Q	R

To quantitatively rationalize experimentally observed optoelectronic properties of $In_{1-x}Ga_xP$ QDs, **Kailai Lin and Prof. Eran Rabani** calculated the electronic structure and optical

properties of alloyed $In_{1-x}Ga_xP$ QDs using atomistic semi-empirical pseudopotential methods[44-47] combined with the Bethe-Salpeter Equation (BSE).[48-49] To yield a unified description of inter-atomic interactions in the alloyed systems, single atomistic pseudopotentials each for In, Ga, P, and As were fitted to accurately reproduce the bulk band structures and bulk deformation potentials of relevant binary semiconductors (i.e., InP, GaP, InAs and GaAs).[46, 50] The pseudopotential has a local form in the reciprocal space, with a prefactor to account for local strain effects. The alloyed $In_{1-x}Ga_xP$ QD configurations were constructed by randomly replacing In cations in a regular tetrahedral InP QD with Ga cations. The QD structures were then relaxed using a previously parameterized Tersoff-type force field[51] and passivated with pseudo-ligand potentials. Given the relaxed QD geometry, the single particle Hamiltonian was constructed with the fitted atomistic pseudopotentials and diagonalized using the stochastic filter diagonalization technique to obtain quasiparticle states of the QD near the HOMO and LUMO energies.[47] The Bethe-Salpeter equation was solved within the static screening approximation to obtain correlated electron-hole pair (i.e., exciton) states.[49] Our theoretical approach allows for joint investigations and direct comparisons between theory predictions and experimental measurements as it permits accurate atomistic calculations of the optoelectronic properties for $In_{1-x}Ga_xP$ nanocrystals with arbitrary gallium composition with experimentally relevant sizes.

Electronic structure calculations confirm the experimentally observed peak shifts. As shown in Figure 3.1B, the calculated optical gaps for $In_{1-x}Ga_xP$ QDs show a monotonic increase in energy with higher gallium concentration and a similar dependence on the average lattice constant as compared to the bulk alloyed $In_{1-x}Ga_xP$. The slope of the QD optical gap changes at 65% gallium composition, indicating an equivalent transition between direct and indirect gap regimes as in the bulk alloy $In_{1-x}Ga_xP$ (blue line). And the shift of the transition point from 75% in

the bulk to 65% for 4nm QDs can be explained by the quantum confinement and the much smaller electron effective mass in the Γ valley as compared to the effective mass in the X and L valleys. The vertical shift of optical gap between the QDs and bulk ternary alloys is attributed to the confinement energy of QD systems. In addition, spatially inhomogeneous In-to-Ga cation exchange is studied through theoretical calculations. The results are consistent with our ssNMR studies, suggesting that Ga is homogeneously distributed in the particle.

We carried out steady-state spectroscopy on each sample, and a few representative experimental absorption and emission spectra from these measurements are plotted in Figures 3.8B, D and 3.9 for samples in the x-0-58% range. $In_{0.86}Ga_{0.14}P$/ZnS is the brightest sample among the alloyed populations, registering a quantum yield of 89% along with good color purity (57 nm FWHM of the emission peak). For the 4nm nanocrystals studied so far, it is difficult to incorporate large amounts of gallium (x>58%) due to decomposition. However, we analyzed all possible gallium compositions computationally for 4nm diameter $In_{1-x}Ga_xP$ nanocrystals by calculating the absorption spectra of InP QD, GaP QD, and alloyed $In_{1-x}Ga_xP$ QDs ranging from 14% to 92% gallium content using the atomistic pseudopotential methods, as shown in Figures 3.10A-H. To generate the absorption spectra, the oscillator strength $f = \frac{4m_e E}{3\hbar^2 e^2}|\boldsymbol{\mu}|^2$ (where $\boldsymbol{\mu}$ is the transition dipole moment and E is the exciton energy) for each excitonic state (grey lower lines) is calculated and its magnitude represented by the height of the upper black lines in Figures 3.10A-H. For all of the samples with gallium content below 57%, the majority of the low energy states in the DOS have large oscillator strength, consistent with the strong excitonic emission observed for each excitonic transition[52] (upper black lines).

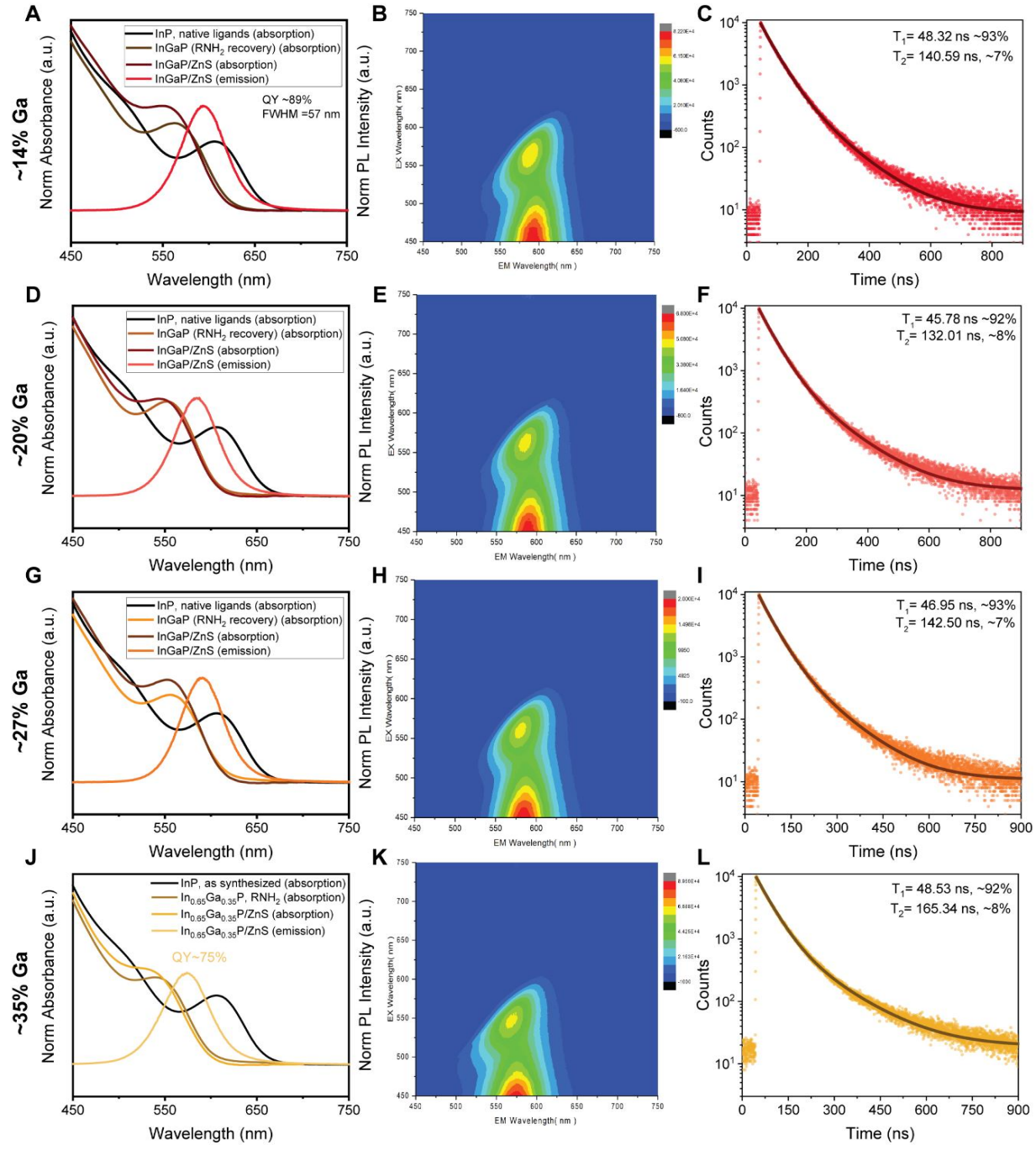

Figure 3.9. Steady-state optical characterization and time-resolved PL decay profiles of core-shell $In_{1-x}Ga_xP/ZnS$ samples synthesized from the 4.0 nm InP QDs.
The molten salt annealing conditions and resultant gallium contents are matched to the optical characterization panels in Table 3.2.

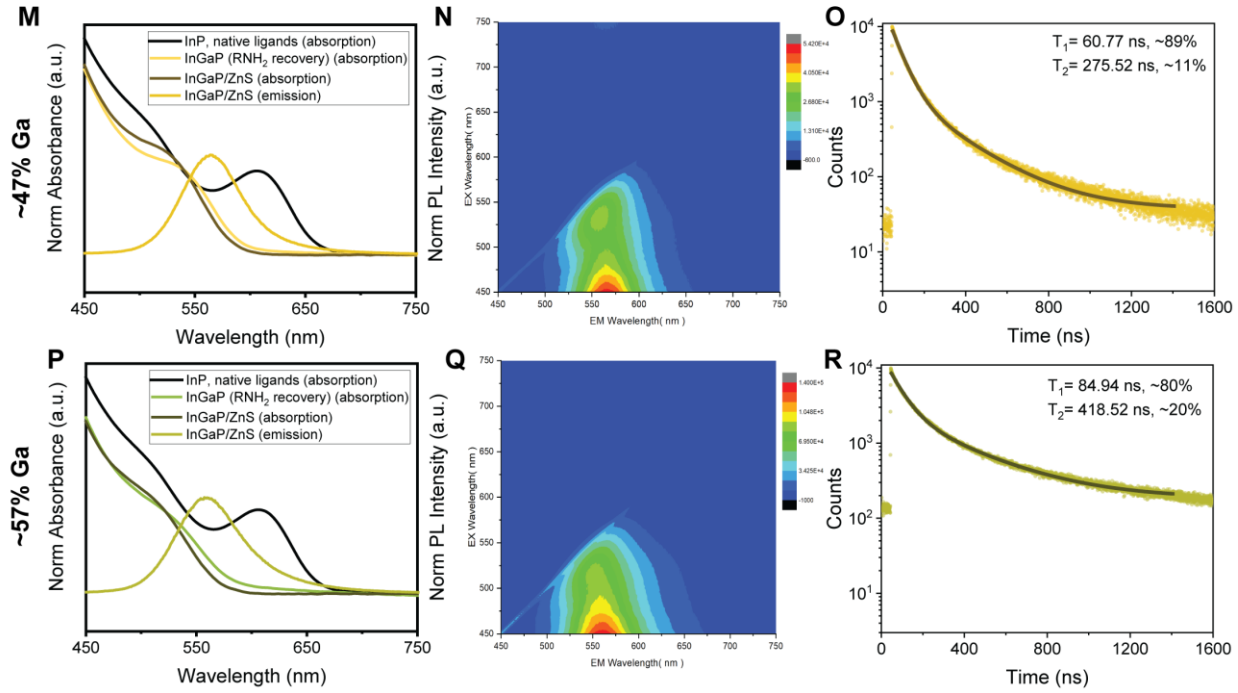

Figure 3.9 (continued). Steady-state optical characterization and time-resolved PL decay profiles of core-shell $In_{1-x}Ga_xP/ZnS$ samples with synthesized from the 4.0 nm InP QDs.
The molten salt annealing conditions and resultant gallium contents are matched to the optical characterization panels in Table 3.2.

For $In_{1-x}Ga_xP$ QDs with x>57%, the computation results show a continued decrease in the sharpness of the absorption onset as the gallium content increases (Figures 3.10E-H). The decrease in the magnitude of the absorption onset is a result of the decrease in oscillator strength of the lowest energy excitonic transitions, consistent with indirect-like electronic transitions. This shows that extensive gallium exchange creates many low energy "dim" excitonic states at the band edge, which is indicative of optical transitions with more "indirect" character.

Calculated absorption spectra are consistent with the experimental observation that the sharpness of the excitonic features declines as gallium content increases. Importantly the theoretical observations are not convoluted with other sources of broadening such as size distribution or composition distributions. Although ssNMR studies establish that the In and Ga

atoms are randomly distributed at the cation sites of the ternary III-V lattice, particle-to-particle compositional variation remains a possible source of added heterogeneity in alloyed nanocrystals. We have previously established that ensemble diffraction techniques are insensitive to these subtle structural differences,[38] but the emissive core-shell $In_{1-x}Ga_xP$/ZnS nanocrystals allow us to explore this optically. Recording PL excitation (PLE) spectra allows us to selectively look at the spectral features of a smaller sub-population instead of the entire ensemble. We, therefore, seek to compare the spectral heterogeneity of these alloyed nanocrystals using the corresponding absorption and PLE linewidths for excitonic transitions. To this end, we constructed excitation-emission maps (Figure S3.9), allowing us to extract representative PLE spectra at the corresponding emission maxima, as well as at the point of half the maximum emission intensity on the high-energy flank (Figure 3.10I). We can further quantify the PLE and ensemble absorption linewidths using the full width at half-maximum (FWHM) of Gaussian fits to the low energy flanks of the respective peaks. Figure 3.10J explains this analytic scheme for a representative sample $In_{0.86}Ga_{0.14}P$/ZnS; the results for these $In_{1-x}Ga_xP$/ZnS samples are summarized in Figure 3.10K. It is evident that each individual PLE spectrum becomes broader at higher gallium concentrations. Ensemble broadening from population ripening at elevated temperatures alone cannot explain the broadening of excitonic features in individual PLE spectra. Previous computational and experimental works have established that the energy states of homogeneously alloyed nanocrystals are not simple arithmetic means of their individual components.[53-54] Instead, atomic disorder-related symmetry breaking can lead to the formation of additional mixed states, resulting in broadened spectral features during excitonic transitions, consistent with our observations. Furthermore, the theoretical model in this work incorporates the atomistic details and local strain effects through atomistic pseudopotentials, and thus, the "mixing of excitonic states" of the alloyed system is directly captured by our

electronic structure calculations and can be observed from the density of states in Figures 3.10A-H. Sample inhomogeneity is accounted for in the calculated absorption spectra through the energy-dependent Gaussian broadening and is kept the same across different Ga compositions. Therefore, the theoretical calculations in this work help conclude that exciton state mixing due to symmetry breaking is the main contributor to the broadened absorption features in $In_{1-x}Ga_xP$ QDs with higher Ga composition. We probe this in more detail with transient absorption studies, the results are summarized in a later section.

We estimate the PL decay lifetimes from time-resolved PL studies (Figure 3.8E). Time-resolved photoluminescence (TRPL) of the $In_{1-x}Ga_xP$/ZnS samples with varying size and Ga-to-In ratios does not show any fast early time (sub-nanosecond) decay components usually associated with non-radiative recombination channels, which is typical for samples with high PL quantum yield. The faster radiative decay channel is the major contributor in each of these high-quality core-shell samples from a subsequent biexponential fit to the decay profile, shown in Figures 3.7 and 3.9. A comparison of the TRPL decay profiles of these $In_{1-x}Ga_xP$/ZnS samples in Figure 3.8E illustrates a remarkable trend: the PL decay lifetime increases monotonically while the PLQY decreases with increasing gallium content, which is difficult to explain by a trapping mechanism. We estimate the radiative lifetime by combining the PL 1/*e* decay time constant and PLQY, providing us with an insight into the materials' intrinsic radiative lifetime (Figure 3.8F). Importantly by directly measuring the radiative lifetimes, the trends we observe are independent of the quality of surface passivation during synthesis or other defects which can lead to non-radiative recombination.

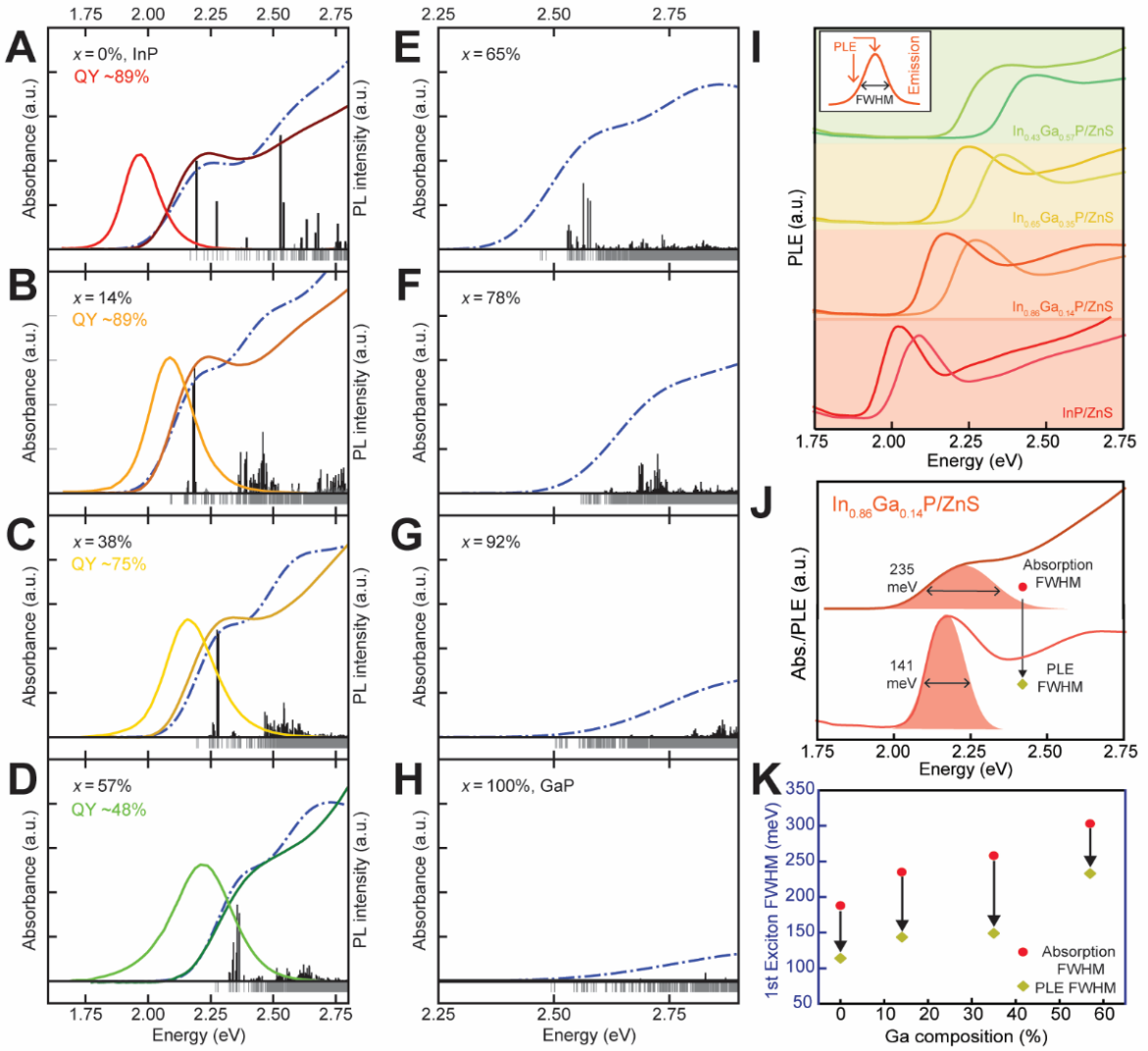

Figure 3.10. Absorption, emission, and excitation spectra with calculated density of states and oscillator strengths.

(A-H) Experimental absorption, emission spectra (solid-colored lines) and calculated absorption spectra (blue dash-dot curves) of representative core-shell $In_{1-x}Ga_xP/ZnS$ samples with 0-57% Ga content, synthesized from 4 nm InP QDs. The exciton density of states and oscillator strengths from theoretical predictions are plotted as grey sticks below the x-axis and black sticks above the x-axis respectively. (I) PLE spectra of the same samples collected at the corresponding emission maxima as well as at half the maximum emission intensity on the high-energy flank. The inset plot describes the same schematically. (J) Comparison of linewidths of the first excitonic feature on the ensemble absorption spectrum and PLE spectrum of the representative $In_{0.86}Ga_{0.14}P/ZnS$ sample, collected at the emission maximum. The linewidths are estimated as the FWHM of Gaussian fits (shaded) to the low energy flanks of the respective peaks. (K) Summary and comparison of absorption and PLE linewidths extracted for the representative core-shell $In_{1-x}Ga_xP/ZnS$ samples noted in A-D.

Radiative lifetimes at room temperature are calculated from the exciton energy and transition dipole moment for the calculated exciton states according to equation: $\tau_r = \frac{3\pi\varepsilon_0\hbar c^3}{\omega^3 |\boldsymbol{\mu}|^2}$, where c is the speed of light, and $\hbar\omega$ is the exciton energy. For the same gallium percentage, multiple configurations with random gallium distributions are considered, rendering the mean and standard deviation of the radiative lifetimes. As summarized in Figure 3.8F, the trends are quite evident. An addition of up to ~30% Ga into the $In_{1-x}Ga_xP$ cores has only a minor effect on radiative lifetime and quantum yield, while a further increase of Ga content up to 60% is accompanied by a decline in PLQY down to 48%, along with a more than threefold increase in radiative lifetime, from 54 ns to 175 ns. The rate of radiative decay is inversely proportional to the calculated radiative lifetime, so we conclude that the oscillator strength of excitonic recombination[55] in these systems is independent of composition when Ga content is below 35% and gradually decreases with increasing gallium content above 35%. Theoretical calculations in this work show good agreement with experimental measurements and demonstrate the same trend of decreasing absolute absorption intensity (Figure 3.10A-H) and increased radiative lifetimes (Figure 3.8F) as Ga concentration increases in alloyed $In_{1-x}Ga_xP_{1-x}$ QDs of the same size. A direct-gap-like excitonic transition characterized by a large oscillator strength would be from the Γ valley of the conduction band to the Γ valley of the valence band. In bulk crystals, the oscillator strength for the transitions from X or L valleys into Γ valley is significantly lower. We ascribe the diminishing oscillator strength of excitonic recombination in Ga-rich $In_{1-x}Ga_xP$/ZnS QDs to an increased mixing of electron states originating from the X and Γ valleys. In bulk $In_{1-x}Ga_xP$ crystals, the direct to indirect

transition is observed at x~0.75 gallium content (Figure 3.1), thus motivating an exploration of quantum-confined samples with even higher gallium contents.

3.4. Trends at higher Ga content.

Our studies suggest that the larger InP nanocrystals are more resistant towards decomposition under similar reaction conditions as compared to smaller nanocrystals, although higher temperatures and longer annealing times are required to achieve high gallium contents. We, therefore, focus on particles derived from the large 4.9 nm InP population to achieve higher gallium contents. Bright $In_{0.62}Ga_{0.38}P$/ZnS samples could be synthesized from 4.9 nm InP cores, as shown in Figure 3.6. We further prepared three populations of cation-exchanged $In_{1-x}Ga_xP$ cores in the 65-92% gallium content range; the reaction conditions are listed in Table 3.3.

Table 3.3. Molten $KGaI_4$ salt cation exchange conditions with the resultant gallium compositions for cation exchange performed on 4.9 nm InP.

Annealing temperature (^oC)	Annealing duration (hr)	Estimated Ga content from PXRD; x-value : $In_{1-x}Ga_xP$	PLQY
440	1	0.38	~19%
450	24	0.65	~2%
450	30	0.78	Non-emissive
450	48	0.92	Non-emissive

The nanocrystalline phases were characterized via PXRD, and gallium compositions were estimated from the diffraction patterns (Figure 3.11A). Representative TEM images provided in Figure 3.11B confirm that we have grown a widegap ZnS shell on the ternary alloyed nanocrystals. Steady-state optical characterization of the core-shell $In_{0.35}Ga_{0.65}P$/ZnS sample (Figure 3.12A) indicates that this sample is weakly emissive, with a PLQY of 2%. The corresponding excitation-emission map is provided in Figure 3.12B.

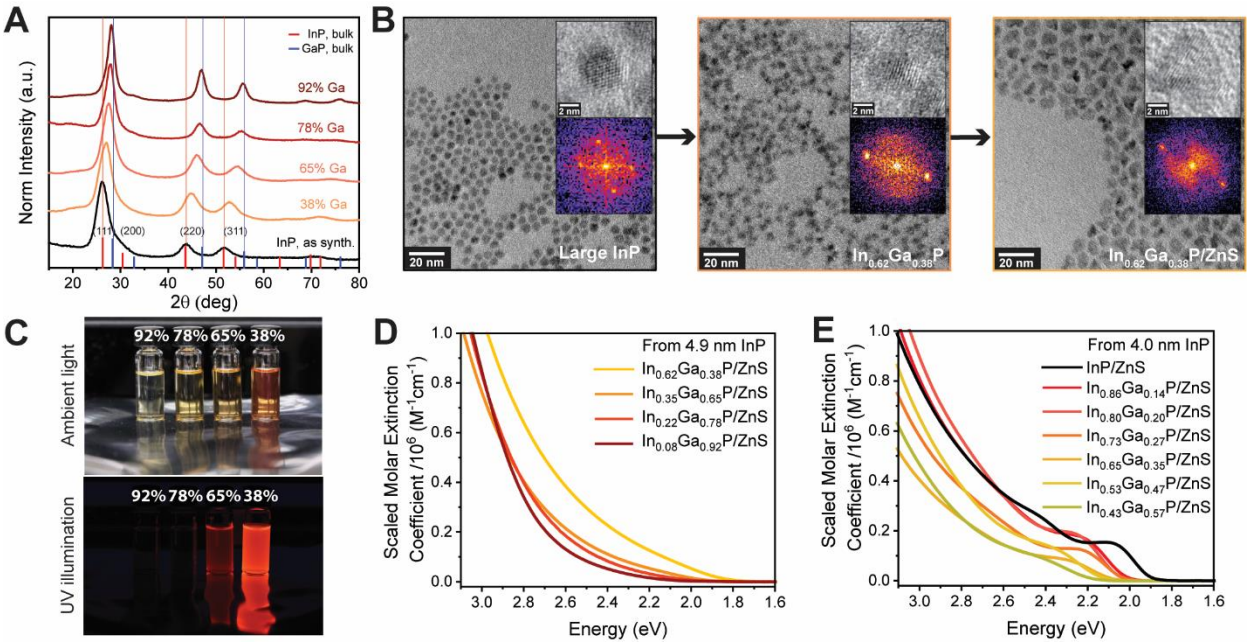

Figure 3.11. Optical and structural characterization of samples with higher Ga content.
(A) PXRD patterns of $In_{1-x}Ga_xP$ cores with high gallium content derived from the large 4.9 nm InP population. (B) Representative TEM images of the InP, $In_{0.62}Ga_{0.38}P$ and $In_{0.62}Ga_{0.38}P/ZnS$ samples indicate the evolution of particle morphology during cation exchange and ZnS shell growth. (C) Photographs of the relevant core-shell samples derived from the same 4.9 nm InP population in ambient light and under UV illumination. Absorbance plots were scaled to the measured absorption cross section at 400 nm (3.1 eV) to yield molar extinction coefficient plots of representative $In_{1-x}Ga_xP/ZnS$ samples synthesized from the (D) 4.9 nm InP population and (E) 4.0 nm InP population.

An excitonic feature is not resolved in the absorption spectra of samples with even higher gallium content, $In_{0.22}Ga_{0.78}P/ZnS$ and $In_{0.08}Ga_{0.92}P/ZnS$ (Figure 3.12C, E). Notably, these are also completely non-emissive, as the excitation-emission maps indicate (Figure 3.12D, F). Visual confirmation can be obtained from the photographs in Figure 3.11C. Using fluence-dependent transient absorption and a Poisson excitation model[7] (discussed in more detail in the next section), we determined the absorption cross-section and, subsequently, the molar extinction coefficient of each sample[56] at 400 nm (3.1 eV) (Figure 3.13). The corresponding absorption spectra were scaled to the extinction coefficients at 400 nm accordingly (Figure 3.11D). A similar treatment of the

absorption spectra of 4 nm core diameter $In_{1-x}Ga_xP$/ZnS samples is shown in Figure 3.11E. This demonstrates that samples with a higher gallium composition show a decrease in absolute absorbance of the excitonic feature. This is consistent with a weakened oscillator strength of excitonic transitions which was suggested by the increase in radiative lifetime. From this, we conclude that the optically dark $In_{0.22}Ga_{0.78}P$/ZnS and $In_{0.08}Ga_{0.92}P$/ZnS samples obtained from 4.9 nm InP are potentially behaving as indirect semiconductors, *i.e.*, the Γ and X valleys are the highest valence band and lowest conduction band positions, respectively. We further performed Tauc analysis to estimate the corresponding indirect gaps. A baseline correction for the disorder-induced Urbach tail was performed according to previously prescribed protocols,[57] thus allowing us to estimate the indirect gaps at 2.71 eV and 2.68 eV for Γ to X valley transitions in $In_{0.22}Ga_{0.78}P$/ZnS and $In_{0.08}Ga_{0.92}P$/ZnS respectively (Figure 3.14).

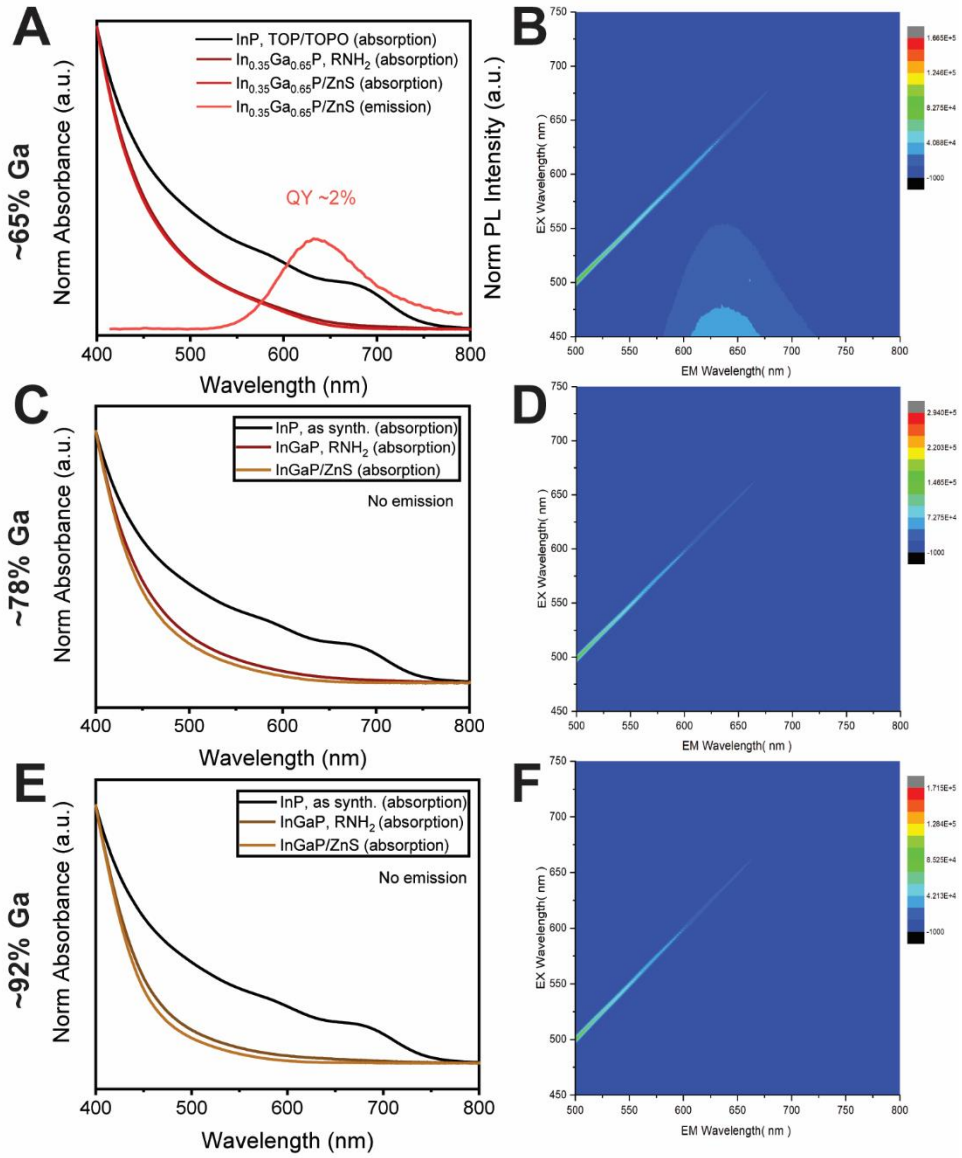

Figure 3.12. Optical characterization of the core-shell $In_{1-x}Ga_xP/ZnS$ samples with high Ga content derived from the 4.9 nm InP QDs.

Absorption and emission spectra of the core-shell $In_{0.35}Ga_{0.65}P/ZnS$ sample are provided in (A). The emission is weak, with a solution phase PLQY of ~2%; (B) the corresponding excitation-emission matrix. Samples with higher gallium content are completely non-emissive, as indicated in the associated excitation-emission matrices. (C) and (D) pertain to the core-shell $In_{0.22}Ga_{0.78}P/ZnS$ sample; (E) and (F) pertain to the $In_{0.08}Ga_{0.92}P/ZnS$ sample.

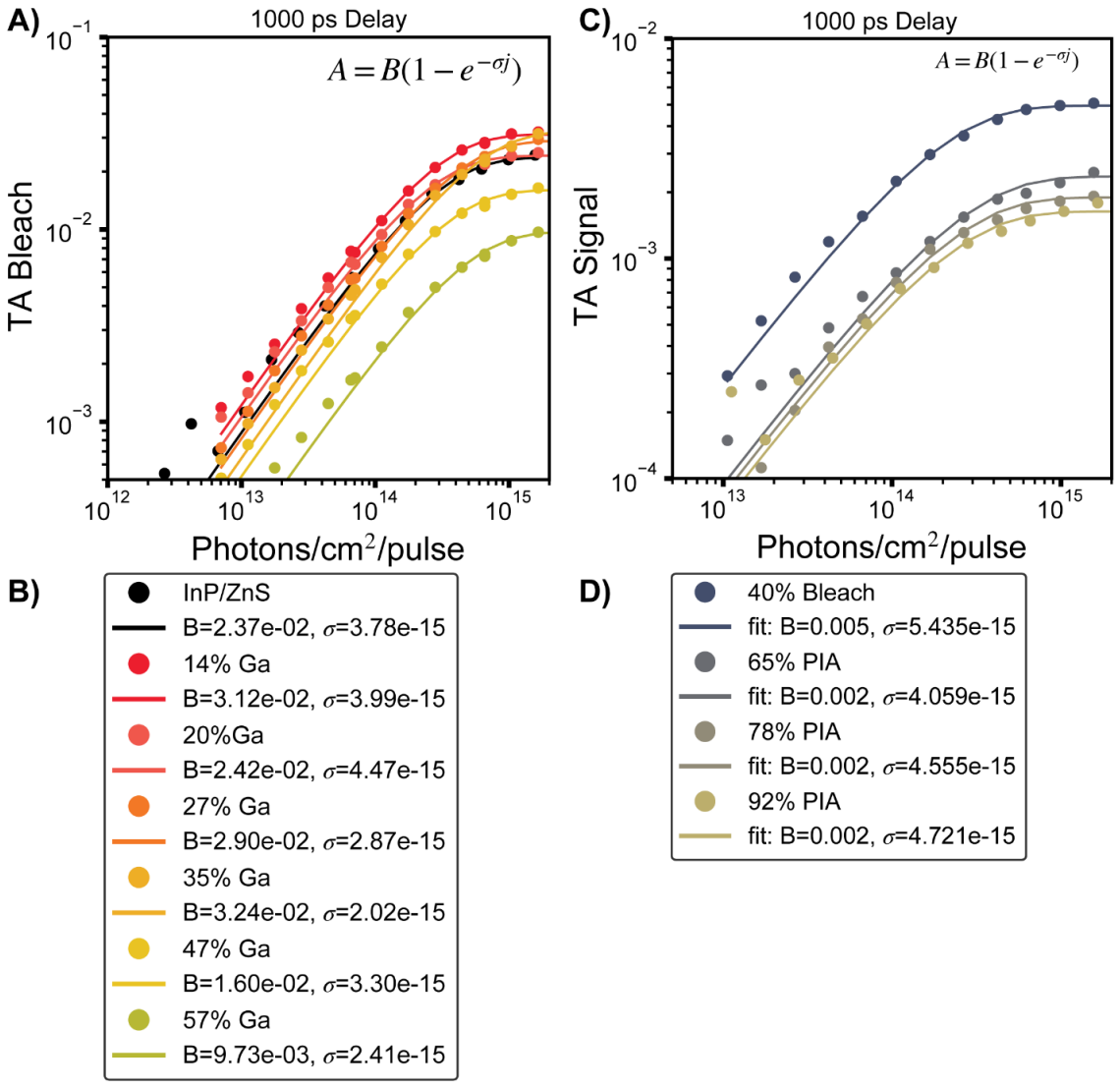

Figure 3.13. Determination of the absorption cross section for $In_{1-x}Ga_xP/ZnS$ nanocrystals.
(A) Fluence dependent TA bleach signal for 4 nm core $In_{1-x}Ga_xP/ZnS$ nanocrystals with fits to Poissonian single exciton statistics. From this we extract the bleach amplitude scaling factor and the absorption cross section at 400 nm. (B) These cross sections are used to determine the absolute absorbance at the band edge for the $In_{1-x}Ga_xP/ZnS$ nanocrystals shown in Figure 3.11E. (C) Fluence dependent TA signal for 4.9 nm core $In_{1-x}Ga_xP/ZnS$ (bleach for 40% Ga, PIA for 65-92% Ga) with fits to Poissonian single exciton statistics. From this we extract the bleach amplitude scaling factor and the absorption cross section at 400 nm. (D) These cross sections are used to determine the absolute absorbance at the band edge for the $In_{1-x}Ga_xP/ZnS$ nanocrystals shown in Figure 3.11D. We note that 400nm is below the absorption onset for the ZnS shell, so we are primarily measuring the absorption cross section of the III-V core.

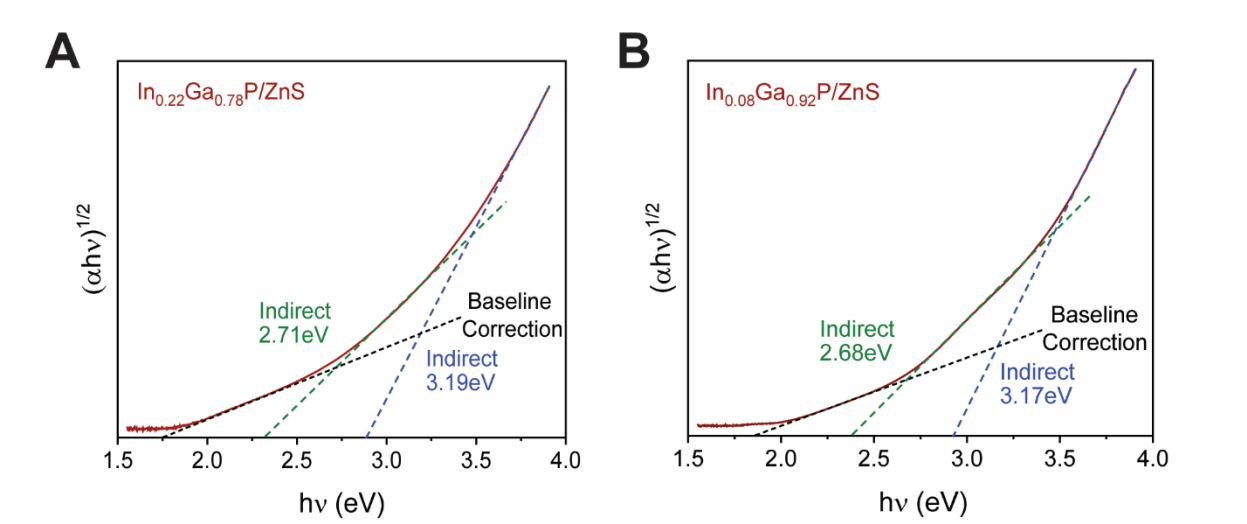

Figure 3.14. Tauc plots pertaining to an indirect band alignment.
Constructed from the absorbance values of the optically dark (A) $In_{0.22}Ga_{0.78}P/ZnS$ and (B) $In_{0.08}Ga_{0.92}P/ZnS$ samples.

3.5. Transient absorption (TA) spectroscopy.

This section is contributed by Dr. Justin Ondry and Prof. Richard Schaller and included here to ensure that the presented results are comprehensive.

We performed femtosecond transient absorption measurements on the $In_{1-x}Ga_xP/ZnS$ nanocrystals synthesized from 4.9 nm InP cores, which displayed absorption and PL characteristics of direct-gap-like behavior (38% Ga), intermediate behavior (65% Ga), and indirect-gap-like behavior (78% Ga), respectively. Measurements were performed using a 35-fs, 2-kHz Ti:sapphire laser with time-delayed white light probe pulses produced in a 2 mm sapphire plate and 1-kHz pump pulses centered at 400 nm produced from second harmonic generation of the fundamental. At these pump energies, we are exciting the samples well above the band gap of the $In_{1-x}Ga_xP$ core but below the absorption onset of the ZnS shell. All time-resolved absorption spectra were collected at room temperature from stirred solutions, first at low excitation fluence such that only single exciton dynamics were observed. TA data was collected on samples with ZnS shells, so the TA dynamics better reflected intrinsic carrier dynamics rather than charge trapping dynamics. The similarity

between the UV-vis absorption feature of unshelled and shelled samples indicates the presence of the shell has minimal impacts on the band edge absorption spectra of these materials, in agreement with a type-I band alignment between the core and the shell materials (Figure 3.9, 3.12). Figures 3.15A and B show schematic representations of the expected transient absorption signals for direct and indirect band gap materials. The key observation is that a direct gap semiconductor is expected to show both ground state bleach (GSB) signal and photoinduced absorption (PIA) signal whereas indirect gap materials are only expected to show a PIA signal. Figure 3.15C shows a transient absorption spectroscopy map for $In_{0.62}Ga_{0.38}P$/ZnS nanocrystals. We observe a strong ground state bleach signal (negative ΔA) peaked at 605 nm that develops within ~1 ps after the pump pulse and slowly decays over the nanosecond timescale of the measurement. The bleach signal corresponds well to the excitonic feature we observe by linear absorption of the sample (Figure 3.6A). This behavior is consistent with a typical direct band gap semiconductor nanocrystal where the $1S_e - 1S_h$ excitonic transition is bleached once the photoexcited carrier cools to the band edge. A linecut of the TA signal at the maximum bleach amplitude (Figure 3.15F) shows slow decay of the bleach signal, consistent with the timescales observed by TRPL. We also observe photo-induced absorption (PIA) signal at wavelengths to the red of the bleach feature, which results chiefly from electrons in the conduction band undergoing excitation to the near-continuum of states above the band edge by the probe pulse.

Next, we turn our attention to the $In_{0.22}Ga_{0.78}P$/ZnS sample, which showed a diffuse absorption onset and lacked detectable photoluminescence at room temperature or 77K. Transient absorption dynamics for the $In_{0.22}Ga_{0.78}P$/ZnS are shown in Figure 3.15E, H. Here we exclusively observe a PIA signal for all wavelengths and do not detect any trace of a bleach feature in the probed spectral range or timescale. This behavior is consistent with what is expected for indirect-gap materials,

where the photoexcited electron and hole reside in different valleys of the conduction and valence band; the momentum mismatch between the electron and hole prevents the formation of an optical bleach signature. The PIA signals measured at 750 nm and 561 nm both form within 1 ps and slowly decay over the 1 ns measurement window.

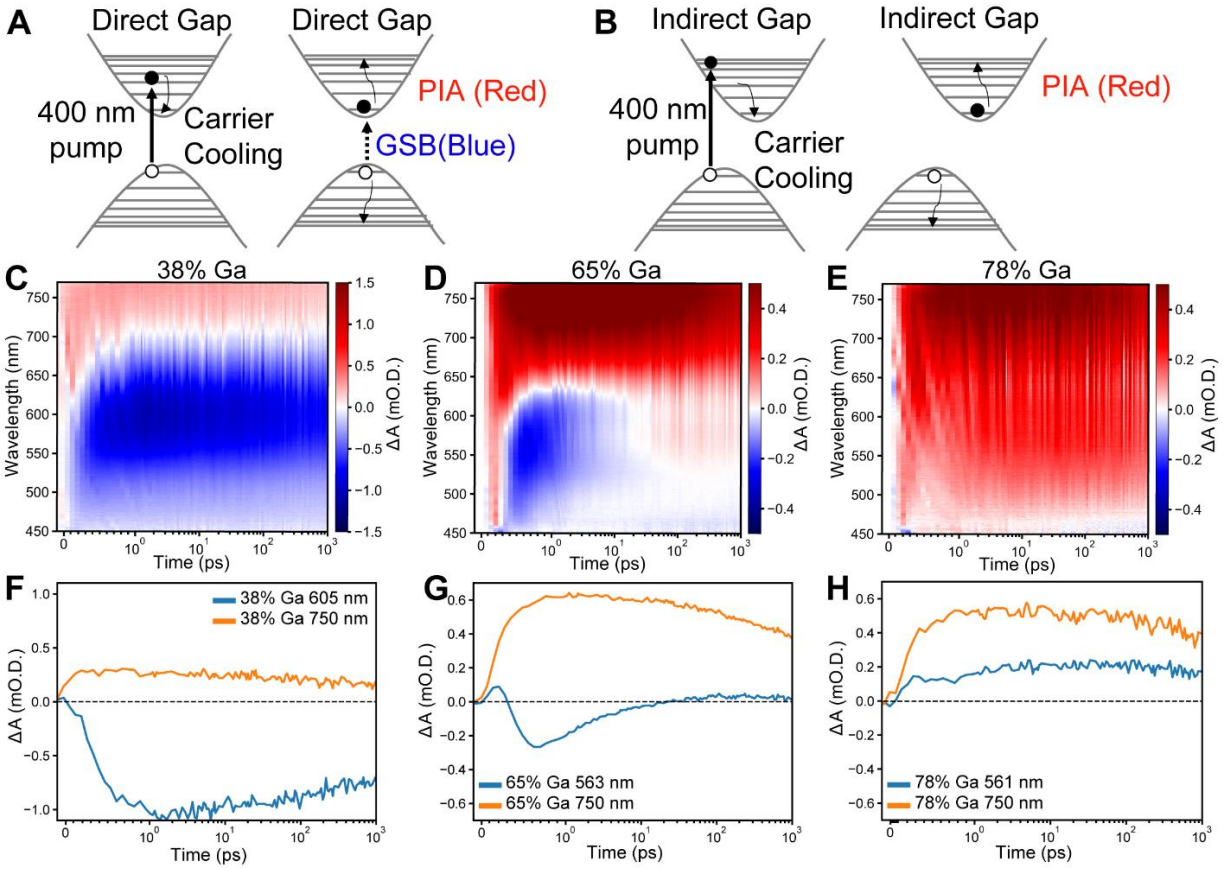

Figure 3.15. Transient absorption dynamics of $In_{1-x}Ga_xP/ZnS$ samples with 4.9 nm core. Schematic representation of the expected transient absorption signals expected for (A) a direct band gap semiconductor, and (B) an indirect band gap semiconductor. GSB: Ground State Bleach, negative ΔA; PIA: Photo-Induced Absorption, positive ΔA. Low fluence transient absorption dynamics (400 nm pump) are shown for $In_{1-x}Ga_xP/ZnS$ QDs with (C) 38%, (D) 65%, and (E) 78% gallium content. Linecuts of the TA signal at maximum bleach amplitude as well as PIA traces at 750 nm are shown for large $In_{1-x}Ga_xP/ZnS$ nanocrystals with (F) 38%, (G) 65%, and (H) 78% gallium content.

Next, we discuss the TA dynamics for the $In_{0.35}Ga_{0.65}P/ZnS$ sample. This sample showed a diffuse absorption onset and weak PL at room temperature. Transient absorption shows the formation of a bleach signal centered at 563 nm which has a maximum amplitude at 800 fs. This

bleach signal quickly decays within 20 ps such that at later times, only a PIA signal is observed across all wavelengths after ~30 ps (Figure 3.15D, G). These carrier dynamics are remarkable since they are not simply a linear combination of direct-like and indirect-like dynamics of the low and high gallium content samples, respectively. One possibility is that after photoexcitation and carrier cooling processes, there is initially a population of carriers in the direct Γ-like valleys as well as a second conduction band state which has X-like character with similar or slightly lower energy than the Γ-like valley. Intervalley scattering from the Γ-like valley to the X-like valley within ~20 ps efficiently removes carriers that can undergo direct transitions, causing the optical bleach signature to quickly decay. Interestingly the TRPL of the $In_{0.35}Ga_{0.65}P$/ZnS sample shows an IRF limited fast component, but also an extremely long decay component (Figure 3.16) suggesting that scattering back into the direct channel at late time can lead to PL. The existence of low energy dark states and higher energy bright states is consistent with the exciton manifold for the 65% Ga sample shown in Figure 3.10E.

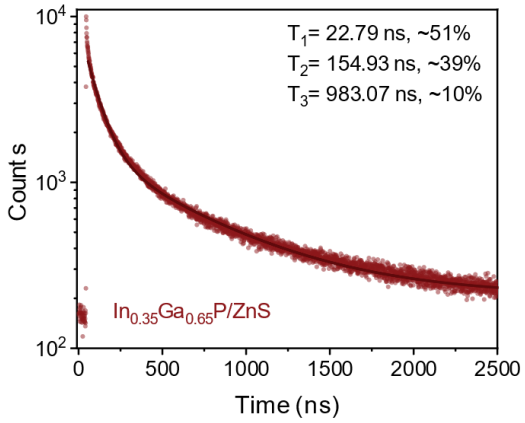

Figure 3.16. Time-resolved PL dynamics for 4.9 nm core diameter $In_{0.35}Ga_{0.65}P$/ZnS nanocrystals.

Fluence-dependent transient absorption dynamics for the samples discussed here are presented in Figure 3.17; the 38% Ga and 78% Ga samples show characteristics of Auger recombination, as

discussed later. The bleach signal of the 65% Ga sample with high pump fluences decays faster than expected for Auger recombination,[12] indicating these dynamics originate from a different process. We also pumped the $In_{0.35}Ga_{0.65}P$/ZnS sample directly into the lowest energy states using a pulse centered at 640nm (Figure 3.18) and found that the decay of the optical bleach signature follows similar dynamics as with the 400 nm pump. In this experiment, we preferentially excited the sample into band edge states which have large oscillator strength. Since we observe similar decay dynamics starting from the band edge state, we conclude that the carrier population transfer occurs directly from the direct-gap-like state to some other optically inactive state.

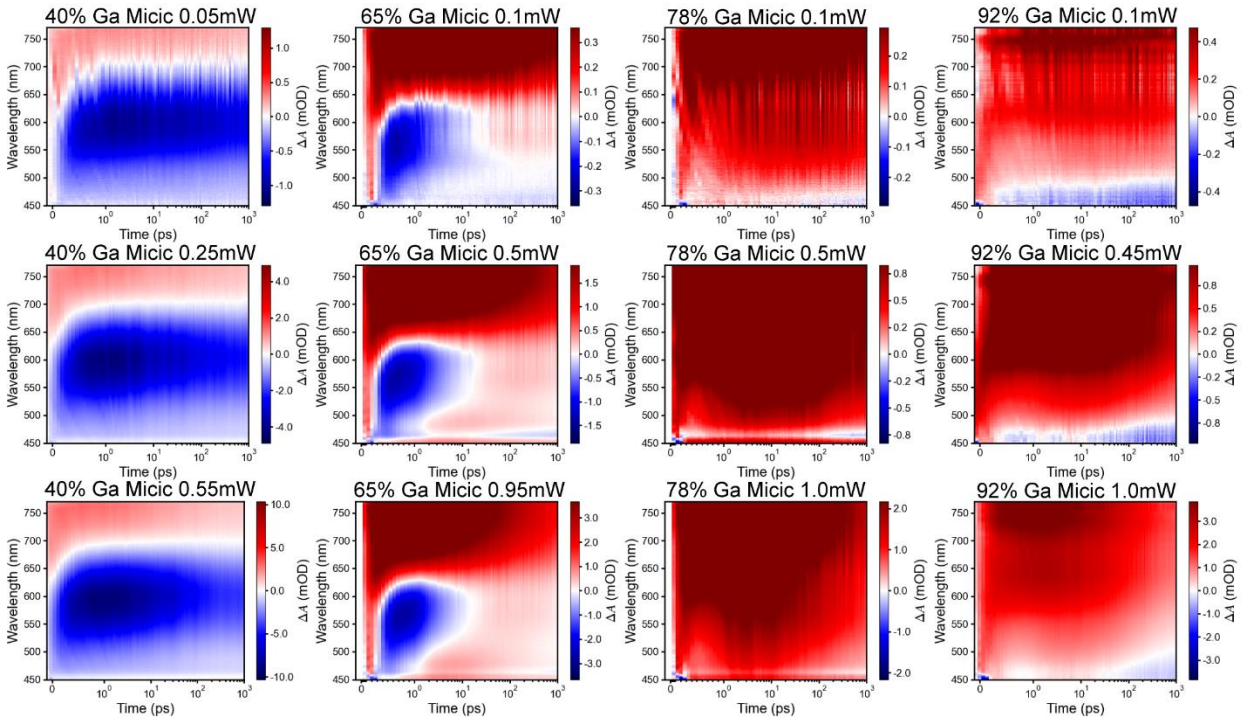

Figure 3.17. Fluence dependent transient absorption dynamics for 4.9 nm core diameter $In_{1-x}Ga_xP$/ZnS nanocrystals.
As a function of increasing Ga content from left to right (40% Ga left to 92% Ga right) and a function of increasing excitation power from top to bottom. The top plots correspond to dynamics for single excitons, the middle plots correspond to dynamics for single and bi-excitons, and the bottom plots contain multi-exciton populations.

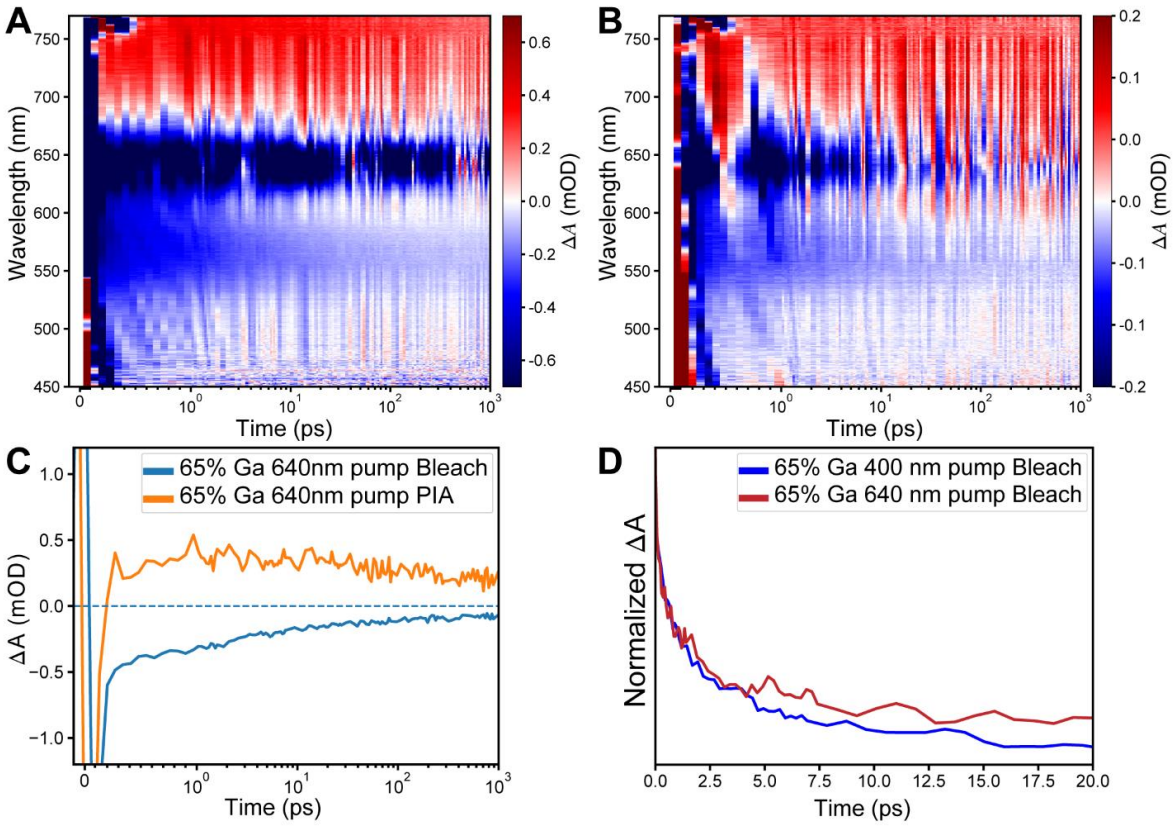

Figure 3.18. Transient absorption dynamics of 4.9 nm diameter core $In_{0.35}Ga_{0.65}P$/ZnS with resonant excitation.

Pumped with 640 nm light to directly access the ground state. (A) 1.0 mW pump and (B) 0.24 mW pump. (C) Dynamics of the bleach signal and PIA signal for a 1.0 mW pump and (D) comparison of the normalized bleach signal for a 400 nm pump and a 640 nm pump, indicating similar dynamics regardless of pump energy.

While the bleach signature decays on the ~20 ps timescale, the PIA signal remains relatively constant over the 1 ns measurement window, indicating that photoexcited carriers are still present within the nanocrystal but have a momentum mismatch that prevents optical bleaching. Due to the lighter effective mass of the electron, the PIA signal is likely sensitive primarily to the electron population, and thus the retention of the PIA signal despite the fast decay of the bleach is consistent with transfer of the electron population to X-like valleys. Taken together, the transient absorption results are consistent with conversion of these QD emitters from direct-like to indirect-like band structures at ~65% gallium. Near the direct-to-indirect transition composition, the excited state

dynamics can become complicated by nearly isoenergetic states which have different oscillator strengths.

3.6. State Degeneracy in $In_{1-x}Ga_xP/ZnS$ Nanocrystals.

This section is contributed by Dr. Justin Ondry and Prof. Richard Schaller and included here to ensure that the presented results are comprehensive.

The previously discussed transient absorption dynamics, TRPL, radiative rate and molar extinction coefficient measurements indicate that the band edge electronic state in $In_{1-x}Ga_xP/ZnS$ with >50% Ga may contain states with indirect-gap-like character which have a lower oscillator strength. In bulk III-V semiconductors, the degeneracy of the conduction band Γ-valley is 2, the conduction band L valley is 8, and the conduction band X valley is 6. In strongly quantum-confined semiconductors the definition of direct *vs* indirect transitions becomes fuzzy owing to translational momentum relaxation. The presence of multiple states arising from the different valleys in the band structure may alter the degeneracy of the band edge exciton. To understand this effect experimentally, we probe state filling in the $In_{1-x}Ga_xP/ZnS$ QDs synthesized from 4.0 nm InP cores using fluence dependent TA. We use the bleach signal for analysis, which reflects the population of the electron states due to the high degeneracy of the valence band and lighter effective mass of the electrons compared to the holes.[58] First, we determine the absorption cross section, σ, and bleach amplitude scaling factor by fitting the power dependent bleach signal at 1000 ps (after Auger recombination, ensuring only single excitons remain in the QDs) according to the equation $A = B(1-e^{-\sigma j})$ where A is the magnitude of the TA bleach signal, B is the bleach amplitude scaling factor, σ is the absorption cross section per dot at the pump wavelength, and j is the pump laser fluence (Figure 3.19A).[7] Figure 3.19B shows that all samples fall on a universal curve for single

excitations at long times, using σ and *B* determined from the fits.[52] In Figure 3.19C, we use *B* and σ to measure the normalized bleach amplitude for the early time signal at 2.5ps (before significant contribution from Auger recombination). For $In_{1-x}Ga_xP$/ZnS samples that have up to 35% Ga incorporated (red to orange dots), we observe saturation at a normalized bleach signal of 2, consistent with a band edge degeneracy of 2. The blue line is a Poissonian excitation model[59] with a degeneracy of 2 and describes the low gallium content data well. This result is consistent with the behavior of a typical III-V direct gap semiconductor. For samples with 47% and 57% gallium, we observe deviation of the fluence-dependent bleach signal from excitation statistics for a band edge degeneracy of 2. Instead, the bleach amplitude continues to increase at high excitation densities before eventually becoming sub-linear. The effect is more pronounced in the highest gallium content sample (green, 57% Ga). The data for the 47-57% Ga samples approach the excitation statistics of 4 (orange line). Thus, our data suggest that incorporating gallium into our samples is altering the degeneracy of the band edge state.

The evolution of band edge state degeneracy as more gallium is exchanged is further analyzed using the atomistic pseudopotential calculations **with Kailai Lin and Prof. Eran Rabani**. The main changes observed in bulk alloys were attributed to changes in the conduction band minima as the system transitions from InP to GaP. In NCs in the strong quantum confinement limit, one has to consider excitonic effects, however, since the calculated excitonic states near the onset of absorption comprise from mainly a single quasi-electron state at any gallium composition, it is sufficient to analyze the quasi-electron structure as the content of Ga varies. Figure 3.19D shows the results for $In_{1-x}Ga_xP$ QDs constructed from 4.0 nm InP NC. At 0% gallium (i.e., InP QD), the first several electron states are the 2-fold and 6-fold degenerate states with envelope function of 1S and 1P shapes, as expected from the effective mass approximation.[5]

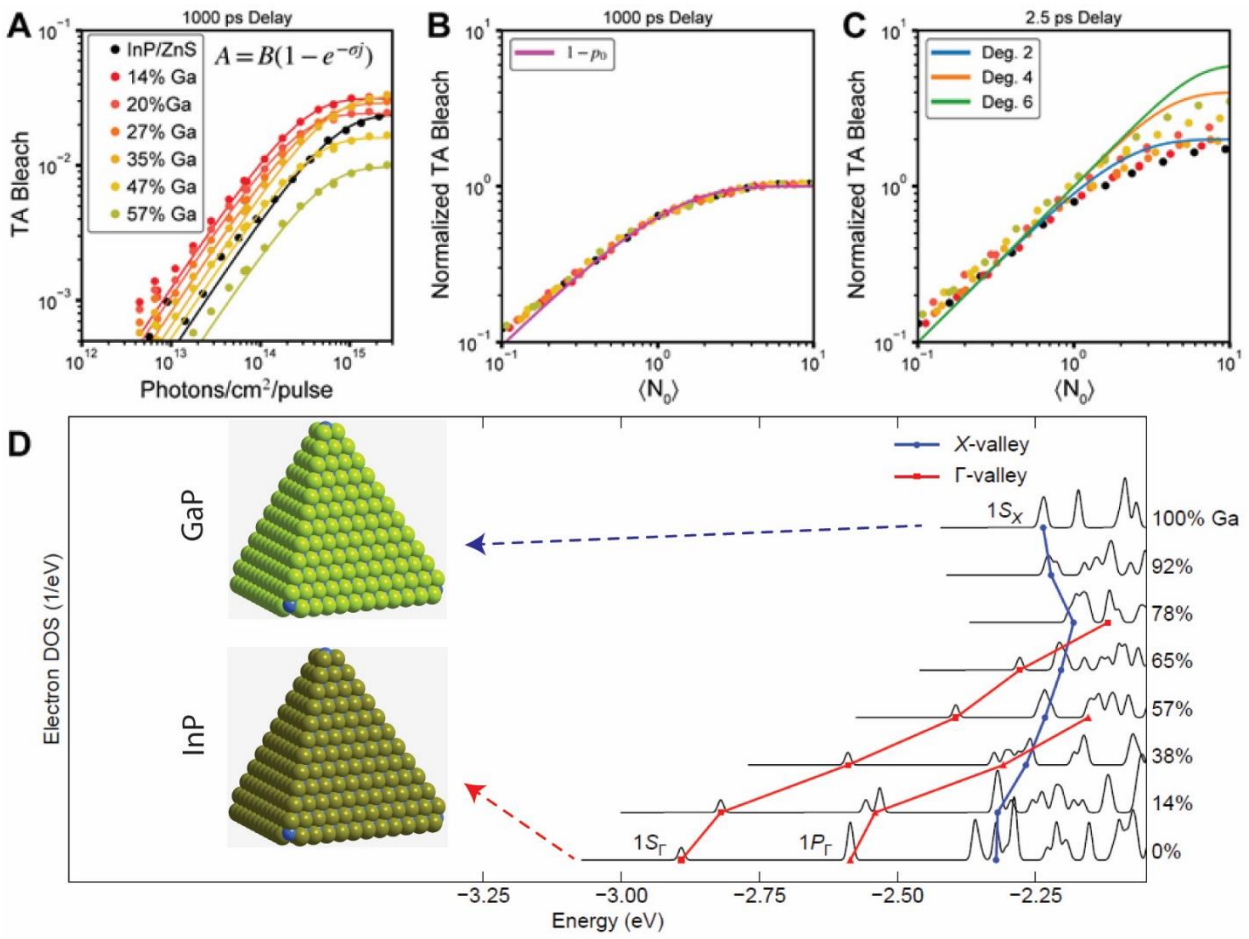

Figure 3.19. State filling in 4 nm core diameter $In_{1-x}Ga_xP/ZnS$ nanocrystals.
(A) Bleach amplitude (*A*) at 1000 ps delay as a function of pump fluence (circles) with fits to single excitation Poissonian statistics to determine the absorption cross section (σ) and bleach amplitude scaling factor (*B*) of $In_{1-x}Ga_xP/ZnS$ nanocrystals with varying gallium content. (B) Normalized TA bleach signal at 1000 ps delay as a function of the initial average excitation $\langle N_0 \rangle$. The pink line is a Poissonian distribution describing the total number of singly photoexcited nanocrystals which remain after Auger recombination. (C) Normalized TA bleach signal at 2.5 ps delay (before significant impact from Auger recombination) as a function of the initial average excitation $\langle N_0 \rangle$. The blue, orange, and green lines are model Poissonian excitation statistics for degeneracies of 2, 4, and 6 respectively for the ground state bleach signal. (D) The density of states (DOS) for the conduction band edge electron states of alloyed QDs are shown. The DOS of each gallium composition is shifted vertically for clarity. Two-fold-degenerate Γ-valley-like ($1S_\Gamma$, red squares) and 6-fold-degenerate X-valley-like ($1S_X$, blue circles) conduction band states and their energies are traced for each gallium content.

Meanwhile at 100% gallium (i.e., GaP QD), the lowest electron states are 6-fold degenerate The two Bloch functions and their corresponding electron states are named "Γ-valley" and "X-valley" respectively. Using the symmetry and spatial features of the Bloch wavefunctions, we

identify and track the $1S_\Gamma$ and $1S_X$ electron states as gallium content increases. As shown in Figure 3.19D, the energy of $1S_\Gamma$ electron states increases faster than $1S_X$, leading to a crossover of the Γ-valley-like to X-valley-like band edge electron state at 65% to 78% gallium content, in agreement with the experimental observations that the direct-to-indirect transition in $In_{1-x}Ga_xP$ QDs occur around x=65-78% and helps decipher the atomistic details in its electronic structures. The electronic structure calculations allow us to better interpret the observed increase in state degeneracy measured by TA. Formally the calculations show the lowest $1S_\Gamma$ state is 2-fold degenerate and the $1S_X$ state is 6-fold degenerate, not exactly the ~4-fold degeneracy inferred by TA. We notice that as the gallium content in $In_{1-x}Ga_xP$ is increased, the splitting between the $1S_\Gamma$ and $1S_X$ electron states decreases and are close in energy. Both the $1S_\Gamma$ and $1S_X$ electron states give rise to the manifold of bright excitonic transitions observed in Figure 3.10D. Due to the close spacing of the states, the bleach observed is actually measuring the state filling of the manifold of closely spaced states with mixed $1S_\Gamma$ and $1S_X$ character. Thus, based on our measurements, in the 57% gallium sample, up to 4 excitons can reside near the band edge simultaneously. In support of this interpretation, we observe a redshift of the bleach feature from early time to late time, suggesting that as Auger removes multicarrier population from higher energy states in the manifold, only the exciton in the lowest energy state remains (Figure 3.20).

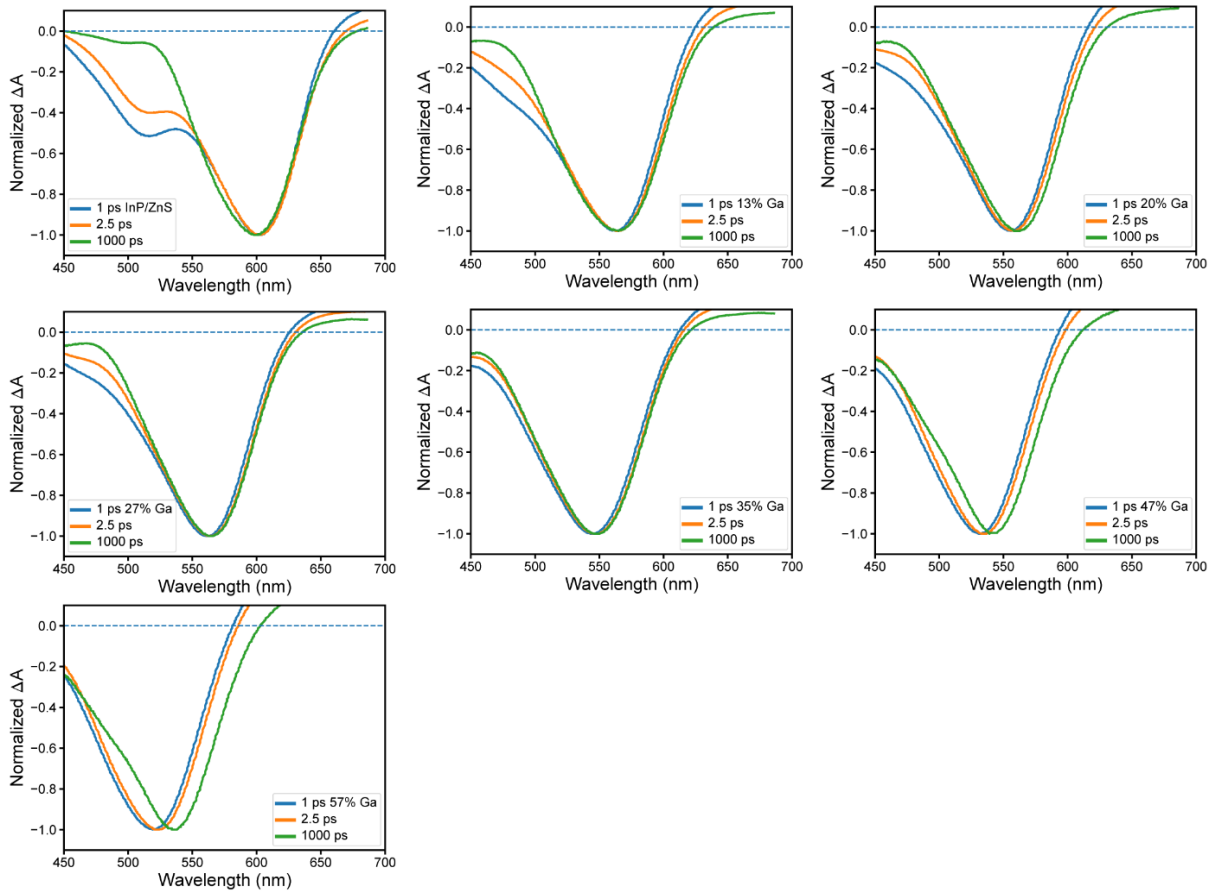

Figure 3.20. Transient absorption spectra for the 4 nm $In_{1-x}Ga_xP$/ZnS under high power excitation. $\left(\langle N \rangle \sim 10\right)$. For early times (1ps, blue and 2.5ps, orange) before Auger recombination and after Auger recombination (1000ps, green). For the samples from x=0-0.35, we do not observe significant shifts in the lowest energy bleach feature. For the samples with x=0.47-0.57, we observe the bleach feature redshifts at late times (single exciton per dot) compared to early times (multi excitons present). For the high gallium content samples, this indicates when there are multiple excitons in the sample, the additional excitons fill slightly higher energy states compared to the lowest allowed transition.

We also calculated the effective Auger constants for our samples, which allow for comparison of materials with varying sizes and compositions with their bulk counterparts. Our results fall within the data spread which has been observed for II-VI and IV-VI materials already studied.[12] This indicates alloying does little to affect the biexciton lifetimes of colloidal nanocrystals, and volume scaling effects are the key factor for determining biexciton lifetimes. Our results here provide considerable guidance for further engineering long biexciton lifetimes in III-V/II-VI

heterostructures. Alloying with a wider band gap material to achieve large cores with a given emission energy, combined with other strategies such as graded alloy shells[60] and quasi type-II band alignments[61] should enable synergistic improvement of optical properties.

3.7. PL characteristics at elevated temperatures.

When used for on-chip color conversion or incorporated into light-emitting diodes (LED), emissive materials often undergo significant thermal cycling in display panels. We employed a home-built setup to explore the PL characteristics of our emissive core-shell $In_{1-x}Ga_xP/ZnS$ samples at elevated temperatures in solution, a schematic of which is presented in Figure 3.21A. A dilute solution of QDs in 1-octadecene was sealed inside a quartz ampoule using an oxy-hydrogen torch and excited using a 450 nm laser; the PL spectra were recorded using a fiber-coupled spectrophotometer collecting emission at 90 degrees with respect to the excitation beam. The sealed ampoule was placed inside a heating block, allowing us to raise the temperature externally. Figures 3.21B, C and D, respectively, illustrate the temperature-dependent PL spectra of the bright InP/ZnS, $In_{0.65}Ga_{0.35}P/ZnS$ and $In_{0.43}Ga_{0.57}P/ZnS$ QD samples between ~296K and 577K, all derived from the 4 nm InP population. Minimal changes of the emission wavelength as a function of temperature are highly desirable to retain a consistent display color gamut and other characteristics of optoelectronic devices utilizing QD materials. To this end, we can empirically establish a Varshni relation for emissive samples by exploring the dependence of the bandgap on temperature.[62] A first-order high-temperature approximation of the semi-empirical Varshni relation, $E_g(T) = E_g(296K) - \alpha T$, allows us to employ linear fits to quantify the temperature dependence of the bandgap of the $In_{1-x}Ga_xP/ZnS$ QD samples.

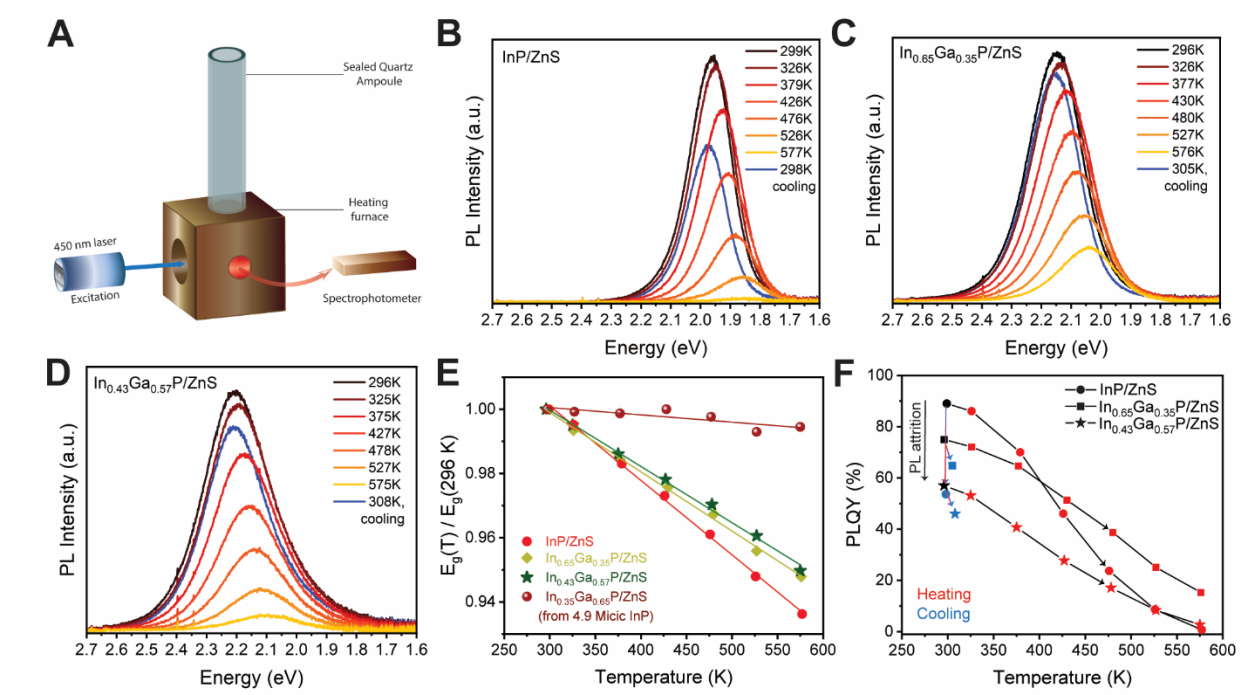

Figure 3.21. High-temperature PL characteristics of $In_{1-x}Ga_xP$/ZnS QDs.
(A) Scheme of a home-built setup for investigating the high-temperature PL characteristics of $In_{1-x}Ga_xP$/ZnS QDs. (B-D) Evolution of PL spectra as a function of temperature in emissive core-shell (B) InP/ZnS (C) $In_{0.65}Ga_{0.35}P$/ZnS and (D) $In_{0.43}Ga_{0.57}P$/ZnS QD samples, all derived from the 4 nm InP. (E) A Varshni plot (normalized at the room-temperature bandgap for all samples) exhibits linear trends in the evolution of optical bandgap with temperature. (F) Changes in PLQY as a function of temperature were estimated as fractional changes in the integrated PL intensity.

Lattice expansion at elevated temperatures contributes to a reduction of the direct bandgap between the Γ-valley of the conduction band and the top of valence band, evident in the associated Varshni plot (Figure 3.21E, 3.22). However, this trend is the opposite for the indirect gap between the Γ-valley of valence band and X-valley of the conduction band, where the bandgap increases with temperature, thus counteracting the previous effect. Indeed, the linear fits reveal that the dependence of bandgap on temperature is weaker for the $In_{1-x}Ga_xP$/ZnS samples with higher Ga content. We attribute this observation to mutual compensation of temperature effects for states with direct and indirect character and a larger contribution from the X valley indirect-like states in

samples with a higher Ga content, consistent with the previously described trends in optoelectronic properties of bulk III-V semiconductors.

We also performed temperature-dependent PL studies on emissive samples derived from the large 4.9 nm InP nanocrystals, the results of which are summarized in Figure 3.23. For the compositions close to the direct-to-indirect transition, such as $In_{0.35}Ga_{0.65}P$/ZnS, the emission wavelength becomes nearly temperature-independent between 296K and 575K (Figure 3.21E). Promisingly, these observations indicate that the alloyed nanocrystals retain their emission color gamut more efficiently than their binary counterparts at high temperatures. We used the ratio of integrated PL intensities at ambient and elevated temperatures recorded in otherwise similar conditions to estimate the PLQY of emissive samples at elevated temperatures. The reduction in PLQY at elevated temperatures is typically attributed to thermally activated trapping of photoexcited carriers, [63-65] whereas PL attrition post-annealing is ascribed to the surface reorganization and/or irreversible loss of ligands from the nanocrystal surface at higher temperatures.[66-67]

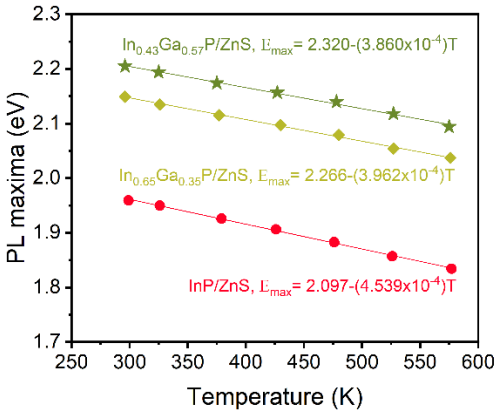

Figure 3.22. Varshni plots with linear fits.
Linear trends in the evolution of optical bandgap with temperature in $In_{1-x}Ga_xP$/ZnS samples.

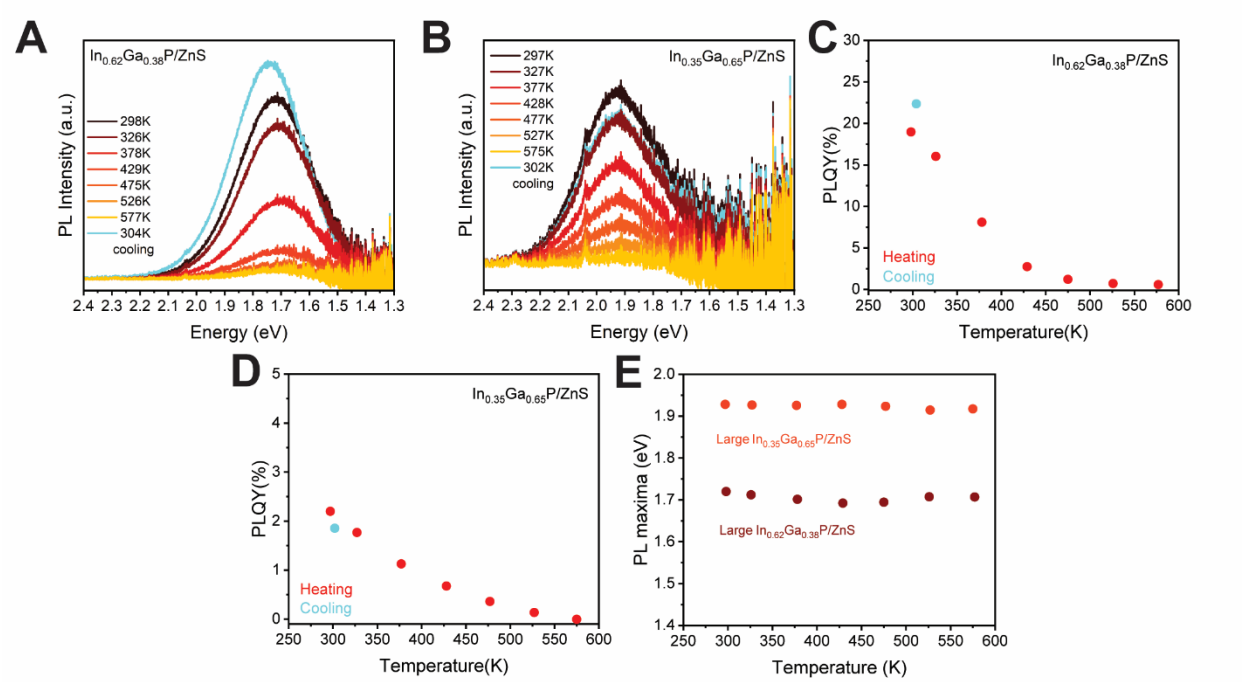

Figure 3.23. Temperature dependence of PL spectra of $In_{1-x}Ga_xP$/ZnS samples from 4.9 nm core. Evolution of PL spectra at higher temperatures in emissive core-shell (A) $In_{0.62}Ga_{0.38}P$/ZnS and (B) $In_{0.35}Ga_{0.65}P$/ZnS samples derived from the large 4.92 nm InP particles. The trends in PLQY for the same as shown in (C) and (D) are similar to those of the smaller $In_{1-x}Ga_xP$/ZnS populations described before. Evolution of the bandgap with temperature is described in a Varshni plot in (E) and indicates a considerably weaker dependence.

We measured the room temperature PLQY of the InP/ZnS and a heavily optimized proprietary InP/ZnSe/ZnS sample to be 89% and 93% respectively using an integrating sphere setup (Figure 3.24). The trends in PLQY are summarized in Figure 3.21F for clarity. We observe a steeper decline in PLQY of the InP/ZnS sample at higher temperatures as well as a poorer PL recovery after cooling as compared to its cation-exchanged $In_{1-x}Ga_xP$ counterparts, indicating that the alloy samples provide better high temperature performance. As observed via TEM, the same reaction conditions allow for the growth of only one monolayer of the ZnS shell on InP nanocrystals (Figure 3.25). The substantial lattice mismatch between InP and ZnS (7.5%) likely prevents the shell from

growing any thicker. Additionally, persistent interfacial strain at the core-shell interface can adversely affect optical performance via the propagation of defects.[36]

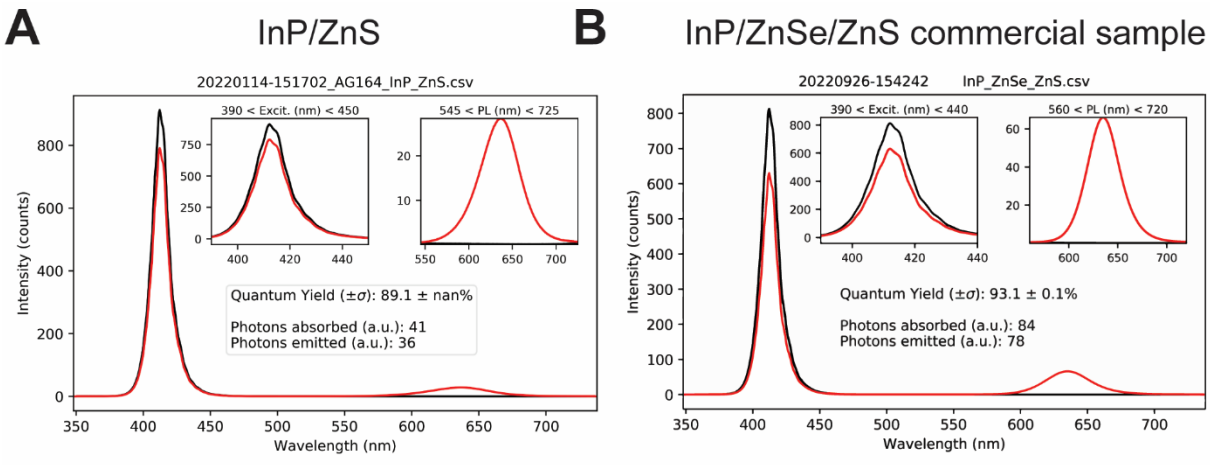

Figure 3.24. Absolute quantum yield measurements.
(A) Room temperature PLQY of the core-shell InP/ZnS sample was estimated at ~89%. (B) Room temperature PLQY of the commercial core-shell InP/ZnSe/ZnS sample was estimated at ~93%.

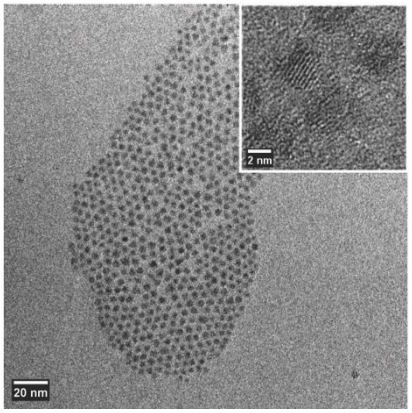

Figure 3.25. Representative TEM image of the InP/ZnS sample from the 4 nm InP core.

To test this hypothesis, we further performed temperature-dependent PL studies on the heavily optimized InP/ZnSe/ZnS commercial core-shell sample. The ZnSe shell has a lattice constant (0.5668 nm) between that of InP (0.5869 nm)[68] and ZnS (0.5441 nm), thereby reducing interfacial

strain from lattice mismatch, resulting in a near-perfect PLQY recovery post-annealing (Figure 3.26). This set of experiments reaffirms the relevance of In-to-Ga cation exchange as an important tool for reducing strains at the core-shell interface.

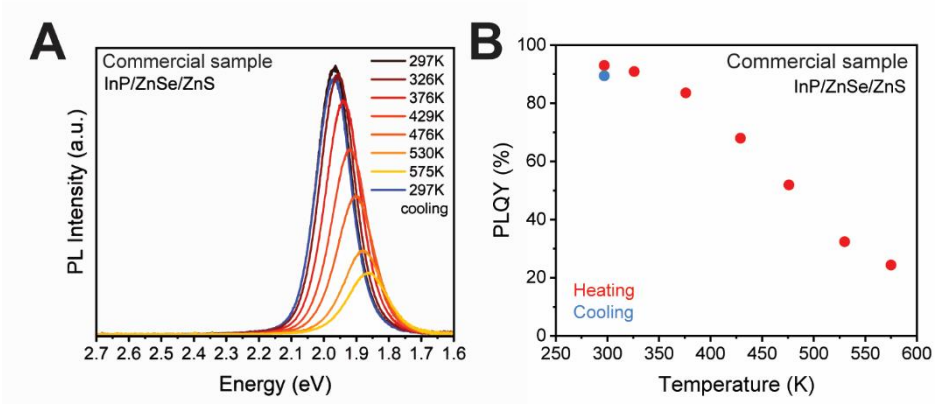

Figure 3.26. Temperature-dependent PL spectra in a commercial core-shell InP/ZnSe/ZnS sample. (A) Evolution of PL spectra (B) Retention of PLQY at elevated temperatures, as well as near-perfect QY recovery after cooling.

3.8. Conclusions.

To summarize, we have demonstrated a molten salt-based In-to-Ga cation exchange and a subsequent oxygen-free shelling protocol to yield highly emissive $In_{1-x}Ga_xP$/ZnS colloidal QDs. We have performed transient absorption spectroscopy and photoluminescence studies which demonstrate that the incorporation of gallium is accompanied by a decrease in oscillator strength of excitonic transitions, as indicated by a decreasing absorption cross-section and a monotonic increase in the radiative lifetime of emission. Atomistic calculations agree well with experimental observations and confirm the trends of optical properties as gallium composition changes in the alloyed QDs. These results inform us that incorporating more gallium in $In_{1-x}Ga_xP$/ZnS CQDs can only be part of a strategy to prepare blue III-P emitters since high gallium contents result in low oscillator strength of emissive states. Compared to InP, a better lattice match between $In_{1-x}Ga_xP$ and the ZnS shell allows for better PLQY recovery during thermal cycling. These results establish

molten-salt synthesized $In_{1-x}Ga_xP$ nanocrystals as a viable alternative to InP for designing next-generation III-V QDs for displays and other applications. Further, we establish that alloying can decouple mutually size dependent properties enabling flexible engineering of emitters with desired properties.

3.9. Materials and methods.

Chemicals. Trioctylphosphine (TOP, 97%), trioctylphosphine oxide (TOPO, 99%), hexamethylphosphoramide (HMPA, 99%), myristic acid (99%), sulfur (99.998%) and anhydrous solvents (hexane, toluene, ethanol (EtOH), methyl acetate, isopropanol (IPA), acetonitrile (MeCN)) were purchased from Sigma Aldrich and used as received. Oleylamine (OAm, technical grade, 70%) was purchased from Sigma Aldrich and purified by freezing, thawing, and then centrifuging to remove any insoluble solids. The resulting purified oleylamine was dried under dynamic vacuum at 100^{o}C overnight and stored in a nitrogen glovebox. 1-Octadecene (ODE, 90%) was purchased from Sigma Aldrich, dried under dynamic vacuum at 80^{o}C overnight and stored in a nitrogen glovebox. Dodecylamine (98%) and octadecylamine (technical grade, 90%) were purchased from Sigma Aldrich and dried under dynamic vacuum before storage in a nitrogen glovebox. Potassium iodide (ultra-dry, 99.998%), gallium(iii) iodide (ultra-dry, 99.999%), indium(iii) acetate (99.99%), zinc chloride (ultra-dry, 99.999%) and N,N-dimethylformamide (DMF, anhydrous 99.9%) were purchased from Alfa Aesar and used as received. *Tris*(trimethylsilyl)phosphine ($(TMS)_3P$, 98%, stored frozen) and indium(iii) chloride (anhydrous, 99.999%) were purchased from Strem Chemicals and used as received.

InP nanocrystal synthesis.

Large InP QDs. Large InP nanocrystals (~4.9 nm diameter) were synthesized following a route established by Micic and others. Briefly, 1 g $InCl_3$ (4.52 mmol), 1.5 g trioctylphosphine

oxide (3.88 mmol) and 15 mL of trioctylphosphine were combined in a nitrogen glovebox and stirred at room temperature. After complete dissolution of the solids, the solution was filtered through a 0.2 μm PTFE filter into a three-neck flask, which was then sealed and transferred air-free to a Schlenk line under nitrogen purge. With the contents of the flask at 25°C, 0.75g (869 μL, 4 mmol) of tris(trimethylsilyl)phosphine was injected. The temperature of the flask was then raised to 270°C and maintained under stirring for 30 hours. Particles were washed under the inert atmosphere of a nitrogen filled glovebox by precipitation with ethanol followed by redispersal in toluene. After another step of precipitation/redispersal, the particles were size selectively precipitated from toluene by incremental addition of ethanol followed by centrifugation after each addition. The largest particles contained in the first fraction were used in further steps.

InP QDs of intermediate size. A consistent sample of nearly monodisperse InP nanocrystals, (4 nm diameter), was obtained from commercial sources as a solution in octadecene (ODE) and stored in a nitrogen glove box. The QDs were precipitated by addition of ethanol (EtOH), centrifuged, and redispersed in toluene for further processing.

Small InP QDs. The synthesis of small InP nanocrystals (~3.2 nm diameter) was adapted from a prior report by the Peng group. 5 mmol $In(Ac)_3$, 15 mmol myristic acid and 35 mL octadecene were mixed in a 250 mL flask. After degassing for 1 hour under vacuum at 120 °C, 5 mL TOP was injected. Into this solution, a solution of 2.5 mmol $(TMS)_3P$ in ODE (8 mL) was injected at 150°C. The reaction temperature was next raised to 270 °C for growing the nanocrystals. After 5 minutes, the reaction mixture was cooled down, and the synthesized particles were washed three times using ethanol and methyl acetate with added

trioctylphosphine ligands. Finally, the nanocrystals were stored as a colloidal solution in hexane.

GaI_3 ligand exchange. The GaI_3 ligand exchange was adapted from a previous publication. A solution of as-synthesized InP in hexane (15 mL, 1 mg/mL) was layered atop a solution of GaI_3 in dimethylformamide (DMF) (2 mL, 0.05 M), and stirred until all particles transferred to the DMF phase. The particles were precipitated by addition of toluene, centrifuged, and redispersed in DMF. The washing step was repeated 3 times. The particles were then redispersed in acetonitrile, washed with toluene, and allowed to dry overnight under nitrogen. A stable colloidal solution of GaI_3 exchanged nanocrystals could be obtained in DMF plus 3 vol% HMPA in order to obtain absorption spectra.

Molten salt dispersal and subsequent gallium exchange. A $KGaI_4$ salt phase was obtained by grinding and mixing GaI_3 and KI in a 1:1 molar ratio and subsequently melting the mixture under stirring at 250^{o}C on a hotplate (using a glass-coated stir-bar). A portion of 1.2 g of the salt mixture was combined with the GaI_3 ligand-exchanged NCs by adding them to the salt as a dry powder and combining them in a mortar and pestle. Next, the particle-salt mixture was loaded into a quartz ampoule and heated to 250^{o}C under vigorous stirring to obtain a visually homogeneous dispersion. The ampoule was sealed under vacuum using an oxy-hydrogen torch, transferred into a muffle furnace, and annealed for different durations at different temperatures. A higher annealing temperature or longer duration led to higher extents of gallium incorporation.

QD recovery following molten salt treatment. The salt matrix was dissolved in acetonitrile (~6 mL) at 60 °C, and the QDs were recovered as a solid by centrifugation. The QD solid was washed with 4 mL fresh acetonitrile to remove residual salt. The particles could regain colloidal stability

in nonpolar solvents through treatment with 1:1 molar dodecylamine/octadecylamine. The amine recovery was performed by utilizing an adaptation of the entropic ligand mixture concept introduced by the Peng group.[42] A solution of dodecylamine and octadecylamine (0.01 M each) was obtained by dissolving the corresponding ligands in toluene at 80^{o}C under stirring. 2 ml of this toluene solution was combined with the QD powder and stirred at 60^{o}C for an hour. The resulting QD solution in toluene was washed with methyl acetate to remove excess ligands and then stored in toluene.

ZnS shelling. In a typical shelling step using $In_{1-x}Ga_xP$ cores derived from InP particles of the large (Micic) and medium sizes (commercial), anhydrous $ZnCl_2$ (157 mg, 1.15 mmol) was combined with 5 ml of freeze-thaw purified oleylamine and 2.6 ml of TOP and degassed at 120^{o}C for 1 hour. The amine capped $In_{1-x}Ga_xP$ particles were introduced into the reaction mixture as a toluene solution (500 µL, ~30 mg/ml) under N_2 flow, followed by degassing at 120^{o}C for another 30 min. Next, the temperature was raised to 300^{o}C, and 2.4 ml of a 0.4 M solution of TOP-S was slowly injected into the reaction mixture at a rate of 1 ml/hour using a syringe pump. The reaction mixture was stirred at 300^{o}C for a total of 3 hours, cooled down, diluted with hexane, and washed with ethanol. Once separated from the reaction mixture, the particles were redispersed in hexane, washed using a mixture of methyl acetate and acetonitrile, and finally stored as a stable colloidal solution in hexane.

While shelling the 4 nm InP particles, native organic ligands were first exchanged with GaI_3, then the particles were dispersed in toluene with the addition of dodecylamine/ octadecylamine. Subsequently, the same synthetic protocol could be followed to grow a ZnS shell on the ligand exchanged particles.

In order to shell alloyed $In_{1-x}Ga_xP$ cores derived from small (Peng) InP particles, anhydrous $ZnCl_2$ (628 mg, 4.60 mmol) was combined with 7 ml of freeze-thaw purified oleylamine along with 3 ml of TOP and degassed at 120^oC for 1 hour. The amine-capped $In_{1-x}Ga_xP$ particles were introduced into the reaction mixture as a toluene solution (500 µL, ~30 mg/ml) under N_2 flow, followed by degassing at 120^oC for another 30 min. Next, the temperature was raised to 300^oC, and 4.8 ml of a 0.8 M solution of TOP-S was slowly injected into the reaction mixture at a rate of 2 ml/hour using a syringe pump. The reaction mixture was stirred at 300^oC for a total of 3 hours, cooled down, diluted with hexane, and washed with ethanol. Once separated from the reaction mixture, the particles were redispersed in hexane, washed using a mixture of methyl acetate and acetonitrile, and finally stored as a stable colloidal solution in hexane.

Core-shell InP/ZnSe/ZnS nanocrystals. Colloidal core-shell InP/ZnSe/ZnS nanocrystal samples with near unity PLQY were obtained from commercial sources as a solution in hexane and were stored in a nitrogen glove box.

Optical characterization. UV-vis spectra were collected on colloidal solutions of QDs with a Shimadzu UV-3600i Plus UV-Vis-NIR spectrophotometer in transmission mode. Photoluminescence emission spectra and Excitation-Emission Maps were collected on a Horiba Jobin Yvon Fluorolog-3 spectrophotometer equipped with a Synapse OE-CCD detector. Time resolved PL decay profiles were recorded with a Horiba Jobin Yvon Tempro fluorescence lifetime system with a 392nm pulsed LED source. High temperature PL spectra were recorded using a dilute colloidal solution of nanocrystals in ODE contained in a quartz ampoule sealed under inert atmosphere. A custom-built furnace setup interfaced with an Ocean Insight HR4Pro high-resolution spectrometer was utilized to record the high temperature PL spectra, which were

corrected using a calibrated Ocean Insight HL-3plus precision lamp source. A 450 nm laser (CPS450, Thorlabs, 4.5 mW) was employed as the excitation source.

PL quantum yield was calculated relative to a dilute solution of the reference dye coumarin 153 in ethanol. Integrated areas of the recorded PL spectra were used to estimate the quantum yield as

$$\varphi = \varphi_{ref} \frac{I_s}{I_{ref}} \frac{f_{ref}}{f_s} \frac{\eta_s^{\,2}}{\eta_{ref}^{\,2}}$$

Where s is the sample and ref is coumarin 153. The quantum yield of coumarin 153 was taken as 0.53. I represents the integrated PL intensity, f denotes the absorption factor at excitation wavelength, and n representing the refractive indices of the solvents. Absolute PLQY measurements were carried out using an integrating sphere (Labsphere) coupled with a computer-controlled spectrometer (Ocean Optics QE Pro) together with a 415-nm fiber-coupled LED excitation source (M415F3, Thorlabs, 14.4 mW).

Powder X-ray diffraction. Powder x-ray diffraction patterns were collected on a Rigaku Miniflex X-ray diffractometer. Samples were deposited on (511)-oriented Si low background substrates. For $In_{1-x}Ga_xP$ nanocrystals, the lattice parameter was extracted by employing Le Bail refinement to fit the full XRD pattern using the TOPAS software package (version 5, Bruker AXS). A twelfth-order Chebyshev polynomial was used to fit the background, and the crystalline phase was assumed to contain a zinc blende phase (F $\overline{4}$ 3m space group) exclusively. The lattice constants of bulk InP (5.8687 Å) and GaP (5.4505 Å) were used to calculate the alloy composition *x*, assuming a linear relationship between the lattice constant and alloying composition (Vegard's law) as follows:

$$a\left(In_{1-x}Ga_xP\right) = \left(1-x\right)a_{InP} + xa_{GaP}$$

Transmission electron microscopy. TEM images were obtained on an FEI Tecnai F30 microscope at 300 kV.

Small Angle X-ray Scattering (SAXS). Colloidal solutions of QDs in toluene were prepared in sealed Kapton capillaries for small-angle x-ray scattering (SAXS) experiments. SAXS patterns were collected using a SAXSLab Ganesha instrument with Cu Kα radiation (λ = 1.54 Å). The SAXS curves were analyzed by fitting to a quantitative model in Igor Pro using the Irena package (available at http://usaxs.xray.aps.anl.gov/staff/ilavsky/irena.html).[40] The scattering curves were fit in the particle size distribution module using the model-free Maximum Entropy approach. The particles' form factor was assumed to be that of a sphere with an aspect ratio of 1. The extracted size distributions were further fit with symmetric Gaussians to estimate average particle diameters along with the associated standard deviations.

X-Ray Fluorescence (XRF). XRF elemental analysis was performed using a Rigaku NEX DE instrument under helium atmosphere.

Transient Absorption Spectroscopy. Measurements were performed using a 35-fs, 2-kHz Ti:sapphire laser with time-delayed white light probe pulses produced in a 2 mm sapphire plate and 1-kHz pump pulses centered at 400 nm produced from second harmonic generation of the fundamental. At these pump energies, we are exciting the samples well above the band gap of the $In_{1-x}Ga_xP$ core, but below the absorption onset of the ZnS shell. All time-resolved absorption spectra were collected at room temperature from stirred solutions, beginning at low excitation fluence such that only single-exciton dynamics were observed.

3.10. Chapter 3 bibliography.

1. Gupta, A.; Ondry, J. C.; Lin, K.; Chen, Y.; Hudson, M. H.; Chen, M.; Schaller, R. D.; Rossini, A. J.; Rabani, E.; Talapin, D. V., Composition-Defined Optical Properties and the Direct-to-Indirect Transition in Core–Shell $In_{1-x}Ga_xP$/ZnS Colloidal Quantum Dots. *J. Am. Chem. Soc.* **2023,** *145* (30), 16429-16448. DOI: 10.1021/jacs.3c02709.

2. Ashcroft, N. W.; Mermin, N. D., *Solid State Physics*. W. B. Saunders Company: 1976.

3. Brus, L. E., Electron–electron and electron-hole interactions in small semiconductor crystallites: The size dependence of the lowest excited electronic state. *J. Chem. Phys.* **1984,** *80* (9), 4403-4409. DOI: 10.1063/1.447218.

4. Schaller, R. D.; Klimov, V. I., High Efficiency Carrier Multiplication in PbSe Nanocrystals: Implications for Solar Energy Conversion. *Phys. Rev. Lett.* **2004,** *92* (18), 186601. DOI: 10.1103/PhysRevLett.92.186601.

5. Ellingson, R. J.; Beard, M. C.; Johnson, J. C.; Yu, P.; Micic, O. I.; Nozik, A. J.; Shabaev, A.; Efros, A. L., Highly Efficient Multiple Exciton Generation in Colloidal PbSe and PbS Quantum Dots. *Nano Lett.* **2005,** *5* (5), 865-871. DOI: 10.1021/nl0502672.

6. Efros, A. L.; Rosen, M., The Electronic Structure of Semiconductor Nanocrystals. *Annu. Rev. Mater. Sci.* **2000,** *30* (1), 475-521. DOI: 10.1146/annurev.matsci.30.1.475.

7. Chang, A. Y.; Liu, W.; Talapin, D. V.; Schaller, R. D., Carrier Dynamics in Highly Quantum-Confined, Colloidal Indium Antimonide Nanocrystals. *ACS Nano* **2014,** *8* (8), 8513-8519. DOI: 10.1021/nn5031274.

8. Murray, C. B.; Norris, D. J.; Bawendi, M. G., Synthesis and characterization of nearly monodisperse CdE (E = sulfur, selenium, tellurium) semiconductor nanocrystallites. *J. Am. Chem. Soc.* **1993,** *115* (19), 8706-8715. DOI: 10.1021/ja00072a025.

9. Balan, A. D.; Eshet, H.; Olshansky, J. H.; Lee, Y. V.; Rabani, E.; Alivisatos, A. P., Effect of Thermal Fluctuations on the Radiative Rate in Core/Shell Quantum Dots. *Nano Lett.* **2017,** *17* (3), 1629-1636. DOI: 10.1021/acs.nanolett.6b04816.

10. Efros, A. L.; Brus, L. E., Nanocrystal Quantum Dots: From Discovery to Modern Development. *ACS Nano* **2021,** *15* (4), 6192-6210. DOI: 10.1021/acsnano.1c01399.

11. Klimov, V. I.; Schwarz, C. J.; McBranch, D. W.; Leatherdale, C. A.; Bawendi, M. G., Ultrafast dynamics of inter- and intraband transitions in semiconductor nanocrystals: Implications for quantum-dot lasers. *Phys. Rev. B* **1999,** *60* (4), R2177-R2180. DOI: 10.1103/PhysRevB.60.R2177.

12. Robel, I.; Gresback, R.; Kortshagen, U.; Schaller, R. D.; Klimov, V. I., Universal Size-Dependent Trend in Auger Recombination in Direct-Gap and Indirect-Gap Semiconductor Nanocrystals. *Phys. Rev. Lett.* **2009,** *102* (17), 177404. DOI: 10.1103/PhysRevLett.102.177404.

13. Carroll, G. M.; Limpens, R.; Neale, N. R., Tuning Confinement in Colloidal Silicon Nanocrystals with Saturated Surface Ligands. *Nano Lett.* **2018,** *18* (5), 3118-3124. DOI: 10.1021/acs.nanolett.8b00680.

14. Klimov, V. I.; Schwarz, C. J.; McBranch, D. W.; White, C. W., Initial carrier relaxation dynamics in ion-implanted Si nanocrystals: Femtosecond transient absorption study. *Appl. Phys. Lett.* **1998,** *73* (18), 2603-2605. DOI: 10.1063/1.122519.

15. Hybertsen, M. S., Absorption and emission of light in nanoscale silicon structures. *Phys. Rev. Lett.* **1994,** *72* (10), 1514-1517. DOI: 10.1103/PhysRevLett.72.1514.

16. Kovalev, D.; Heckler, H.; Ben-Chorin, M.; Polisski, G.; Schwartzkopff, M.; Koch, F., Breakdown of the k-Conservation Rule in Si Nanocrystals. *Phys. Rev. Lett.* **1998,** *81* (13), 2803-2806. DOI: 10.1103/PhysRevLett.81.2803.

17. Onton, A.; Lorenz, M. R.; Reuter, W., Electronic Structure and Luminescence Processes in $In_{1-x}Ga_xP$ Alloys. *J. Appl. Phys.* **1971,** *42* (9), 3420-3432. DOI: 10.1063/1.1660748.

18. James, L. W.; Van Dyke, J. P.; Herman, F.; Chang, D. M., Band Structure and High-Field Transport Properties of InP. *Phys. Rev. B* **1970,** *1* (10), 3998-4004. DOI: 10.1103/PhysRevB.1.3998.

19. Williams, G. P.; Cerrina, F.; Lapeyre, G. J.; Anderson, J. R.; Smith, R. J.; Hermanson, J., Experimental study of the band structure of GaP, GaAs, GaSb, InP, InAs, and InSb. *Phys. Rev. B* **1986,** *34* (8), 5548-5557. DOI: 10.1103/PhysRevB.34.5548.

20. Onton, A.; Chicotka, R. J., Photoluminescence Processes in $In_{1-x}Ga_xP$ at 2°K. *Phys. Rev. B* **1971,** *4* (6), 1847-1853. DOI: 10.1103/PhysRevB.4.1847.

21. Lee, J.-W.; Schremer, A. T.; Fekete, D.; Shealy, J. R.; Ballantyne, J. M., Growth of direct bandgap GalnP quantum dots on GaP substrates. *J. Electron. Mater.* **1997,** *26* (10), 1199-1204. DOI: 10.1007/s11664-997-0020-0.

22. Gao, H.; Sun, Q.; Sun, W.; Tan, H. H.; Jagadish, C.; Zou, J., Understanding the Effect of Catalyst Size on the Epitaxial Growth of Hierarchical Structured InGaP Nanowires. *Nano Lett.* **2019,** *19* (11), 8262-8269. DOI: 10.1021/acs.nanolett.9b03835.

23. Gao, H.; Sun, W.; Sun, Q.; Tan, H. H.; Jagadish, C.; Zou, J., Compositional Varied Core–Shell InGaP Nanowires Grown by Metal–Organic Chemical Vapor Deposition. *Nano Lett.* **2019,** *19* (6), 3782-3788. DOI: 10.1021/acs.nanolett.9b00915.

24. Kornienko, N.; Whitmore, D. D.; Yu, Y.; Leone, S. R.; Yang, P., Solution Phase Synthesis of Indium Gallium Phosphide Alloy Nanowires. *ACS Nano* **2015,** *9* (4), 3951-3960. DOI: 10.1021/nn507335j.

25. Srivastava, V.; Liu, W.; Janke, E. M.; Kamysbayev, V.; Filatov, A. S.; Sun, C.-J.; Lee, B.; Rajh, T.; Schaller, R. D.; Talapin, D. V., Understanding and Curing Structural Defects in Colloidal GaAs Nanocrystals. *Nano Lett.* **2017,** *17* (3), 2094-2101. DOI: 10.1021/acs.nanolett.7b00481.

26. Li, Y.; Hou, X.; Dai, X.; Yao, Z.; Lv, L.; Jin, Y.; Peng, X., Stoichiometry-Controlled InP-Based Quantum Dots: Synthesis, Photoluminescence, and Electroluminescence. *J. Am. Chem. Soc.* **2019,** *141* (16), 6448-6452. DOI: 10.1021/jacs.8b12908.

27. Kim, Y.; Ham, S.; Jang, H.; Min, J. H.; Chung, H.; Lee, J.; Kim, D.; Jang, E., Bright and Uniform Green Light Emitting InP/ZnSe/ZnS Quantum Dots for Wide Color Gamut Displays. *ACS Appl. Nano Mater.* **2019,** *2* (3), 1496-1504. DOI: 10.1021/acsanm.8b02063.

28. Won, Y.-H.; Cho, O.; Kim, T.; Chung, D.-Y.; Kim, T.; Chung, H.; Jang, H.; Lee, J.; Kim, D.; Jang, E., Highly efficient and stable InP/ZnSe/ZnS quantum dot light-emitting diodes. *Nature* **2019,** *575* (7784), 634-638. DOI: 10.1038/s41586-019-1771-5.

29. Ramasamy, P.; Ko, K.-J.; Kang, J.-W.; Lee, J.-S., Two-Step "Seed-Mediated" Synthetic Approach to Colloidal Indium Phosphide Quantum Dots with High-Purity Photo- and Electroluminescence. *Chem. Mater.* **2018,** *30* (11), 3643-3647. DOI: 10.1021/acs.chemmater.8b02049.

30. Kim, Y.-H.; Jun, Y.-w.; Jun, B.-H.; Lee, S.-M.; Cheon, J., Sterically Induced Shape and Crystalline Phase Control of GaP Nanocrystals. *J. Am. Chem. Soc.* **2002,** *124* (46), 13656-13657. DOI: 10.1021/ja027575b.

31. Micic, O. I.; Sprague, J. R.; Curtis, C. J.; Jones, K. M.; Machol, J. L.; Nozik, A. J.; Giessen, H.; Fluegel, B.; Mohs, G.; Peyghambarian, N., Synthesis and Characterization of InP, GaP, and $GaInP_2$ Quantum Dots. *J. Phys. Chem.* **1995,** *99* (19), 7754-7759. DOI: 10.1021/j100019a063.

32. Kim, K.-H.; Jo, J.-H.; Jo, D.-Y.; Han, C.-Y.; Yoon, S.-Y.; Kim, Y.; Kim, Y.-H.; Ko, Y. H.; Kim, S. W.; Lee, C.; Yang, H., Cation-Exchange-Derived InGaP Alloy Quantum Dots toward Blue Emissivity. *Chem. Mater.* **2020,** *32* (8), 3537-3544. DOI: 10.1021/acs.chemmater.0c00551.

33. Jeong, B. G.; Chang, J. H.; Hahm, D.; Rhee, S.; Park, M.; Lee, S.; Kim, Y.; Shin, D.; Park, J. W.; Lee, C.; Lee, D. C.; Park, K.; Hwang, E.; Bae, W. K., Interface polarization in heterovalent core–shell nanocrystals. *Nat. Mater.* **2022,** *21* (2), 246-252. DOI: 10.1038/s41563-021-01119-8.

34. Zhang, H.; Dasbiswas, K.; Ludwig, N. B.; Han, G.; Lee, B.; Vaikuntanathan, S.; Talapin, D. V., Stable colloids in molten inorganic salts. *Nature* **2017,** *542* (7641), 328-331. DOI: 10.1038/nature21041.

35. Kamysbayev, V.; Srivastava, V.; Ludwig, N. B.; Borkiewicz, O. J.; Zhang, H.; Ilavsky, J.; Lee, B.; Chapman, K. W.; Vaikuntanathan, S.; Talapin, D. V., Nanocrystals in Molten Salts and Ionic Liquids: Experimental Observation of Ionic Correlations Extending beyond the Debye Length. *ACS Nano* **2019,** *13* (5), 5760-5770. DOI: 10.1021/acsnano.9b01292.

36. Srivastava, V.; Kamysbayev, V.; Hong, L.; Dunietz, E.; Klie, R. F.; Talapin, D. V., Colloidal Chemistry in Molten Salts: Synthesis of Luminescent $In_{1-x}Ga_xP$ and $In_{1-x}Ga_xAs$ Quantum Dots. *J. Am. Chem. Soc.* **2018,** *140* (38), 12144-12151. DOI: 10.1021/jacs.8b06971.

37. Hudson, M. H.; Gupta, A.; Srivastava, V.; Janke, E. M.; Talapin, D. V., Synthesis of $In_{1-x}Ga_xP$ Quantum Dots in Lewis Basic Molten Salts: The Effects of Surface Chemistry, Reaction Conditions, and Molten Salt Composition. *J. Phys. Chem. C* **2022,** *126* (3), 1564-1580. DOI: 10.1021/acs.jpcc.1c10394.

38. Gupta, A.; Ondry, J. C.; Chen, M.; Hudson, M. H.; Coropceanu, I.; Sarma, N. A.; Talapin, D. V., Diffusion-Limited Kinetics of Isovalent Cation Exchange in III–V Nanocrystals Dispersed in Molten Salt Reaction Media. *Nano Lett.* **2022,** *22* (16), 6545-6552. DOI: 10.1021/acs.nanolett.2c01699.

39. Mićić, O. I.; Nozik, A. J.; Lifshitz, E.; Rajh, T.; Poluektov, O. G.; Thurnauer, M. C., Electron and Hole Adducts Formed in Illuminated InP Colloidal Quantum Dots Studied by Electron Paramagnetic Resonance. *J. Phys. Chem. B* **2002,** *106* (17), 4390-4395. DOI: 10.1021/jp014180q.

40. Ilavsky, J.; Jemian, P. R., Irena: Tool Suite for Modeling and Analysis of Small-Angle Scattering. *J. Appl. Crystallogr.* **2009,** *42* (2), 347-353. DOI: doi:10.1107/S0021889809002222.

41. Kroupa, D. M.; Voros, M.; Brawand, N. P.; McNichols, B. W.; Miller, E. M.; Gu, J.; Nozik, A. J.; Sellinger, A.; Galli, G.; Beard, M. C., Tuning colloidal quantum dot band edge positions through solution-phase surface chemistry modification. *Nat. Commun.* **2017,** *8*, 15257. DOI: 10.1038/ncomms15257.

42. Yang, Y.; Qin, H.; Jiang, M.; Lin, L.; Fu, T.; Dai, X.; Zhang, Z.; Niu, Y.; Cao, H.; Jin, Y.; Zhao, F.; Peng, X., Entropic Ligands for Nanocrystals: From Unexpected Solution Properties to Outstanding Processability. *Nano Lett.* **2016,** *16* (4), 2133-2138. DOI: 10.1021/acs.nanolett.6b00730.

43. Calvin, J. J.; Kaufman, T. M.; Sedlak, A. B.; Crook, M. F.; Alivisatos, A. P., Observation of ordered organic capping ligands on semiconducting quantum dots via powder X-ray diffraction. *Nat. Commun.* **2021,** *12* (1), 2663. DOI: 10.1038/s41467-021-22947-x.

44. Wang, L.-W.; Zunger, A., Pseudopotential calculations of nanoscale CdSe quantum dots. *Phys. Rev. B* **1996,** *53* (15), 9579-9582. DOI: 10.1103/PhysRevB.53.9579.

45. Wang, L.-W.; Zunger, A., Local-density-derived semiempirical pseudopotentials. *Phys. Rev. B* **1995,** *51* (24), 17398-17416. DOI: 10.1103/PhysRevB.51.17398.

46. Enright, M. J.; Jasrasaria, D.; Hanchard, M. M.; Needell, D. R.; Phelan, M. E.; Weinberg, D.; McDowell, B. E.; Hsiao, H.-W.; Akbari, H.; Kottwitz, M.; Potter, M. M.; Wong, J.; Zuo, J.-M.; Atwater, H. A.; Rabani, E.; Nuzzo, R. G., Role of Atomic Structure on Exciton Dynamics and Photoluminescence in NIR Emissive InAs/InP/ZnSe Quantum Dots. *J. Phys. Chem. C* **2022,** *126* (17), 7576-7587. DOI: 10.1021/acs.jpcc.2c01499.

47. Rabani, E.; Hetényi, B.; Berne, B. J.; Brus, L. E., Electronic properties of CdSe nanocrystals in the absence and presence of a dielectric medium. *J. Chem. Phys.* **1999,** *110* (11), 5355-5369. DOI: 10.1063/1.478431.

48. Eshet, H.; Grünwald, M.; Rabani, E., The Electronic Structure of CdSe/CdS Core/Shell Seeded Nanorods: Type-I or Quasi-Type-II? *Nano Lett.* **2013,** *13* (12), 5880-5885. DOI: 10.1021/nl402722n.

49. Rohlfing, M.; Louie, S. G., Electron-hole excitations and optical spectra from first principles. *Phys. Rev. B* **2000,** *62* (8), 4927-4944. DOI: 10.1103/PhysRevB.62.4927.

50. Jasrasaria, D.; Weinberg, D.; Philbin, J. P.; Rabani, E., Simulations of nonradiative processes in semiconductor nanocrystals. *J. Chem. Phys.* **2022,** *157* (2), 020901. DOI: 10.1063/5.0095897.

51. Powell, D.; Migliorato, M. A.; Cullis, A. G., Optimized Tersoff potential parameters for tetrahedrally bonded III-V semiconductors. *Phys. Rev. B* **2007,** *75* (11), 115202. DOI: 10.1103/PhysRevB.75.115202.

52. Klimov, V. I., Optical Nonlinearities and Ultrafast Carrier Dynamics in Semiconductor Nanocrystals. *J. Phys. Chem. B* **2000,** *104* (26), 6112-6123. DOI: 10.1021/jp9944132.

53. Mourad, D.; Guille, A.; Aubert, T.; Brainis, E.; Hens, Z., Random-Alloying Induced Signatures in the Absorption Spectra of Colloidal Quantum Dots. *Chem. Mater.* **2014,** *26* (23), 6852-6862. DOI: 10.1021/cm5035408.

54. Mlinar, V.; Zunger, A., Effect of atomic-scale randomness on the optical polarization of semiconductor quantum dots. *Phys. Rev. B* **2009,** *79* (11), 115416. DOI: 10.1103/PhysRevB.79.115416.

55. Corney, A., The spontaneous radiation of emission. In *Atomic and Laser Spectroscopy*, Clarendon Press, Oxford: Great Britain, 1978; pp 93-115.

56. Jasieniak, J.; Smith, L.; van Embden, J.; Mulvaney, P.; Califano, M., Re-examination of the Size-Dependent Absorption Properties of CdSe Quantum Dots. *J. Phys. Chem. C* **2009,** *113* (45), 19468-19474. DOI: 10.1021/jp906827m.

57. Makuła, P.; Pacia, M.; Macyk, W., How To Correctly Determine the Band Gap Energy of Modified Semiconductor Photocatalysts Based on UV–Vis Spectra. *J. Phys. Chem. Lett.* **2018,** *9* (23), 6814-6817. DOI: 10.1021/acs.jpclett.8b02892.

58. Jasrasaria, D.; Philbin, J. P.; Yan, C.; Weinberg, D.; Alivisatos, A. P.; Rabani, E., Sub-Bandgap Photoinduced Transient Absorption Features in CdSe Nanostructures: The Role of Trapped Holes. *J. Phys. Chem. C* **2020,** *124* (31), 17372-17378. DOI: 10.1021/acs.jpcc.0c04746.

59. Makarov, N. S.; Guo, S.; Isaienko, O.; Liu, W.; Robel, I.; Klimov, V. I., Spectral and Dynamical Properties of Single Excitons, Biexcitons, and Trions in Cesium–Lead-Halide Perovskite Quantum Dots. *Nano Lett.* **2016,** *16* (4), 2349-2362. DOI: 10.1021/acs.nanolett.5b05077.

60. Chen, Y.; Vela, J.; Htoon, H.; Casson, J. L.; Werder, D. J.; Bussian, D. A.; Klimov, V. I.; Hollingsworth, J. A., "Giant" Multishell CdSe Nanocrystal Quantum Dots with Suppressed Blinking. *J. Am. Chem. Soc.* **2008,** *130* (15), 5026-5027. DOI: 10.1021/ja711379k.

61. Cragg, G. E.; Efros, A. L., Suppression of Auger Processes in Confined Structures. *Nano Lett.* **2010,** *10* (1), 313-317. DOI: 10.1021/nl903592h.

62. Varshni, Y. P., Temperature dependence of the energy gap in semiconductors. *Physica* **1967,** *34* (1), 149-154. DOI: 10.1016/0031-8914(67)90062-6.

63. Rowland, C. E.; Liu, W.; Hannah, D. C.; Chan, M. K. Y.; Talapin, D. V.; Schaller, R. D., Thermal Stability of Colloidal InP Nanocrystals: Small Inorganic Ligands Boost High-Temperature Photoluminescence. *ACS Nano* **2014,** *8* (1), 977-985. DOI: 10.1021/nn405811p.

64. Zhao, Y.; Riemersma, C.; Pietra, F.; Koole, R.; de Mello Donegá, C.; Meijerink, A., High-Temperature Luminescence Quenching of Colloidal Quantum Dots. *ACS Nano* **2012,** *6* (10), 9058-9067. DOI: 10.1021/nn303217q.

65. Rowland, C. E.; Fedin, I.; Diroll, B. T.; Liu, Y.; Talapin, D. V.; Schaller, R. D., Elevated Temperature Photophysical Properties and Morphological Stability of CdSe and CdSe/CdS Nanoplatelets. *J. Phys. Chem. Lett.* **2018,** *9* (2), 286-293. DOI: 10.1021/acs.jpclett.7b02793.

66. Porter, V. J.; Geyer, S.; Halpert, J. E.; Kastner, M. A.; Bawendi, M. G., Photoconduction in Annealed and Chemically Treated CdSe/ZnS Inorganic Nanocrystal Films. *J. Phys. Chem. C* **2008,** *112* (7), 2308-2316. DOI: 10.1021/jp710173q.

67. Talapin, D. V.; Lee, J.-S.; Kovalenko, M. V.; Shevchenko, E. V., Prospects of Colloidal Nanocrystals for Electronic and Optoelectronic Applications. *Chem. Rev.* **2010,** *110* (1), 389-458. DOI: 10.1021/cr900137k.

68. Levinshtein, M.; Rumyantsev, S.; Shur, M., Handbook Series on Semiconductor Parameters. World Scientific: London, 1996; Vol. 1, pp 169-190.

4. $In_{1-x}Ga_xP$ Nanocrystals Synthesized in Molten Salts as Stable Blue Emitters

4.1. Introduction to molten-salt synthesized $In_{1-x}Ga_xP$ nanocrystals as stable blue emitters.

Among colloidal semiconductor nanocrystals that emit within the visible spectral range, cadmium selenide (CdSe)-based systems, belonging to the II-VI class of binary semiconductors, have been most extensively studied and optimized.[1-4] Only recently the research community has dedicated significant efforts to develop Cd-free, non-toxic alternatives for use in consumer electronics. In this context, InP-based III-V colloidal quantum dots (CQDs) have emerged as promising candidates. Most optimized methods for synthesizing InP nanocrystals involve the continuous injection of pre-formed InP clusters, resulting in minimal size variations, thereby reducing emission linewidth.[5] Synthesis of highly luminescent InP nanocrystals typically involves the sequential growth of multiple shells to effectively isolate charge carriers from surface trap states, while fine-tuning the band alignment and reducing lattice mismatch at the core-shell interface.[6-7] These strategies have successfully yielded red[8] and green-emitting[9] InP/ZnSe/ZnS nanocrystals with PLQYs exceeding 95%, narrow emission linewidths, and near-optimal device external quantum efficiency (EQE). However, the challenge lies in achieving blue emission, which requires InP nanocrystals to be as small as 1.5 nm according to the sizing curve based on confinement effects.[10-11] Such minuscule sizes are inherently unstable and prone to detrimental non-radiative processes, such as rapid Auger recombination. The associated synthetic difficulties have forced the research community to resort to sub-optimal synthetic strategies, such as surface etching[12-13] or aliovalent doping of larger pre-formed InP nanocrystals with Zn^{2+} or Cu^{2+} cations to achieve blue emission.[6, 14-15] As a result, stable blue emission with a high device external quantum efficiency (EQE) from Cd-free nanocrystals has mostly remained limited to II-VI semiconductors, such as ZnSe(Te)-based materials.[16, 17]

III–V compound semiconductors stand as the material of choice for a myriad of electronic and optoelectronic applications, encompassing high-performance transistors,[18-20] efficient photovoltaic cells,[21-23] and light-emitting diodes (LEDs).[24] The evolution of epitaxial growth techniques, such as molecular beam epitaxy,[25] metal-organic chemical vapor deposition (MOCVD),[26] and pulsed laser deposition[27] have facilitated the growth of single-crystalline III–V thin films tailored for various device applications. Unfortunately, the achievements in this realm have not yet extended to the domain of solution-processable III-V nanocrystals. The III-V bonds are predominantly covalent and rigid, making it difficult to achieve microscopic reversibility for defect-free crystal growth, except at elevated temperatures inaccessible to traditional organic solvents.[28] Molten inorganic salts serve as robust, high-temperature solvents with an expansive electrochemical window, making them inert matrices suitable for a variety of chemical processes.[29] The unique chemical interactions between the NC surfaces and the molten salt matrix induce a structural reconfiguration of the molten salt ion template surrounding the NCs. This effectively forms a protective barrier that prevents direct contact between the NC surfaces, safeguarding them against undesirable sintering, even at elevated temperatures.[30] This distinctive environment proves highly conducive to synthetic transformations involving III-V nanocrystals.

In our recent work, our group successfully synthesized ternary III–V phases of $In_{1-x}Ga_xP$ nanocrystals from InP by subjecting them to high-temperature annealing in a molten salt mixture of gallium-containing salts.[31] In their bulk form, GaP, an indirect-band-gap semiconductor (E_g = 2.26 eV),[32] possesses a larger bandgap than InP, a direct-band-gap semiconductor (E_g = 1.34 eV).[33] Consequently, alloying InP nanocrystals with GaP produces ternary III-P phases with a larger bandgap and bluer emission while maintaining a larger size. Notably, at approximately 75% gallium content in the bulk the conduction band's Γ and X valleys cross in energy, causing In_{1-}

$_xGa_xP$ to exhibit indirect behavior at higher gallium contents.[32, 34] We observed a similar transition in their quantum-confined counterpart $In_{1-x}Ga_xP$ nanocrystals, characterized by a decreased oscillator strength of excitonic transitions above a certain gallium content.[35] Our findings suggest that incorporating more gallium in $In_{1-x}Ga_xP$/ZnS colloidal nanocrystals can only be a part of the strategy for achieving blue III-P emitters. We must instead strike a balance between the nanocrystal size and gallium composition to yield blue emission from $In_{1-x}Ga_xP$ while preserving the oscillator strength of direct-like Γ-to-Γ valley interband excitonic transitions.

In this work we expand upon these design principles and apply them to a population of small InP nanocrystals. We perform In-to-Ga cation exchange reaction in a reduced $Ga^{(I)}Ga^{(III)}I_4$ (nominally Ga_2I_4) molten salt medium under carefully tuned annealing conditions to produce alloyed $In_{1-x}Ga_xP$ nanocrystals with a moderate gallium content. GaP alloying results in a larger bandgap and also reduces the lattice mismatch at the core-shell interface with wide bandgap shelling materials such as zinc sulfide (ZnS). We further describe a rigorously oxygen-free shelling protocol to grow a relatively thick highly crystalline ZnS shell on the $In_{1-x}Ga_xP$ cores to achieve efficient surface passivation. This in turn, yields bright and color-pure blue emission at 470 nm, with a narrow emission linewidth of 38 nm, and ~40% emission quantum yield. We demonstrate that the high-temperature PLQY attrition and recovery behavior of the blue-emitting $In_{1-x}Ga_xP$/ZnS core-shell sample is similar to its heavily optimized green-emitting InP counterpart with a similar core size.

4.2. Synthesis of small InP nanocrystals and In-to-Ga cation exchange.

Similar to the direct-to-indirect crossover in bulk $In_{1-x}Ga_xP$ at ~75% gallium content, we have established empirically and through calculations that there is a similar but gradual transition in their quantum-confined counterpart $In_{1-x}Ga_xP$ nanocrystals, characterized by a decreased oscillator

strength of excitonic transitions above ~65% gallium content.[35] Here, we explore a synthetic strategy utilizing smaller nanocrystals and limiting to moderate gallium compositions to yield blue emission from $In_{1-x}Ga_xP$ while preserving the oscillator strength of direct-like Γ-to-Γ valley interband excitonic transitions.

The selection of a suitable precursor offers one of the most accessible handles for tuning the size of InP nanocrystals synthesized in colloidal organic phases. Most optimized InP syntheses with narrow resultant size distributions, utilize *in situ* formed indium carboxylates as the indium precursor. Given a similar indium to phosphorous ratio, a longer chain carboxylic acid is known to yield smaller nanocrystals under otherwise similar reaction conditions.[36-37] We reproduced this result by synthesizing InP nanocrystals using indium laurate, myristate and palmitate precursors.

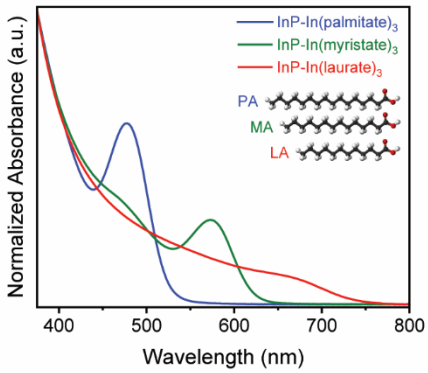

Figure 4.1. Dependence of InP nanocrystal size on the choice of indium carboxylate precursor.

As noted in Figure 4.1, carboxylate precursors with a smaller hydrocarbon chain yield larger nanocrystals, characterized by an absorption feature at a longer wavelength. We adapted the synthesis of small InP nanocrystals from an established reaction between indium palmitate and tris(trimethylsilyl)phosphine as the indium and phosphorous precursors, respectively.[7] The absorption spectrum shows an excitonic feature at 465 nm and a Stokes shifted emission peak at 515 nm (Figure 4.2A). The photoluminescence is dominated by surface trap state emission, owing

to the large surface to volume ratio and lack of surface passivation. PXRD indicates that the crystalline phase is zinc blende, and the broad diffraction peaks indicate that the nanocrystalline domains are indeed small (Figure 4.4D). Scherrer analysis estimates the particles' diameter at ~1.8 nm. In order to better estimate the size of the nanocrystals, we perform small angle X-ray scattering, and estimate the average particle diameter at 2.5 nm from a volume-scaled size distribution obtained from a maximum entropy fit (Figure 4.3A-B).

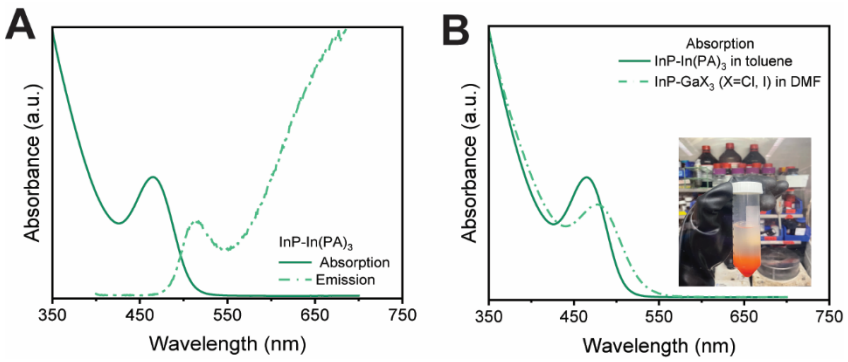

Figure 4.2. Optical characterization of InP nanocrystals before and after Z-type ligand exchange. (A) Absorption and emission spectra of the starting InP nanocrystals synthesized from indium palmitate and tris(trimethylsilyl)phosphine. The native organic X-type ligands were exchanged with inorganic Z-type gallium halide ligands. (B) Absorption spectrum of the ligand-exchanged nanocrystals dispersed in DMF. The photograph shows that the nanocrystals transfer to the DMF phase after ligand exchange.

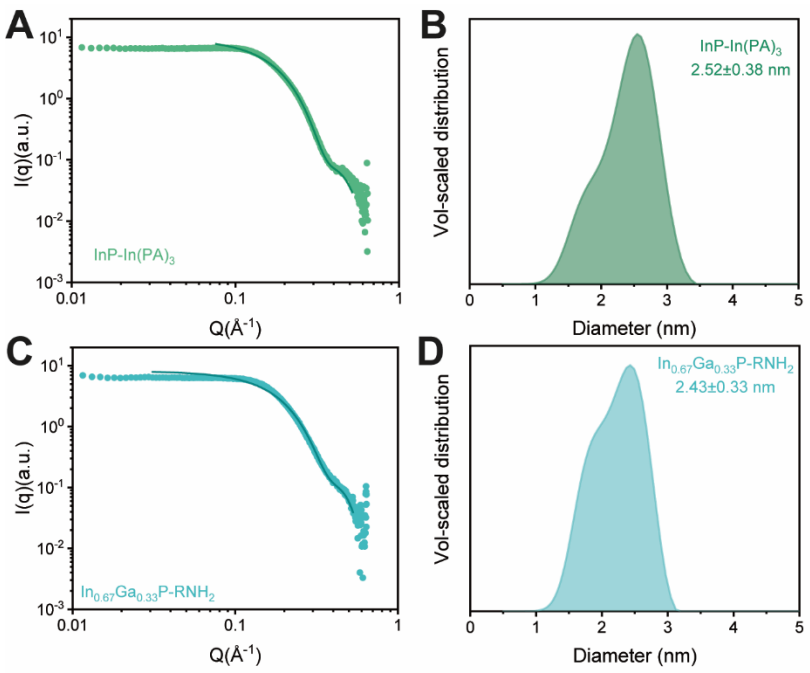

Figure 4.3. Size analysis: small-angle X-ray scattering (SAXS) data and maximum-entropy fits. For (A) small InP QDs with indium palmitate surface passivation, and (C) alloyed $In_{1-x}Ga_xP$ QDs recovered with alkylamine ligands. (B) and (D) respectively are volume-scaled size distributions of the same obtained from maximum entropy fits to the SAXS data.

The next step is to perform In-to-Ga cation exchange to yield alloyed $In_{1-x}Ga_xP$ nanocrystals. The as-synthesized organically capped nanocrystals are not compatible with the heavily ionized molten salt reaction media. We exchanged the X-type long-chain organic ligands with compact Z-type inorganic ligands, specifically gallium halides (gallium chloride and gallium iodide), to be able to disperse them in the molten salt matrix. This chalcogenide-free approach was recently developed in our group to avoid installing a large number of heteroatoms onto the surface of small nanocrystals with a large surface to volume ratio.[38-39] The ligand exchanged particles form a stable colloidal dispersion in DMF that could be characterized optically via absorption spectroscopy (Figure 4.2B). Surface ligands are known to affect the energy states of a nanocrystal in a non-trivial fashion,[40-41] and the subtle changes in the shape of the absorption feature before and after ligand exchange may not be indicative of any surface etching processes.

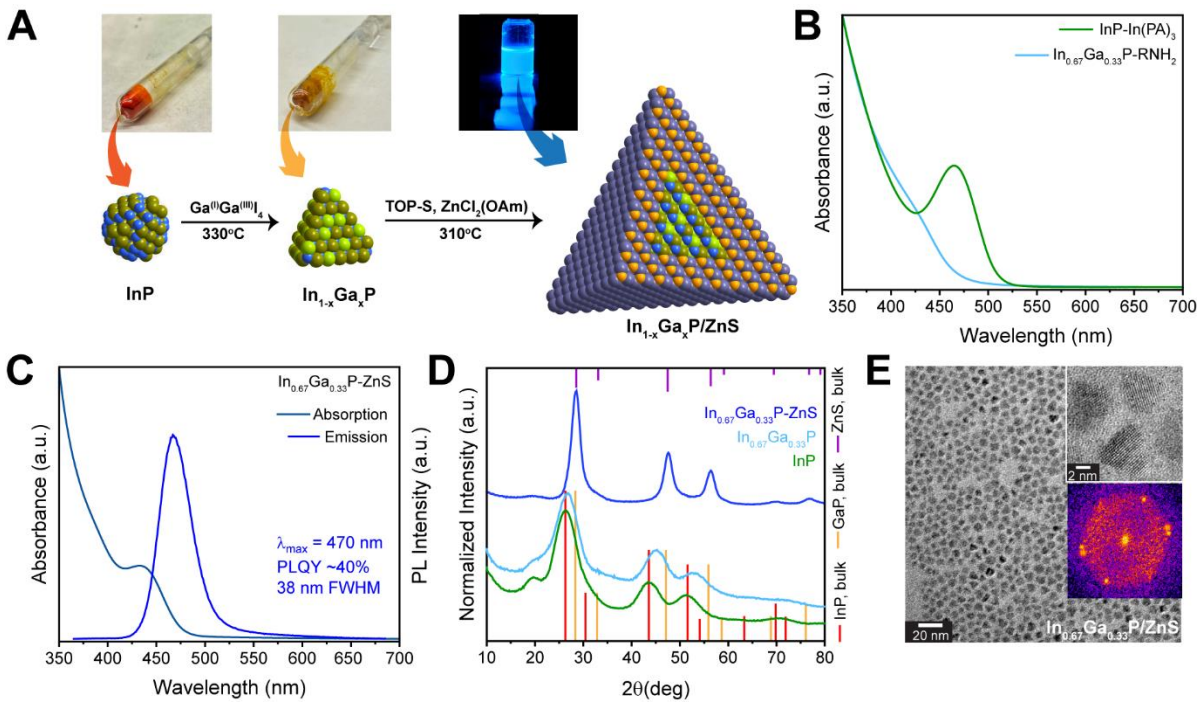

Figure 4.4. Optical and structural characterization of the small InP, alloyed $In_{1-x}Ga_xP$ and core-shell $In_{1-x}Ga_xP/ZnS$ colloidal nanocrystals.

(A) Reaction scheme indicating the cation exchange and subsequent ZnS shelling conditions. Photos of the nanocrystals dispersed in the molten salt reaction medium sealed inside a quartz ampoule before and after annealing, along with a photo of the bright blue emitting core-shell sample dispersed in hexane under UV illumination, are included. (B) Absorption spectra of the InP and $In_{1-x}Ga_xP$ nanocrystals indicate a blue shift in the excitonic feature following In-to-Ga cation exchange. (C) Absorption and emission spectra of the core-shell $In_{1-x}Ga_xP/ZnS$ sample. (D) Powder X-ray Diffraction patterns of the core-only and core-shell samples. (E) TEM images of the core-shell $In_{1-x}Ga_xP/ZnS$ nanocrystals show faceted single crystalline domains, with ~9 nm tetrahedral edge length. Lattice fringes are clearly visible in the high-resolution micrograph.

The ligand exchanged particles were dried, incorporated into a reduced $Ga^{(I)}Ga^{(III)}I_4$ molten salt matrix, and annealed at 300°C and 330°C for an hour each while sealed inside a quartz ampoule. A reaction scheme along with photos nanocrystals dispersed in the salt matrix before and after annealing, are included in Figure 4.4A. The most common decomposition pathway for Indium Pnictide phases is oxidative, and the reduced gallium iodide salt ensures a reducing environment is maintained during the annealing step to prevent decomposition. The In-to-Ga cation exchange

increases the optical bandgap, characterized by a blue shift of the absorption feature as demonstrated in Figure 4.4B. X-ray diffraction peaks of the alloyed nanocrystals are shifted toward higher 2θ values indicating gallium incorporation. The pattern is that of a pure zinc blende phase, with no obvious signs of decomposition. The crystalline domains are small, therefore the diffraction peaks are broad (Figure 4.4D). We estimate gallium composition from the 2θ positions of the diffraction peaks through linear interpolation using the bulk lattice constants of InP and GaP (Vegard's law). As a fraction of the total metal content, we estimate the gallium composition of the $In_{1-x}Ga_xP$ core at 33%, although the diffuse diffraction pattern makes the linear interpolation method somewhat unreliable. We estimate the average diameter of the alloyed $In_{1-x}Ga_xP$ nanocrystals thus synthesized, at ~2.5 nm as well via SAXS (Figure 4.3 B, D), indicating any surface etching effects occurring during the cation exchange step are negligible.

We next passivated the surface of the $In_{1-x}Ga_xP$ nanocrystals by overgrowing a ZnS shell on the core. The growth of a crystalline ZnS phase is usually performed at temperatures of around 300^oC or higher to prevent the accumulation of defects. However, gallium has a large affinity towards oxygen at elevated temperatures, requiring that we use oxygen-free shelling precursors at this step to prevent substantial surface oxidation. A HF surface treatment of the InP core to remove residual oxides has previously been shown to be instrumental in achieveing a high PLQY in the heavily optimized InP/ZnSe/ZnS core/shell/shell heterostructures.[8] We decided to adapt an anhydrous version of this step by treating the nanocrystals with GaF_3 in the presence of oleylamine at 120^oC before the addition of any shelling precursors. Next, we introduced the zinc and sulfur precursors in five separate steps at the growth temperature of 310^oC to prevent secondary nucleation of ZnS domains. We tracked the evolution of the absorption and emission features of the nanocrystals during shell growth by withdrawing aliquots every 30 min, before each addition of the zinc

precursor (Figure 4.5). The PLQY steadily increases over the course of shell growth up to this point, but any further addition of precursors lead to a sharp decrease in the PLQY accompanied by a noticeable red shift and broadening of the emission peak.

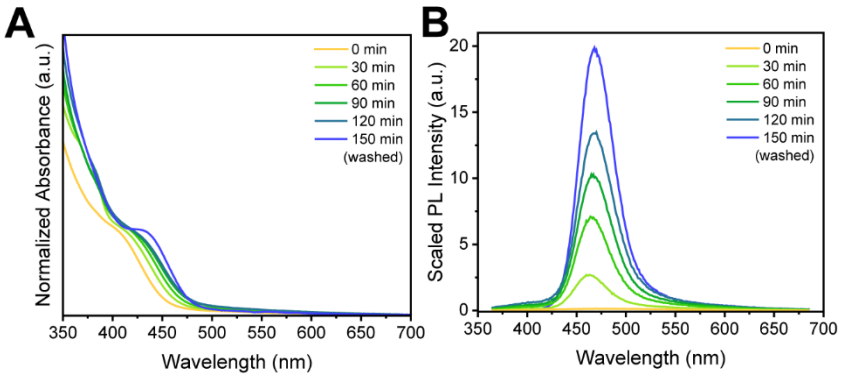

Figure 4.5. Optical characterization of aliquots withdrawn during ZnS shell growth.
The evolution of the (A) absorption and (B) photoluminescence emission spectra during shell growth were tracked by withdrawing aliquots at every 30 min. The PL spectra are scaled using the absorbance value at the excitation wavelength of 350 nm.

The final core-shell sample emits in the blue region of the visible spectrum, with an emission peak λ_{max} = 470 nm and a narrow emission linewidth of 38 nm (Figure 4.4C). The photograph taken under UV irradiation and included with the reaction scheme in Figure 4.4A visually corroborates the blue emission. We measured the (absolute) photoluminescence quantum yield of the core-shell sample at 40% using an integrating sphere (Figure 4.6).

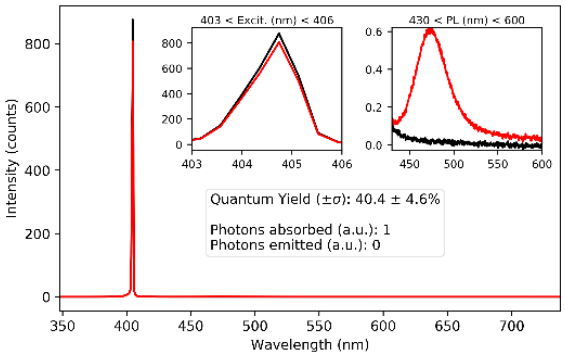

Figure 4.6. Absolute PL quantum yield of the blue-emitting core-shell $In_{1-x}Ga_xP/ZnS$ sample. In hexane, measured using an integrating sphere and a 405 nm laser excitation source.

The extent of inhomogeneous broadening of the emission peak can be roughly estimated from the eccentricity of the excitonic feature along the diagonal in an excitation-emission map. The excitation-emission map of the core-shell $In_{1-x}Ga_xP/ZnS$ sample in Figure 4.7 demonstrates little diagonal broadening, indicating limited population dispersity and alloying inhomogeneity in these samples, which are major contributors toward inhomogeneous broadening.

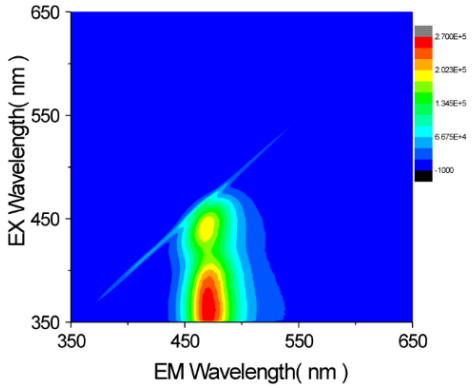

Figure 4.7. Excitation-emission map of the blue-emitting core-shell $In_{1-x}Ga_xP/ZnS$ sample.

The diffraction pattern of the core-shell $In_{1-x}Ga_xP/ZnS$ sample in Figure 4.4D almost matches that of a zinc blende ZnS phase, with the significantly narrowed peaks clearly indicating extended crystalline domains. We thus ascertain the growth of a thick zinc sulfide shell. A TEM image of

the core-shell sample is included in Figure 4.4E. The nanocrystals show faceted single crystalline domains with minimal size polydispersity, with ~9 nm tetrahedral edge length on average. Lattice fringes are clearly visible in the associated high-resolution micrograph, implying the core-shell particles are good quality and highly crystalline. We estimate the ZnS shell to be 6 monolayers / 1.6 nm thick from the TEM data. We further perform X-ray Fluorescence based elemental analysis on the core-only and core-shell samples. We estimate the Ga-to-In ratio to be ~3:1 from XRF, which is about 40% higher than the PXRD based estimate. We have also observed this discrepancy between elemental analysis and diffraction-based estimates of Ga contents in the past, and have ascribed it to the presence of additional Ga-containing moieties (likely GaI_3 as a Z-type ligand) at the nanocrystal surface that were not incorporated into the crystalline domain, and therefore, do not affect the positions of the diffraction peaks.[38] As a surface effect, this discrepancy is more pronounced in such small nanocrystals with a large surface-to-volume ratio. We record a Ga-to-In ratio of ~3.3 in the core-shell sample, thereby corroborating the retention of gallium in the alloyed core over the course of shell growth. The increase in gallium content is likely related to the GaF_3

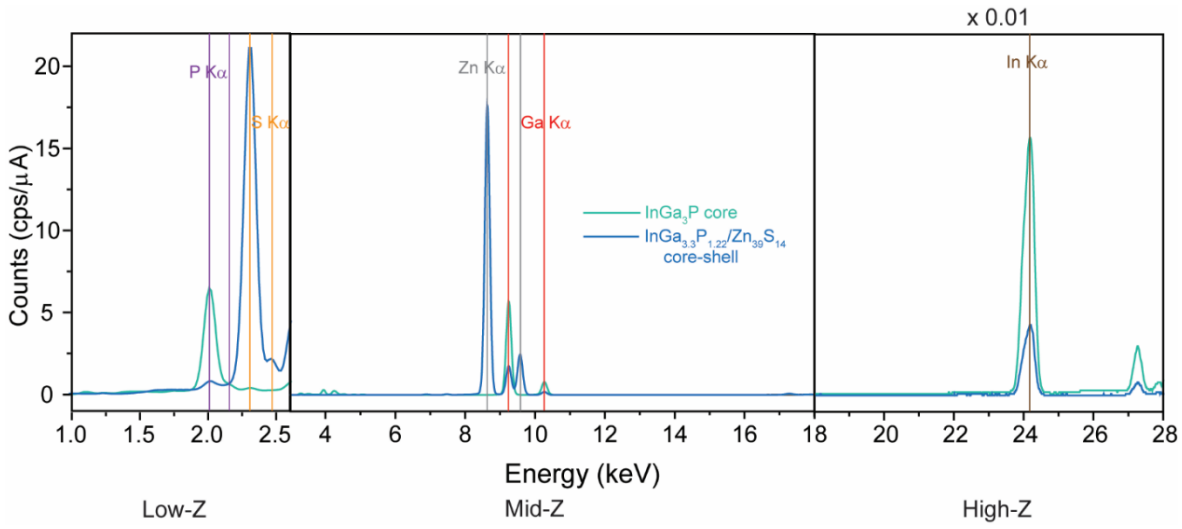

Figure 4.8. XRF elemental analysis of the core and core-shell.

surface treatment of the core during shell growth. The large Zn to (In+Ga) ratio further points to the presence of a thick ZnS shell on the relatively small $In_{1-x}Ga_xP$ core.

In this and previous works, we have emphasized the importance of a rigorously oxygen-free shell growth recipe for Ga-containing III-V phases due to the very high oxophilicity of gallium at elevated temperatures. We can probe that by the addition of a usual oxygen-containing zinc precursor, zinc oleate, to the core-shell $In_{1-x}Ga_xP/ZnS$ nanocrystals and probe changes in the emission. We dissolved a 2:1 stoichiometric mixture of oleic acid and $ZnCl_2$ in 1-octadecene (ODE) under inert conditions and degassed the reaction mixture under vacuum at 120^oC for an hour to yield a 0.2(M) solution of zinc oleate in ODE. We recorded the steady-state PL spectrum of a nanomolar solution of the core-shell $In_{1-x}Ga_xP/ZnS$ colloidal nanocrystals in hexane, and then added $2x10^{-6}$ mol of zinc oleate to the cuvette under inert conditions. As demonstrated in Figure 4.9, we see an immediate decrease in PLQY after the addition of zinc oleate, and some further decrease in more time, when the solution was allowed to rest. The emission spectra are scaled by sample absorbance at the excitation wavelength of 350 nm to account for small changes in concentration.

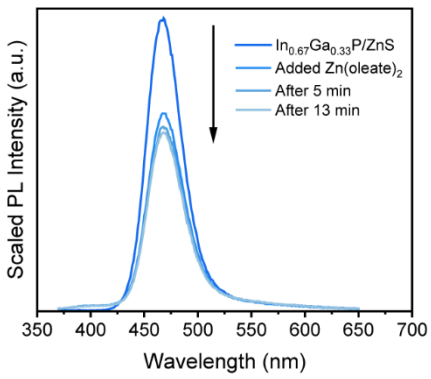

Figure 4.9. Decrease in PLQY due to the addition of zinc oleate.

Interestingly, this effect was observed in core-shell nanocrystals with a thick ZnS shell, which we plan to probe further.

4.3. Time-resolved spectroscopy.

Time-resolved photoluminescence (trPL) studies convey important information regarding exciton dynamics and radiative PL decay pathways. We record trPL decay profile at the emission maximum of 470 nm using a 405 nm excitation source. The decay can be modeled as a biexponential, with a time constant of 61 ns for the majority decay pathway, likely radiative (Figure 4.10). The long decay lifetime is consistent with a high-quality core-shell sample with efficient surface passivation. We are working on complementing this data with transient absorption studies and fluence dependent carrier dynamics to develop a comprehensive understanding of the optoelectronic behavior of this exciting sample.

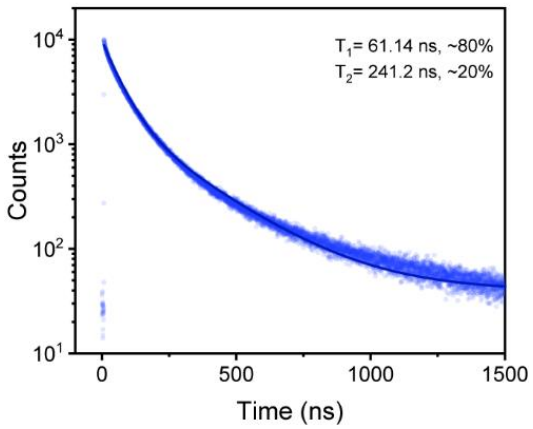

Figure 4.10. Time-resolved PL decay of the blue-emitting core-shell $In_{1-x}Ga_xP/ZnS$ colloidal nanocrystals.

4.4. High-temperature behavior of photoluminescence.

We examined the emission behavior of the blue-emitting colloidal core-shell $In_{1-x}Ga_xP/ZnS$ sample at elevated temperatures using a custom-built setup. This setup, illustrated in Figure 4.12A, utilizes a dilute solution of the colloidal nanocrystals in 1-octadecene sealed inside a quartz ampoule using an oxy-hydrogen torch. We excited the NCs with a 405 nm laser and recorded their PL spectra using a fiber-coupled spectrophotometer positioned perpendicular to the excitation source. To control the temperature, we placed the sealed ampoule in a heating block. This experimentation is relevant in scenarios where emissive materials are subjected to thermal cycling, such as in on-chip color converters in LEDs or electroluminescent devices. We usually observe a decrease in photoluminescence quantum yield (PLQY) of colloidal nanocrystals at higher temperatures, commonly explained by thermally activated trapping of photoexcited carriers.[42-44] On the other hand, an unrecoverable drop in PLQY post annealing, known as PL attrition, is often explained by irreversible loss of ligands from the nanocrystal surface as temperatures rise.[45-46] Minimal PLQY drops and temperature-related color shifts are crucial for preserving a consistent display color range and brightness in optoelectronic devices that employ nanocrystals as emitters.

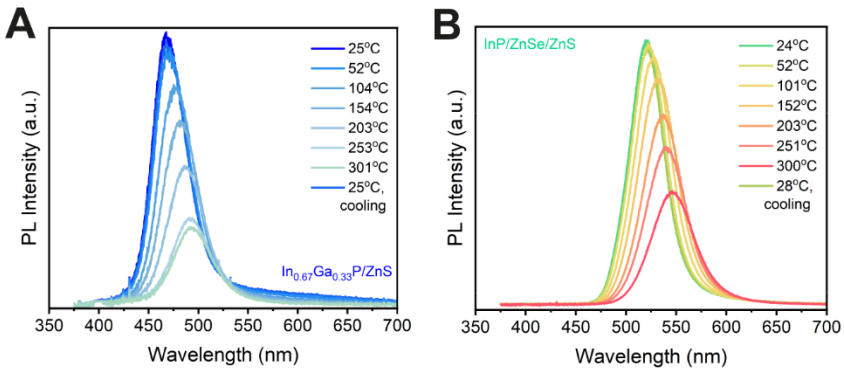

Figure 4.11. High-temperature PL spectra of $In_{1-x}Ga_xP/ZnS$ and InP/ZnSe/ZnS nanocrystals with a similar core size plotted against wavelength axes.

In Figure 4.11 we compare the photoluminescence behavior of the blue-emitting core-shell $In_{1-x}Ga_xP/ZnS$ sample between room temperature and 300°C/573K with a heavily optimized InP/ZnSe/ZnS sample with a similar core size, procured from proprietary sources. We further transform these emission spectra with the Jacobian correction factor and plot them against energy axes in Figures 4.12 B and C to subsequently extract their optical bandgap (Figure 4.12F).

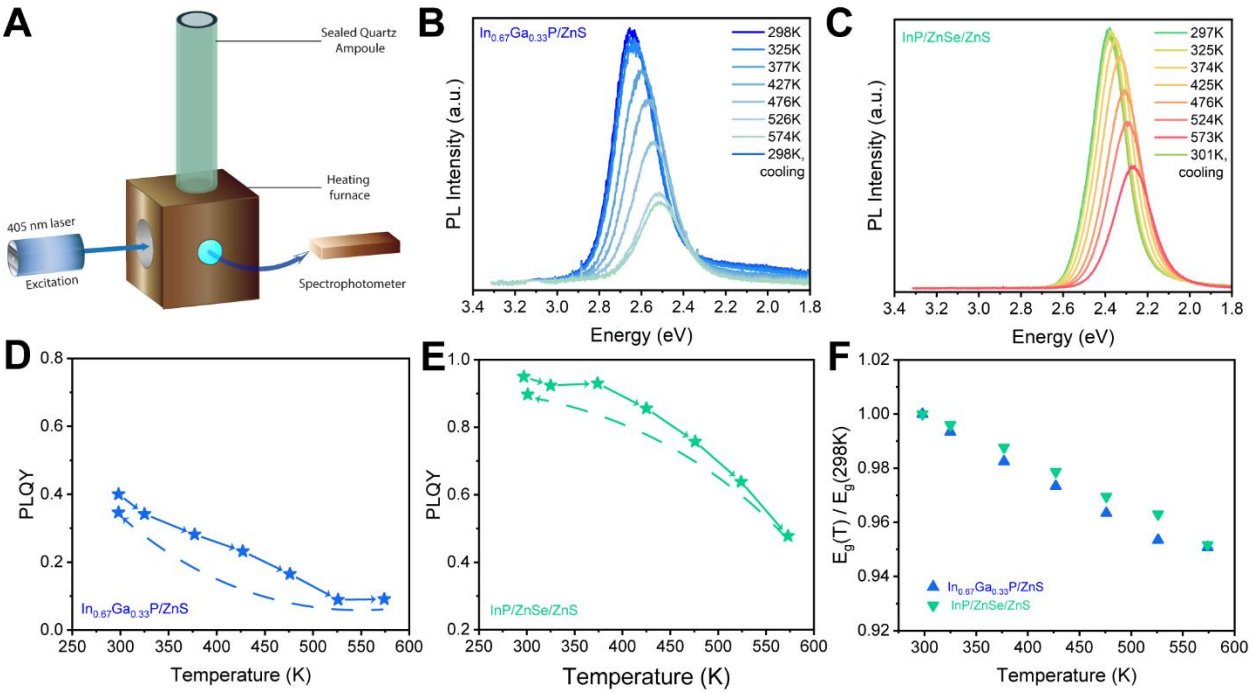

Figure 4.12. Photoluminescence behavior at elevated temperatures.
(A) Schematic of the setup utilized for investigating the PL behavior of bright $In_{1-x}Ga_xP/ZnS$ and InP/ZnSe/ZnS NCs of comparable core size, at elevated temperatures. The emission spectra for the same in energy axes, are plotted in (B) and (C) respectively as a function of temperature. Fractional changes in the integrated PL intensity of the samples were used to estimate the drop in PLQY with temperature in the plots (D) and (E). (F) Dependence of optical bandgap on temperature (scaled to the room-temperature bandgap) exhibits similar linear trends.

We determined the photoluminescence quantum yield (PLQY) of emissive samples at higher temperatures by comparing the integrated PL intensities measured under similar conditions at both ambient and elevated temperatures. After annealing, the samples were allowed to cool back down to room temperature, and we recorded PL spectra again in order to estimate the irreversible PL

attrition. The trends in PLQY are scaled to the room temperature PLQY and summarized in Figure 4.12D and E for clarity. The room temperature PLQY of the heavily optimized InP/ZnSe/ZnS sample obtained from proprietary sources, was estimated to be 95% from a prior report.[9] Notedly, the decline in PLQY of both the samples has a very similar dependence on temperature, and the PLQY recovery after cooling is near perfect in both cases. Sustained interfacial strain at the core-shell boundary has been noted as one of the main causes of irreversible PLQY attrition as it enhances defect mobility. This experiment demonstrates impressive high temperature performance of the blue-emitting core-shell $In_{1-x}Ga_xP$/ZnS NCs with a relatively thick ZnS shell. We ascribe this to a decreased lattice mismatch at the core-shell interface owing to the In-to-Ga cation exchange.

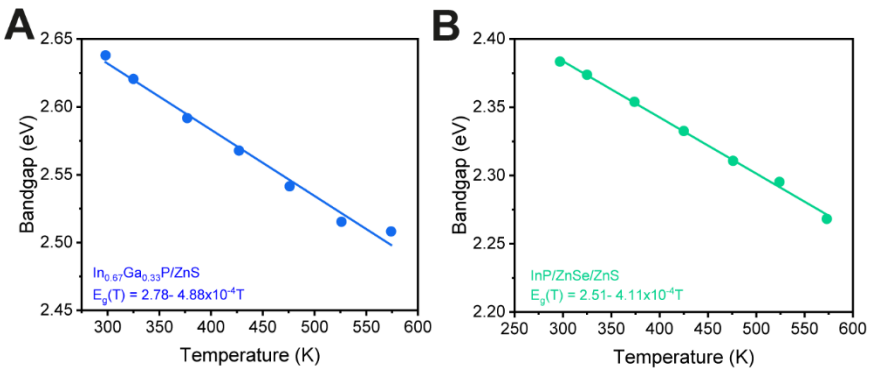

Figure 4.13. Varshni plot to describe temperature dependence of the optical bandgap.

Temperature dependence of the optical bandgap can be assumed to be linear under a first order high-temperature approximation of the semi-empirical Varshni relation, $E_g(T) = E_g(296K) - \alpha T$. At higher temperatures, lattice expansion causes a decrease in the direct bandgap between the Γ-valley of the conduction band and the top of the valence band. This is clearly demonstrated in the Varshni plot associated with the data for both samples, in Figure 4.13. To compare their temperature dependence, we normalize the bandgaps of the $In_{1-x}Ga_xP$/ZnS and InP/ZnSe/ZnS

samples by their room temperature counterparts and compare the slope of the linear relations in Figure 4.12F. The linear fits indicate that the temperature dependence is similar for both samples, and the blue-emitting sample is able to retain its emission color range reasonably well under thermal cycling conditions.

4.5. Conclusions.

To summarize, we start with small InP nanocrystals and perform In-to-Ga cation exchange in a reduced $Ga^{(I)}Ga^{(III)}I_4$ molten salt reaction medium to yield small alloyed $In_{1-x}Ga_xP$ nanocrystals. We achieve effective surface passivation by growing a highly crystalline 6 monolayer thick ZnS shell on the $In_{1-x}Ga_xP$ core under rigorously oxygen-free conditions to yield bright and color pure blue emission at 470 nm with 40% PLQY and a narrow emission linewidth of 38 nm. Residual strain at the core-shell interface is alleviated by a better lattice match with the In-to-Ga cation exchanged nanocrystals, allowing us to grow the thick ZnS shell. A thick shell of a wide bandgap material may efficiently localize excitons in the $In_{1-x}Ga_xP$ core by imposing a large potential barrier, thereby preventing fast FRET pathways leading to reddened emission in electroluminescent devices. This work demonstrates a carefully tuned synthetic strategy by striking a balance between the nanocrystal size and gallium composition in order to achieve bright blue emission from $In_{1-x}Ga_xP$ while maintaining the oscillator strength of direct-like Γ-to-Γ valley interband excitonic transitions.

4.6 Materials and methods.

Chemicals. Trioctylphosphine (TOP, 97%), palmitic acid (PA, 99%), sulfur (99.998%), gallium metal (99.99%) and anhydrous solvents (hexane, toluene, ethanol (EtOH), methyl acetate, isopropanol (IPA), acetonitrile (MeCN)) were purchased from Sigma Aldrich and used as

received. Oleylamine (OAm, technical grade, 70%) was purchased from Sigma Aldrich and purified by freezing, thawing, and then centrifuging to remove any insoluble solids. The resulting purified oleylamine was dried under dynamic vacuum at 100^{o}C overnight and stored in a nitrogen glovebox. 1-Octadecene (ODE, 90%) was purchased from Sigma Aldrich, dried under dynamic vacuum at 80^{o}C overnight and stored in a nitrogen glovebox. Dodecylamine (98%) and octadecylamine (technical grade, 90%) were purchased from Sigma Aldrich and dried under dynamic vacuum before storage in a nitrogen glovebox. Gallium(iii) iodide (ultra-dry, 99.999%), indium(iii) acetate (99.99%), zinc chloride (ultra-dry, 99.999%), gallium fluoride (99.995%) and N,N-dimethylformamide (DMF, anhydrous 99.9%) were purchased from Alfa Aesar/ Thermo Fischer Scientific and used as received. *Tris*(trimethylsilyl)phosphine ($(TMS)_3P$, 98%, stored frozen) was purchased from Strem Chemicals and used as received.

InP nanocrystal synthesis. In a typical iteration, indium acetate (0.8 mmol, 234 mg) and palmitic acid (2.4 mmol, 615 mg) were mixed with 8 mL of ODE in a 50 mL three-neck flask and fixed to a Schlenk line with a reflux condenser. The reaction mixture was degassed at 120°C for 2 hours, after which it was put back under N_2 flow and cooled to 70^{o}C. Next, a solution of $(TMS)_3P$ (0.6 mmol, 150 mg) in 600 μL of TOP was quickly injected into the flask. Following the injection, the mixture was heated to 240°C and stirred for 30 min before cooling back down to room temperature. The nanocrystals were precipitated with a 2:1 mixture of ethanol and methyl acetate, collected via centrifugation, and redispersed in hexanes. This washing procedure was repeated three times, and the nanocrystals were finally stored as a colloidal solution in hexanes.

GaX_3 ligand exchange. A solution of InP nanocrystals in hexanes (20 mL, 1 mg/mL) was layered atop an equimolar solution of GaI_3 and $GaCl_3$ in dimethylformamide (DMF) (3 mL, 0.05 M each), and stirred until all nanocrystals transferred to the DMF phase. The particles were precipitated by

the addition of a 1:1 toluene and hexane mixture and centrifuged. The precipitated particles were washed with toluene and acetonitrile separately 3 times and then allowed to dry overnight under nitrogen. The particles create a suspension instead of a dispersion in either solvent and can be precipitated out by centrifugation.

Molten salt dispersal and subsequent gallium exchange. The reduced gallium iodide salt $Ga^{(I)}Ga^{(III)}I_4$, nominally Ga_2I_4 was prepared by annealing equimolar amounts of gallium metal and gallium iodide in a sealed quartz ampoule at 450°C for 24 hours. A portion of 600 mg of the salt mixture was combined with the gallium halide ligand-exchanged NCs by adding them to the salt as a dry powder and combining them in a mortar and pestle. Next, the particle-salt mixture was loaded into a quartz ampoule. The salt was fused and stirred at 260°C using a glass-coated magnetic stir bar on a hot plate. The ampoule was next sealed under reduced pressure using an oxy-hydrogen torch and then annealed inside a furnace at 300°C and 330°C for an hour each.

QD recovery following molten salt treatment. An equimolar mixture of octadecylamine and dodecylamine was prepared separately, degassed at 100°C, and stored as a toluene solution (100 mg/mL) under inert atmosphere. After annealing, the ampoule was opened inside a glovebox, the salt phase was dissolved in anhydrous acetonitrile under stirring at 60°C, and the alloyed nanocrystals were collected via centrifugation. The precipitated nanocrystals were washed with fresh acetonitrile, collected, and finally redispersed as a colloidal solution using 2 mL of the solution of alkylamine ligands in toluene. The colloidal solution was centrifuged to discard any non-colloidal byproducts, the supernatant was collected separately, and washed with a 4:1 mixture of methyl acetate and acetonitrile. The precipitated $In_{1-x}Ga_xP$ nanocrystals were collected via centrifugation, and finally stored as a colloidal solution in toluene.

ZnS shelling. In a typical iteration, we degas a mixture of 784 mg (5.75 mmol, 1.2 equiv) zinc chloride in 5 mL oleylamine and 5 mL trioctylphosphine in a 25 mL round-bottomed flask at 120^{o}C for an hour, under vacuum. Simultaneously, in a 50 mL round bottomed flask equipped with a septum, we degassed 100 mg of gallium fluoride (GaF_3) in 3 mL oleylamine and 5 mL squalene at 120^{o}C under vacuum for 30 min, until effervescence subsided. A solution of ~15 mg $In_{1-x}Ga_xP$ nanocrystals (derived from 20 mg InP nanocrystals according to the cation exchange procedure above) in toluene was next added to the 50 mL round bottomed flask containing GaF_3 and degassed under vacuum at 120^{o}C for another 30 min, when the pressure gauge reaches a limiting value. Next, both flasks are returned to N_2 flow and the temperature of the $ZnCl_2$ solution is raised to 130^{o}C. 6 mL of a 0.8(M) TOP-S solution (total 4.8 mmol, 1 equiv) was loaded into a syringe with a needle, and 1.2 mL of that was introduced to the reaction mixture in the 50 mL flask. The temperature of the same was next raised to 310^{o}C and 2 mL of the $ZnCl_2$ precursor solution was added to it, followed by stirring at 310^{o}C for 30 min. The S and Zn precursor addition was repeated another four times during which 2 mL of the $ZnCl_2$ solution and 1.2 mL TOP-S were added to the reaction mixture and stirred at 30 min intervals. After completion, the reaction mixture was cooled down to room temperature, diluted with 5 mL of hexane and centrifuged at 8000 rpm to remove any non-colloidal byproducts. The clear solution was washed with ethanol, precipitated nanocrystals were collected via centrifugation and then redispersed in hexane with additonal oleylamine and trioctylphosphine ligands. The colloidal dispersion was washed a second time with methyl acetate to remove any organic residue, and the nanocrystals were stored as a colloidal dispersion in octane.

Optical characterization. UV-vis spectra were collected on colloidal solutions of QDs with a Shimadzu UV-3600i Plus UV-Vis-NIR spectrophotometer in transmission mode.

Photoluminescence emission spectra were collected on a Horiba Jobin Yvon FluoroMax-4 spectrophotometer. Excitation-Emission Maps were collected on a Horiba Jobin Yvon Fluorolog-3 spectrophotometer equipped with a Synapse OE-CCD detector. Absolute PLQY measurements were carried out using an integrating sphere (Labsphere) coupled with a computer-controlled spectrometer (Ocean Optics QE Pro) together with a 405-nm laser diode excitation source (LDM405, Thorlabs, 4.0 mW). Time-resolved fluorescence lifetimes were collected on a Picoquant Fluotime 300 fluorescence spectrometer with PMA 175 detector and an LDH-P-C-405 diode laser (excitation wavelength of 407.7 nm). High temperature PL spectra were recorded using a dilute colloidal solution of nanocrystals in ODE contained in a quartz ampoule sealed under inert atmosphere. A custom-built furnace setup interfaced with an Ocean Insight HR4Pro high-resolution spectrometer was utilized to record the high temperature PL spectra, which were corrected using a calibrated Ocean Insight HL-3plus precision lamp source. A 405 nm laser (CPS405, Thorlabs, 4.5 mW) was employed as the excitation source.

Powder X-ray diffraction. Powder x-ray diffraction patterns were collected on a Rigaku Miniflex X-ray diffractometer. Samples were deposited on (511)-oriented Si low background substrates. Average lattice parameter and Scherrer sizes were determined by fitting the {111}, {220}, and {311} peaks to pseudo-Voigt functions to extract the peak width and position. The lattice constants of bulk InP (5.8687 Å) and GaP (5.4505 Å) were used to calculate the alloy composition *x,* assuming a linear relationship between the lattice constant and alloying composition (Vegard's law) as follows:

$$a\left(In_{1-x}Ga_xP\right) = \left(1-x\right)a_{InP} + xa_{GaP}$$

Transmission electron microscopy. TEM images were obtained on an FEI Tecnai F30 microscope at 300 kV.

Small Angle X-ray Scattering (SAXS). Colloidal solutions of QDs in toluene were prepared in sealed Kapton capillaries for small-angle x-ray scattering (SAXS) experiments. SAXS patterns were collected using a SAXSLab Ganesha instrument with Cu Kα radiation (λ = 1.54 Å). The SAXS curves were analyzed by fitting to a quantitative model in Igor Pro using the Irena package (available at http://usaxs.xray.aps.anl.gov/staff/ilavsky/irena.html).[47] The scattering curves were fit in the particle size distribution module using the model-free Maximum Entropy approach. The particles' form factor was assumed to be that of a sphere with an aspect ratio of 1. The extracted size distributions were further fit with symmetric Gaussians to estimate average particle diameters along with the associated standard deviations.

X-Ray Fluorescence (XRF). X-ray fluorescence (XRF) analysis was performed with a benchtop Energy Dispersive Rigaku NEX DE VS X-ray fluorimeter equipped with a Peltier-cooled FAST SDD Silicon Drift Detector. All analyses were carried out under He atmosphere to increase sensitivity for lighter elements. Elemental ratios were determined using the standardless thin films fundamental parameters method as programmed in QuantEZ software provided by Rigaku, using the standard Rigaku calibration protocols. All samples were measured on a PTFE substrate to avoid the large Si Kα peak which interferes with the phosphorus Kα peak.

4.7. Chapter 4 bibliography.

1. Chen, O.; Zhao, J.; Chauhan, V. P.; Cui, J.; Wong, C.; Harris, D. K.; Wei, H.; Han, H.-S.; Fukumura, D.; Jain, R. K.; Bawendi, M. G., Compact high-quality CdSe–CdS core–shell nanocrystals with narrow emission linewidths and suppressed blinking. *Nat. Mater.* **2013,** *12* (5), 445-451. DOI: 10.1038/nmat3539.

2. Zhou, J.; Pu, C.; Jiao, T.; Hou, X.; Peng, X., A Two-Step Synthetic Strategy toward Monodisperse Colloidal CdSe and CdSe/CdS Core/Shell Nanocrystals. *J. Am. Chem. Soc.* **2016,** *138* (20), 6475-6483. DOI: 10.1021/jacs.6b00674.

3. Bae, W. K.; Padilha, L. A.; Park, Y.-S.; McDaniel, H.; Robel, I.; Pietryga, J. M.; Klimov, V. I., Controlled Alloying of the Core–Shell Interface in CdSe/CdS Quantum Dots for Suppression of Auger Recombination. *ACS Nano* **2013,** *7* (4), 3411-3419. DOI: 10.1021/nn4002825.

4. Park, Y.-S.; Lim, J.; Klimov, V. I., Asymmetrically strained quantum dots with non-fluctuating single-dot emission spectra and subthermal room-temperature linewidths. *Nat. Mater.* **2019,** *18* (3), 249-255. DOI: 10.1038/s41563-018-0254-7.

5. Ramasamy, P.; Ko, K.-J.; Kang, J.-W.; Lee, J.-S., Two-Step "Seed-Mediated" Synthetic Approach to Colloidal Indium Phosphide Quantum Dots with High-Purity Photo- and Electroluminescence. *Chem. Mater.* **2018,** *30* (11), 3643-3647. DOI: 10.1021/acs.chemmater.8b02049.

6. Van Avermaet, H.; Schiettecatte, P.; Hinz, S.; Giordano, L.; Ferrari, F.; Nayral, C.; Delpech, F.; Maultzsch, J.; Lange, H.; Hens, Z., Full-Spectrum InP-Based Quantum Dots with Near-Unity Photoluminescence Quantum Efficiency. *ACS Nano* **2022,** *16* (6), 9701-9712. DOI: 10.1021/acsnano.2c03138.

7. Ramasamy, P.; Kim, N.; Kang, Y.-S.; Ramirez, O.; Lee, J.-S., Tunable, Bright, and Narrow-Band Luminescence from Colloidal Indium Phosphide Quantum Dots. *Chem. Mater.* **2017,** *29* (16), 6893-6899. DOI: 10.1021/acs.chemmater.7b02204.

8. Won, Y.-H.; Cho, O.; Kim, T.; Chung, D.-Y.; Kim, T.; Chung, H.; Jang, H.; Lee, J.; Kim, D.; Jang, E., Highly efficient and stable InP/ZnSe/ZnS quantum dot light-emitting diodes. *Nature* **2019,** *575* (7784), 634-638. DOI: 10.1038/s41586-019-1771-5.

9. Kim, Y.; Ham, S.; Jang, H.; Min, J. H.; Chung, H.; Lee, J.; Kim, D.; Jang, E., Bright and Uniform Green Light Emitting InP/ZnSe/ZnS Quantum Dots for Wide Color Gamut Displays. *ACS Appl. Nano Mater.* **2019,** *2* (3), 1496-1504. DOI: 10.1021/acsanm.8b02063.

10. Mićić, O. I.; Ahrenkiel, S. P.; Nozik, A. J., Synthesis of extremely small InP quantum dots and electronic coupling in their disordered solid films. *Appl. Phys. Lett.* **2001,** *78* (25), 4022-4024. DOI: 10.1063/1.1379990.

11. Micic, O. I.; Curtis, C. J.; Jones, K. M.; Sprague, J. R.; Nozik, A. J., Synthesis and Characterization of InP Quantum Dots. *J. Phys. Chem.* **1994,** *98* (19), 4966-4969. DOI: 10.1021/j100070a004.

12. Siramdas, R.; McLaurin, E. J., InP Nanocrystals with Color-Tunable Luminescence by Microwave-Assisted Ionic-Liquid Etching. *Chem. Mater.* **2017,** *29* (5), 2101-2109. DOI: 10.1021/acs.chemmater.6b04457.

13. Lovingood, D. D.; Strouse, G. F., Microwave Induced In-Situ Active Ion Etching of Growing InP Nanocrystals. *Nano Lett.* **2008,** *8* (10), 3394-3397. DOI: 10.1021/nl802075j.

14. Yang, X.; Zhao, D.; Leck, K. S.; Tan, S. T.; Tang, Y. X.; Zhao, J.; Demir, H. V.; Sun, X. W., Full Visible Range Covering InP/ZnS Nanocrystals with High Photometric Performance and Their Application to White Quantum Dot Light-Emitting Diodes. *Adv. Mater.* **2012,** *24* (30), 4180-4185. DOI: https://doi.org/10.1002/adma.201104990.

15. Huang, F.; Bi, C.; Guo, R.; Zheng, C.; Ning, J.; Tian, J., Synthesis of Colloidal Blue-Emitting InP/ZnS Core/Shell Quantum Dots with the Assistance of Copper Cations. *J. Phys. Chem. Lett.* **2019,** *10* (21), 6720-6726. DOI: 10.1021/acs.jpclett.9b02386.

16. Kim, T.; Kim, K.-H.; Kim, S.; Choi, S.-M.; Jang, H.; Seo, H.-K.; Lee, H.; Chung, D.-Y.; Jang, E., Efficient and stable blue quantum dot light-emitting diode. *Nature* **2020,** *586* (7829), 385-389. DOI: 10.1038/s41586-020-2791-x.

17. Jang, E.; Jang, H., Review: Quantum Dot Light-Emitting Diodes. *Chem. Rev.* **2023,** *123* (8), 4663-4692. DOI: 10.1021/acs.chemrev.2c00695.

18. del Alamo, J. A., Nanometre-scale electronics with III–V compound semiconductors. *Nature* **2011,** *479* (7373), 317-323. DOI: 10.1038/nature10677.

19. Ko, H.; Takei, K.; Kapadia, R.; Chuang, S.; Fang, H.; Leu, P. W.; Ganapathi, K.; Plis, E.; Kim, H. S.; Chen, S.-Y.; Madsen, M.; Ford, A. C.; Chueh, Y.-L.; Krishna, S.; Salahuddin, S.; Javey, A., Ultrathin compound semiconductor on insulator layers for high-performance nanoscale transistors. *Nature* **2010,** *468* (7321), 286-289. DOI: 10.1038/nature09541.

20. Kroemer, H., Heterostructure bipolar transistors and integrated circuits. *Proc. IEEE* **1982,** *70* (1), 13-25. DOI: 10.1109/PROC.1982.12226.

21. Geisz, J. F.; France, R. M.; Schulte, K. L.; Steiner, M. A.; Norman, A. G.; Guthrey, H. L.; Young, M. R.; Song, T.; Moriarty, T., Six-junction III–V solar cells with 47.1% conversion efficiency under 143 Suns concentration. *Nature Energy* **2020,** *5* (4), 326-335. DOI: 10.1038/s41560-020-0598-5.

22. Wallentin, J.; Anttu, N.; Asoli, D.; Huffman, M.; Åberg, I.; Magnusson, M. H.; Siefer, G.; Fuss-Kailuweit, P.; Dimroth, F.; Witzigmann, B.; Xu, H. Q.; Samuelson, L.; Deppert, K.;

Borgström, M. T., InP Nanowire Array Solar Cells Achieving 13.8% Efficiency by Exceeding the Ray Optics Limit. *Science* **2013,** *339* (6123), 1057-1060. DOI: 10.1126/science.1230969.

23. Yoon, J.; Jo, S.; Chun, I. S.; Jung, I.; Kim, H.-S.; Meitl, M.; Menard, E.; Li, X.; Coleman, J. J.; Paik, U.; Rogers, J. A., GaAs photovoltaics and optoelectronics using releasable multilayer epitaxial assemblies. *Nature* **2010,** *465* (7296), 329-333. DOI: 10.1038/nature09054.

24. Nakamura, S.; Mukai, T.; Senoh, M., Candela-class high-brightness InGaN/AlGaN double-heterostructure blue-light-emitting diodes. *Appl. Phys. Lett.* **1994,** *64* (13), 1687-1689. DOI: 10.1063/1.111832.

25. Cho, A. Y.; Arthur, J. R., Molecular beam epitaxy. *Prog. Solid State Chem.* **1975,** *10*, 157-191. DOI: https://doi.org/10.1016/0079-6786(75)90005-9.

26. Dapkus, P. D.; Manasevit, H. M.; Hess, K. L.; Low, T. S.; Stillman, G. E., High purity GaAs prepared from trimethylgallium and arsine. *J. Cryst. Growth* **1981,** *55* (1), 10-23. DOI: https://doi.org/10.1016/0022-0248(81)90265-7.

27. Dijkkamp, D.; Venkatesan, T.; Wu, X. D.; Shaheen, S. A.; Jisrawi, N.; Min-Lee, Y. H.; McLean, W. L.; Croft, M., Preparation of Y-Ba-Cu oxide superconductor thin films using pulsed laser evaporation from high Tc bulk material. *Appl. Phys. Lett.* **1987,** *51* (8), 619-621. DOI: 10.1063/1.98366.

28. Cho, W.; Zhou, Z.; Lin, R.; Ondry, J. C.; Talapin, D. V., Synthesis of Colloidal GaN and AlN Nanocrystals in Biphasic Molten Salt/Organic Solvent Mixtures under High-Pressure Ammonia. *ACS Nano* **2023,** *17* (2), 1315-1326. DOI: 10.1021/acsnano.2c09552.

29. Zhang, H.; Dasbiswas, K.; Ludwig, N. B.; Han, G.; Lee, B.; Vaikuntanathan, S.; Talapin, D. V., Stable colloids in molten inorganic salts. *Nature* **2017,** *542* (7641), 328-331. DOI: 10.1038/nature21041.

30. Kamysbayev, V.; Srivastava, V.; Ludwig, N. B.; Borkiewicz, O. J.; Zhang, H.; Ilavsky, J.; Lee, B.; Chapman, K. W.; Vaikuntanathan, S.; Talapin, D. V., Nanocrystals in Molten Salts and Ionic Liquids: Experimental Observation of Ionic Correlations Extending beyond the Debye Length. *ACS Nano* **2019,** *13* (5), 5760-5770. DOI: 10.1021/acsnano.9b01292.

31. Srivastava, V.; Kamysbayev, V.; Hong, L.; Dunietz, E.; Klie, R. F.; Talapin, D. V., Colloidal Chemistry in Molten Salts: Synthesis of Luminescent $In_{1-x}Ga_xP$ and $In_{1-x}Ga_xAs$ Quantum Dots. *J. Am. Chem. Soc.* **2018,** *140* (38), 12144-12151. DOI: 10.1021/jacs.8b06971.

32. Onton, A.; Lorenz, M. R.; Reuter, W., Electronic Structure and Luminescence Processes in $In_{1-x}Ga_xP$ Alloys. *J. Appl. Phys.* **1971,** *42* (9), 3420-3432. DOI: 10.1063/1.1660748.

33. Williams, G. P.; Cerrina, F.; Lapeyre, G. J.; Anderson, J. R.; Smith, R. J.; Hermanson, J., Experimental study of the band structure of GaP, GaAs, GaSb, InP, InAs, and InSb. *Phys. Rev. B* **1986,** *34* (8), 5548-5557. DOI: 10.1103/PhysRevB.34.5548.

34. Onton, A.; Chicotka, R. J., Photoluminescence Processes in $In_{1-x}Ga_xP$ at 2°K. *Phys. Rev. B* **1971,** *4* (6), 1847-1853. DOI: 10.1103/PhysRevB.4.1847.

35. Gupta, A.; Ondry, J. C.; Lin, K.; Chen, Y.; Hudson, M. H.; Chen, M.; Schaller, R. D.; Rossini, A. J.; Rabani, E.; Talapin, D. V., Composition-Defined Optical Properties and the Direct-to-Indirect Transition in Core–Shell $In_{1-x}Ga_xP$/ZnS Colloidal Quantum Dots. *J. Am. Chem. Soc.* **2023,** *145* (30), 16429-16448. DOI: 10.1021/jacs.3c02709.

36. Tamang, S.; Lincheneau, C.; Hermans, Y.; Jeong, S.; Reiss, P., Chemistry of InP Nanocrystal Syntheses. *Chem. Mater.* **2016,** *28* (8), 2491-2506. DOI: 10.1021/acs.chemmater.5b05044.

37. Battaglia, D.; Peng, X., Formation of High Quality InP and InAs Nanocrystals in a Noncoordinating Solvent. *Nano Lett.* **2002,** *2* (9), 1027-1030. DOI: 10.1021/nl025687v.

38. Hudson, M. H.; Gupta, A.; Srivastava, V.; Janke, E. M.; Talapin, D. V., Synthesis of $In_{1-x}Ga_xP$ Quantum Dots in Lewis Basic Molten Salts: The Effects of Surface Chemistry, Reaction Conditions, and Molten Salt Composition. *J. Phys. Chem. C* **2022,** *126* (3), 1564-1580. DOI: 10.1021/acs.jpcc.1c10394.

39. Gupta, A.; Ondry, J. C.; Chen, M.; Hudson, M. H.; Coropceanu, I.; Sarma, N. A.; Talapin, D. V., Diffusion-Limited Kinetics of Isovalent Cation Exchange in III–V Nanocrystals Dispersed in Molten Salt Reaction Media. *Nano Lett.* **2022,** *22* (16), 6545-6552. DOI: 10.1021/acs.nanolett.2c01699.

40. Kroupa, D. M.; Vörös, M.; Brawand, N. P.; McNichols, B. W.; Miller, E. M.; Gu, J.; Nozik, A. J.; Sellinger, A.; Galli, G.; Beard, M. C., Tuning colloidal quantum dot band edge positions through solution-phase surface chemistry modification. *Nat. Commun.* **2017,** *8* (1), 15257. DOI: 10.1038/ncomms15257.

41. Soreni-Harari, M.; Yaacobi-Gross, N.; Steiner, D.; Aharoni, A.; Banin, U.; Millo, O.; Tessler, N., Tuning Energetic Levels in Nanocrystal Quantum Dots through Surface Manipulations. *Nano Lett.* **2008,** *8* (2), 678-684. DOI: 10.1021/nl0732171.

42. Rowland, C. E.; Liu, W.; Hannah, D. C.; Chan, M. K. Y.; Talapin, D. V.; Schaller, R. D., Thermal Stability of Colloidal InP Nanocrystals: Small Inorganic Ligands Boost High-Temperature Photoluminescence. *ACS Nano* **2014,** *8* (1), 977-985. DOI: 10.1021/nn405811p.

43. Zhao, Y.; Riemersma, C.; Pietra, F.; Koole, R.; de Mello Donegá, C.; Meijerink, A., High-Temperature Luminescence Quenching of Colloidal Quantum Dots. *ACS Nano* **2012,** *6* (10), 9058-9067. DOI: 10.1021/nn303217q.

44. Rowland, C. E.; Fedin, I.; Diroll, B. T.; Liu, Y.; Talapin, D. V.; Schaller, R. D., Elevated Temperature Photophysical Properties and Morphological Stability of CdSe and CdSe/CdS Nanoplatelets. *J. Phys. Chem. Lett.* **2018,** *9* (2), 286-293. DOI: 10.1021/acs.jpclett.7b02793.

45. Porter, V. J.; Geyer, S.; Halpert, J. E.; Kastner, M. A.; Bawendi, M. G., Photoconduction in Annealed and Chemically Treated CdSe/ZnS Inorganic Nanocrystal Films. *J. Phys. Chem. C* **2008,** *112* (7), 2308-2316. DOI: 10.1021/jp710173q.

46. Talapin, D. V.; Lee, J.-S.; Kovalenko, M. V.; Shevchenko, E. V., Prospects of Colloidal Nanocrystals for Electronic and Optoelectronic Applications. *Chem. Rev.* **2010,** *110* (1), 389-458. DOI: 10.1021/cr900137k.

47. Ilavsky, J.; Jemian, P. R., Irena: Tool Suite for Modeling and Analysis of Small-Angle Scattering. *J. Appl. Crystallogr.* **2009,** *42* (2), 347-353. DOI: doi:10.1107/S0021889809002222.

5. Summary and Outlook

III-V colloidal quantum dots, particularly InP nanocrystals, have emerged as a compelling choice for solution-processable emissive colloidal nanocrystals to reduce costs in Light Emitting Diode (LED) fabrication. They offer distinct advantages over their heavily optimized II-VI counterparts, such as reduced toxicity and enhanced stability. III-V bonds are predominantly covalent and rigid, which makes achieving defect-free crystal growth a challenging endeavor, especially at temperatures commonly accessible with traditional organic solvents. Additionally, achieving blue emission from InP nanocrystals is difficult, owing to the steep confinement-based sizing curve. To tackle these challenges, this study introduces a novel approach: the use of molten halide salts as a reaction medium for In-to-Ga cation exchange to yield alloyed $In_{1-x}Ga_xP$ nanocrystals with a higher bandgap than their InP counterparts.

We use this molten salt system to systematically study the effect of cation exchange on particle morphology and the kinetics of the In-to-Ga replacement. We find that the In-to-Ga cation exchange proceeds via surface recrystallization, evident from a transformation in particle morphology. This allows the activation energy of the rate-determining step in the cation exchange process to be considerably lower (~1eV) compared to the activation energy measured for self-diffusion in the corresponding bulk systems.

We next develop a subsequent oxygen-free shelling protocol to yield highly emissive $In_{1-x}Ga_xP$/ZnS colloidal NCs. We perform transient absorption spectroscopy and photoluminescence studies which demonstrate that the incorporation of gallium is accompanied by a decrease in oscillator strength of excitonic transitions, as indicated by a decreasing absorption cross-section and a monotonic increase in the radiative lifetime of emission. Atomistic calculations agree well

with experimental observations and confirm the trends of optical properties as gallium composition changes in the alloyed NCs. These results inform us that incorporating more gallium in $In_{1-x}Ga_xP$/ZnS NCs can only be part of a strategy to prepare blue III-P emitters since high gallium contents result in low oscillator strength of emissive states.

We next utilize these synthetic strategies to yield small alloyed $In_{1-x}Ga_xP$ nanocrystals by performing In-to-Ga cation exchange on smaller InP nanocrystals dispersed in a molten salt reaction medium. We achieve effective surface passivation by growing a highly crystalline thick ZnS shell on the $In_{1-x}Ga_xP$ core under rigorously oxygen-free conditions to yield bright and color pure blue emission with high PLQY and a narrow emission linewidth. Residual strain at the core-shell interface is alleviated by a better lattice match with the In-to-Ga cation exchanged nanocrystals. In essence, this underscores the importance of balancing nanocrystal size and gallium composition to achieve blue emission from $In_{1-x}Ga_xP$ nanocrystals while preserving the oscillator strength of direct-like interband transitions.

To improve upon the optoelectronic properties of $In_{1-x}Ga_xP$ nanocrystals, it is important to reduce the lattice mismatch at the core-shell interface. To this end, an alloyed Zn(Se,S) shell grown onto the $In_{1-x}Ga_xP$ core would significantly alleviate interfacial strain, especially for thick shells. Additionally, the L-type oleylamine and trioctylphosphine ligands utilized during shell growth, are known to be labile. We may achieve more stable device performance by switching to ligands that preferably bind to the nanocrystal surface. Lastly, diffusive mixing at a III–V/II-VI interface, such as substitutional Zn^{2+} defects may p-type dope III–V semiconductors by charge balance arguments. This leads to the creation of carrier localizing states and emission broadening. Therefore, an all III-V/III-V core-shell heterostructure, such as $In_{1-x}Ga_xP/Ga_{1-y}Al_yP$ would be optimal for optoelectronic performance.